NASA Contractor Report 3864

Analysis of the Surface Load and Radiated Sound of a Vibrating Airfoil With Application to the Experiment of Brooks

John E. Yates

CONTRACT NAS1-17003
JANUARY 1985

NASA

NASA Contractor Report 3864

Analysis of the Surface Load and Radiated Sound of a Vibrating Airfoil With Application to the Experiment of Brooks

John E. Yates

Aeronautical Research Associates of Princeton, Inc.
Princeton, New Jersey

Prepared for
Langley Research Center
under Contract NAS1-17003

National Aeronautics
and Space Administration

Scientific and Technical Information Branch

1985

TABLE OF CONTENTS

TABLE OF CONTENTS - cont.

APPENDICES:

ANALYSIS OF THE SURFACE LOAD AND RADIATED SOUND OF A VIBRATING AIRFOIL WITH APPLICATION TO THE EXPERIMENT OF BROOKS

John E. Yates

SUMMARY

A method is developed for calculating the surface load and radiated sound from a vibrating surface in a compressible viscous fluid. The method is applied to a thin two-dimensional elliptic cross-section. For large values of the viscous diffusion parameter, σ, the surface load tends to an elliptic distribution in agreement with the results of inviscid theory when edge pressure continuity (the Neumann condition) is enforced. For thin surfaces, the surface load is insensitive to variations in the thickness ratio.

A three-dimensional spectral technique is developed to calculate the inviscid surface load and radiated sound from a thin vibrating airfoil. Calculations are compared with an experiment of Brooks (1977). The inviscid theory predicts the correct form of the far field sound pressure and its phase. The actual levels are somewhat sensitive to the choice of theoretical spanwise surface pressure mode but are in better agreement with experiment than the surface pressure. The comparison of theoretical and experimental surface pressure indicates that the viscous theory, used to validate the inviscid theory, is either inadequate or there is a source of experimental error. A previous explanation (Yates, 1980) for the experimental data, that there is an equipartition of surface work into sound and viscous dissipation, is verified if flat surface loading is taken to occur near the airfoil edges. However present calculations fail to confirm the type loading indicated by the experiment.

1. INTRODUCTION

Brooks (Ref. 1) published the results of an experiment that was carefully designed to evaluate and hopefully validate the Kirchhoff integral formulation of sound radiation from a vibrating airfoil. The surface motion and pressure were measured and used in the Kirchhoff integral to calculate the far field sound. Simultaneously the sound field was measured and compared with the calculated field. The outcome was unexpected. The calculated sound field is 3 to 5 dB more intense than the measured field (see Appendix A, Figs. A.4, A.5). Also, the measured surface pressure distribution appears to have a virtual discontinuity across the leading and trailing edges although the spanwise distribution does decay smoothly to zero at the edges as may be expected (see Appendix A, Figs. A.2, A.3).

Yates (Refs. 2 and 3) published a plausible explanation of Brooks' results. Based on the premise that the measured surface pressure distribution is correct, a calculation was made of the partitioning of the surface work into radiated sound energy and vorticity formation near the edges. At the Helmholtz numbers of the experiment, the surface work is almost equally partitioned into sound and vortical energy produced near the leading and trailing edges. On the other hand, the inviscid Kirchhoff formulation, used by Brooks to calculate the far field, assigns all of the surface work to the far field. Hence, the 3 to 5 dB overestimation of the sound. Based on the energy argument of Yates, two conclusions were drawn. 1) Viscous forces cannot be neglected in the integral relation (e.g., see Ffowcs Williams and Hawkings, Ref. 4) between the surface and far field. 2) Viscous stresses must be included in the calculation of the surface load.

In a subsequent study the present author focused on the aerodynamic problem of calculating the surface load. It was shown (Ref. 5) that the inviscid aerodynamic problem is not well posed in that it admits eigensolutions. Furthermore, the far field sound depends on the magnitude of the eigensolution and is also not unique. By relaxing the usual Neumann edge uniqueness condition (continuity of pressure), it was possible to find by arbitrary adjustments of the eigensolution a surface pressure distribution in much better agreement with the one measured by Brooks. Because these inviscid results were encouraging, a direct viscous calculation of the load on a vibrating flat plate was made and included in Ref. 5. For Stokes number* ($\sigma = \sqrt{\omega c^2/4\nu}$) of order 10, a singular edge loading is calculated. For $\sigma \approx 100$, the edge load decays smoothly to zero in accordance with the Neumann condition. The Stokes number of the Brooks experiment is approximately 3000 (see Appendix A), and the calculated

*See remarks on P. 11 concerning this terminology.

viscous edge loading is in complete agreement with the inviscid theory plus Neumann condition. Based on the results of viscous thin airfoil theory (Ref. 6), Yates suggested that the viscous calculations must be made for the actual cross-sectional geometry of the airfoil with Stokes number based on the local edge radius.

The purpose of the present study is to perform the suggested detailed calculations for the surface pressure distribution and also for the sound field. Based on the results, evaluations are made of the experiment and its previous explanations. It is shown here that even with finite leading and trailing edge radii, the viscous theory predicts a surface load distribution that is in agreement with results of inviscid theory plus the Neumann edge condition. This is taken to indicate that either the viscous theory as applied is inadequate to predict the experimental results, or something was overlooked in the experiment. The present report does not offer a conclusive answer to this alternative. However, to conclude our study, specific questions were examined in detail with the use of inviscid load and acoustic theory. Follow up experimental and theoretical efforts are proposed in order to resolve unanswered questions of fundamental importance in our understanding of the role of viscous stresses in surface loading and noise production.

NOMENCLATURE

a	background speed of sound
A	b/c, aspect ratio for rectangular airfoil
A_n	coefficients in the series solution of the thickness problem see (2.3.16)
A^*	effective, aspect ratio, see Section 3.4
b	airfoil span, see Fig. 3.1-1
c	airfoil chord
c_p, c_v	specific heats at constant pressure and constant volume
C_{mn}	matrix coefficient, see (2.3.18),(2.3.21) or (3.2.17),(3.2.23)
$\vec{d}$	displacement vector, see (2.2.1)
$d_n(s)$, $d_t(s)$	see (2.2.8)
$D_n(s)$, $D_t(s)$	see (2.2.18)
D_N, D_T	see (2.3.4)
e, e'	see (3.5.1), (3.5.3), (3.6.1). (3.6.2)
$E(k)$, $K(k)$	standard elliptic integrals, see (2.3.28)
F_n	see (2.3.24), through (2.3.27)
$F(w)$	conformal mapping function, see (2.2.19) and (2.3.1)

g, g_o	see (2.2.25)
g_m	see (3.2.14)
G_m	see (2.3.19), (2.3.22)
h_o	amplitude of translation mode of vibration
h'	perturbation enthalpy
$\tilde{h}(\tilde{x})$	$= c\tau f(2\tilde{x}/c)$, airfoil thickness distribution
H	dimensionless perturbation enthalpy
H_f	acoustic far field enthalpy
H_o	surface enthalpy
i	$\sqrt{-1}$
$\vec{i}$, $\vec{j}$, $\vec{k}$	unit vectors along the x, y, z axes
Im	Imaginary part of a complex quantity
$J_n(z)$	Bessel function
k	$\omega c/2a$, Helmholtz number
$K(\vec{x})$	kernel function, see (3.2.8)
ℓ	reference length
L_n	coefficients in definition of load distribution, see (3.2.10)
$L_n^{(h)}$	load coefficients for the translation mode, see (3.2.21)

$L_n^{(\alpha)}$	load coefficient for the rotation mode, see (3.2.22)
$L(\vec{\xi})$	surface load distribution, see (3.2.2)
$\vec{n}$	unit normal vector to C_o, see Fig. 2.1-1
p	background pressure
p'	perturbation pressure
$\vec{p}$	unit vector, see Fig. 2.1-1
p_{ref}	dB reference pressure, 2×10^{-4} dynes/cm^2
p'_{rms}	root mean square pressure, see (3.2.29)
P	pressure in dB, see (3.2.30 and 3.2.31)
$\mathscr{P}_a$	radiated acoustic energy, see (4.1.9)
P_{mn}	see (3.2.23)
P_n	Legendre polynamial
Pr	Prandtl number
$\mathscr{P}_{ref}$	dB reference power, 10^{-12} watts
$\mathscr{P}_v$	dissipated vortical energy, see (4.1.10)
$P(-1), P(1)$	leading and trailing edge load (experimental)
$\|q\|$	absolute value of the quantity q

q^*	complex conjugate of the quantity q
q^+	Fourier transform of the quantity q, see (4.2.1) and (4.23)
Q_{mn}	see (3.2.23)
R	perfect gas constant or Euclidean distance, see (Eq. 3.3.3)
Re	real part of a complex quantity
s	speed ratio see (4.1.5) or arc length
s'	perturbation entropy
$S(\hat{ky})$	see (3.2.5)
S_{mn}	see (3.2.13)
$S(\beta)$	see (3.3.10)
t	time
T	background temperature
$U_n(x)$	Chebyshev polynomials of the second kind, see (3.2.11)
V_∞	free stream velocity
$\vec{V}'$	perturbation velocity
$\vec{\mathcal{V}}'$	dimensionless perturbation velocity
$\mathscr{W}_o$	surface work, see (4.1.8)
x_o	h_o/α_o, axis of rotation

$\vec{x}_o(s)$	vector definition of the vibrating surface C_o, see Fig. 2.1-1
x,y,z or x_i	Cartesian coordinates
$\vec{t}$	unit tangent vector to C_o, see Fig. 2.1-1
α	$\sigma e^{i\pi/4}$ (or Fourier transform variable)
α_o	amplitude of rotational mode of vibration
α,β	Fourier transform variables of (x,y)
$\Gamma(z)$	gamma function
δ	σs
δ_{mn}	Kroneker delta symbol
Δe	increment of acceleration sensitivity parameter, see (3.5.1) or increment of in-plane vibration amplitude, see (3.6.1)
λ	see (3.2.19)
λ, μ	coefficients of viscosity
λ_o, λ_1	see (4.2.4), (4.2.5)
ν	μ/ρ, coefficient of kinematic viscosity
ρ	background density
σ	$\frac{c}{2}\sqrt{\frac{\omega}{\nu}}$
τ	airfoil thickness ratio, see (3.1.8)
τ_{ij}	perturbation viscous stress, see (2.1.4)
ψ	$\pi-\beta$, directivity angle, see Fig. 3.2-1

ω	frequency (rad/sec)
$\vec{\Omega}$	dimensionless perturbation vorticity
$\gamma(x)$	vorticity distribution, see (4.3.4)
∇^2	Laplace operator
γ	c_p/c_v, ratio of specific heats
$\mathscr{J}_\varepsilon$	see (4.4.25) and Fig. 4.4-1 for graph of $\mathscr{J}_o$
(-)	used to denote dimensional variables in Section 3
grad	gradient operator
div	divergence operator
curl	vector curl operator

2. ANALYSIS OF A VIBRATING SURFACE OF FINITE THICKNESS IN A COMPRESSIBLE VISCOUS MEDIUM AT REST

2.1 Basic Formulation and Assumptions

We adopt the Navier-Stokes equations as the starting point for our analysis. These equations are linearized around a background stationary fluid medium that we assume to be a perfect gas. Using primes to denote perturbation quantities, the linearized equations can be expressed in terms of enthalpy h', entropy s', and velocity v_i' as follows:

$$\frac{1}{a^2}\frac{\partial h'}{\partial t} + \frac{\partial v_i'}{\partial x^i} = \frac{\partial}{\partial t}\left(\frac{s'}{R}\right) \tag{2.1.1}$$

$$\frac{\partial v_i'}{\partial t} + \frac{\partial h'}{\partial x^i} = T\frac{\partial s'}{\partial x^i} + \frac{\partial}{\partial x^j}\left(\frac{\tau_{ij}'}{\rho}\right) \tag{2.1.2}$$

$$\frac{\partial}{\partial t}\left(\frac{s'}{R}\right) = \frac{\mu}{p \cdot Pr}\nabla^2 h' \tag{2.1.3}$$

where the following definitions pertain:

$$\tau_{ij}' = \lambda\frac{\partial v^{k'}}{\partial x^k}\delta_{ij} + \mu\left(\frac{\partial v_i'}{\partial x^i} + \frac{\partial v_j'}{\partial x^i}\right) \quad \text{Viscous Stress Tensor} \tag{2.1.4}$$

$$Pr = \frac{c_p\mu}{k} \qquad \text{Prandtl Number} \tag{2.1.5}$$

$$p = \rho RT \qquad \text{Perfect Gas Law} \tag{2.1.6}$$

The perturbation pressure can be calculated in terms of h' and s' with the formula

$$p' = \rho h' - p \cdot \frac{s'}{R} \tag{2.1.7}$$

We first assume that viscous processes are more important than heat conduction processes for the problem under consideration. This means that the Prandtl number is infinite and the perturbation entropy is zero. It is consistent with this assumption to neglect compressible viscous effects. Such terms in the momentum equation lead to the ultimate conversion of acoustic energy into heat many wave lengths from the vibrating surface and are only important in the near field for frequencies in the gega hertz range. With the foregoing assumptions, the perturbation equations reduce to the following set:

$$\frac{1}{a^2}\frac{\partial h'}{\partial t} + \operatorname{div} \vec{v}' = 0 \tag{2.1.8}$$

$$\frac{\partial \vec{v}'}{\partial t} + \operatorname{grad} h' = -\nu \operatorname{curl} (\operatorname{curl} \vec{v}') \tag{2.1.9}$$

with the pressure given by

$$p' = \rho h' \tag{2.1.10}$$

Justification of the Model

The foregoing equations or their inviscid counterpart with $\nu = 0$ will be used throughout this report except in Section 4 where we modify the equations to include a constant streaming velocity. We have derived these equations somewhat formally without reference to the specific application we have in mind; i.e., analysis of the Brooks experiment. The linearized model is justified on the grounds that all of the near field and acoustic pressures measured by Brooks were simple harmonic in time. Furthermore, the maximum velocity on the airfoil surface (see Appendix A) was in all cases less than 0.5 ft/sec with amplitudes less than three thousandths of an inch.

The formal assumption of an infinite Prandtl number can be justified as follows. We use Eq. (2.1.3) to deduce the order of magnitude of entropy variations relative to enthalpy variations. Suppose that h' varies on a length scale ℓ and the basic frequency is ω. Then

$$\frac{|s'|}{R} = \frac{\mu}{p \cdot Pr \cdot \omega \ell^2} |h'|$$

$$= \frac{1}{Pr} \cdot \frac{\gamma}{a^2} \cdot \frac{1}{\sigma} |h'| \tag{2.1.11}$$

where

$$\sigma = \ell\sqrt{\frac{\omega}{\nu}} \tag{2.1.12}$$

is the Stokes number* based on the length scale of the enthalpy fluctuations. From the table of basic data in Appendix A, the Stokes number is of order 3000 based on the semi-chord. If we use the radius of curvature of a 12% thick airfoil, the Stokes number is still of order 30. The relative contribution of the enthalpy and entropy to the pressure can be estimated with (2.1.7). We have

$$\frac{|p'|}{\rho} = |h'| - \frac{a^2}{\gamma} \cdot \frac{|s'|}{R} = |h'| - \frac{|h'|}{\sigma Pr} \tag{2.1.13}$$

Even for a Prandtl number of unity (more typical of air), the entropy contribution to the pressure is of order $(1/\sigma)$ smaller than the enthalpy contribution. Thus we can safely use the isentropic model (2.1.8, 2.1.9, 2.1.10) to analyze the length and time scales that are important in the Brooks experiment.

2.2 The Two-Dimensional Boundary Value Problem

Referring to Fig. 2.1-1 we consider a two-dimensional surface C_o that executes rigid body simple harmonic translation and rotation about the origin of coordinates. The surface displacement can be expressed in the form

$$\vec{d} = Re[(\vec{p}h_o - \alpha_o \vec{k}x\vec{x}_o(s))e^{i\omega t}] \tag{2.2.1}$$

where $\vec{p}$ is a unit vector in the direction of the translation mode with amplitude h_o, and α_o is the amplitude of the rotation mode. The vector $\vec{x}_o(s)$ defines the surface C_o where s is the arc length along the boundary as indicated in Fig. 2.1-1. The unit vectors tangent and normal to C_o are defined by the relations

---

*Actually σ^2 is a Reynolds number based on the velocity $\omega\ell$ and length ℓ. However, σ is the more natural viscous diffusion parameter of the problem and will be referred to as the Stokes number in this report, although the author could not find a precedent for this terminology.

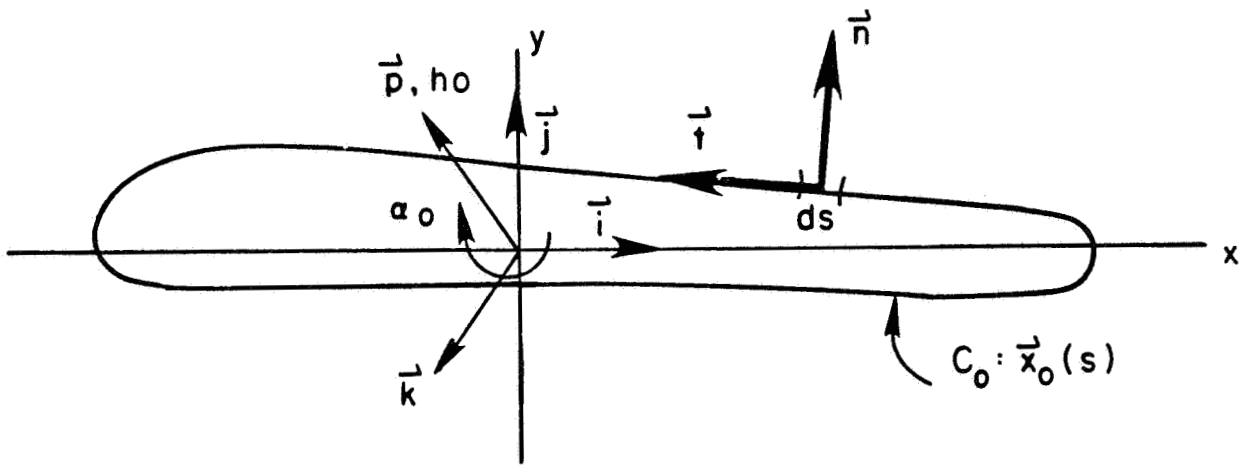

Figure 2.1-1 Vibrating Two-Dimensional Surface in a Compressible Viscous Medium.

$$\vec{t} = \frac{d\vec{x}_o}{ds} \tag{2.2.2}$$

$$\vec{n} = \vec{t}x\vec{k} \tag{2.2.3}$$

The boundary value problem for the perturbation enthalpy and vorticity is given by the following formulae:

$$\nabla^2 h' + \frac{\omega^2}{a^2} h' = 0 \tag{2.2.4}$$

$$\nabla^2 \Omega' - \frac{i\omega}{\nu} \Omega' = 0 \tag{2.2.5}$$

$$\frac{\partial h'}{\partial s} - \nu \frac{\partial \Omega'}{\partial n} = \omega^2 d_t(s) \quad \text{on} \quad C_o \tag{2.2.6}$$

$$\frac{\partial h'}{\partial n} + \nu \frac{\partial \Omega'}{\partial s} = \omega^2 d_n(s) \quad \text{on} \quad C_o \tag{2.2.7}$$

where

$$d_n(s) = (\vec{n}\cdot\vec{p})h_o + (\vec{t}\cdot\vec{x}_o)\alpha_o$$

$$d_t(s) = (\vec{t}\cdot\vec{p})h_o - (\vec{n}\cdot\vec{x}_o)\alpha_o \tag{2.2.8}$$

The perturbation vorticity Ω' is related to the perturbation velocity via the relation

$$\Omega' = \vec{k} \cdot \text{curl } \vec{v}' \tag{2.2.9}$$

To solve the foregoing problem, we first introduce dimensionless dependent and independent variables as follows:

$$(\vec{x},\vec{x}_o,h_o) \rightarrow \frac{c}{2} (\vec{x},\vec{x}_o,h_o)$$

$$h' = \left(\frac{\omega c}{2}\right)^2 H, \quad \Omega' = \omega\, \Omega \tag{2.2.10}$$

with

$$k = \frac{\omega c}{2a} \qquad \text{Helmholtz Number} \tag{2.2.11}$$

$$\sigma = \frac{c}{2}\sqrt{\frac{\omega}{\nu}} \qquad \text{Stokes Number Based on Semi-Chord} \tag{2.2.12}$$

$$\alpha = \sigma e^{i\pi/4} \tag{2.2.13}$$

The dimensionless problem becomes

$$\nabla^2 H + k^2 H = 0 \tag{2.2.14}$$

$$\nabla^2 \Omega - \alpha^2 \Omega = 0 \tag{2.2.15}$$

with

$$\frac{\partial H}{\partial n} + \frac{1}{\sigma^2}\frac{\partial \Omega}{\partial s} = D_n(s) \quad \text{on} \quad C_o \tag{2.2.16}$$

$$\frac{\partial H}{\partial s} - \frac{1}{\sigma^2}\frac{\partial \Omega}{\partial n} = D_t(s) \quad \text{on} \quad C_o \tag{2.2.17}$$

where

$$D_n(s) = (\vec{n}\cdot\vec{p})h_o + (\vec{t}\cdot\vec{x}_o)\alpha_o$$

$$D_t(s) = (\vec{t}\cdot\vec{p})h_o - (\vec{n}\cdot\vec{x}_o)\alpha_o \tag{2.2.18}$$

Finally, we introduce a conformal map from the physical plane $z = x + iy$ to an arbitrary new plane $w = u + iv$ via the transformation

$$z = F(w) \tag{2.2.19}$$

The problem in the w-plane can be expressed as follows

$$\nabla^2 H + k^2 g^2 H = 0 \tag{2.2.20}$$

$$\nabla^2 \Omega - \alpha^2 g^2 \Omega = 0 \tag{2.2.21}$$

with

$$\nabla^2 \equiv \frac{\partial^2}{\partial u^2} + \frac{\partial^2}{\partial v^2} \tag{2.2.22}$$

The boundary conditions on C_o', the image of C_o under the conformal map, are

$$\frac{\partial H}{\partial N} + \frac{1}{\sigma_o^2} \frac{\partial \Omega}{\partial S} = D_N(S) = g_o D_n \tag{2.2.23}$$

$$\frac{\partial H}{\partial S} - \frac{1}{\sigma_o^2} \frac{\partial \Omega}{\partial N} = D_T(S) = g_o D_t \tag{2.2.24}$$

The connection formulae that relate the z-plane and w-plane are

$$g = \left|\frac{dz}{dw}\right| = |F'(w)| \quad , \quad g_o = g(u_o, v_o) \tag{2.2.25}$$

$$z_o = F(w_o) \quad , \quad dS = \frac{ds}{g_o} \text{ on } C_o' \tag{2.2.26}$$

$$\frac{\partial}{\partial S} = g_o \frac{\partial}{\partial s} \quad , \quad \frac{\partial}{\partial N} = g_o \frac{\partial}{\partial n} \tag{2.2.27}$$

2.3 The Vibrating Elliptic Airfoil

We consider the special case of an elliptic cross section that vibrates along the y-axis ($\vec{p} = \vec{j}$) and rotates about the origin of coordinates (see Fig. 2.1-1). Furthermore, we construct the solution in the w-plane where the ellipse becomes the unit circle. The appropriate map is the Joukowski transformation,

$$z = F(w) = \frac{1+\tau}{2} \cdot w + \frac{1-\tau}{2} \cdot \frac{1}{w} \tag{2.3.1}$$

where τ is the thickness ratio. Thus

$$g_o(\theta) = (\sin^2 \theta + \tau^2 \cos^2 \theta)^{1/2} \tag{2.3.2}$$

$$\vec{t}\cdot\vec{j} = \tau \cos \theta/g_o \quad , \quad \vec{n}\cdot\vec{j} = \sin \theta/g_o$$

$$\vec{t}\cdot\vec{x}_o = -\left(\frac{1-\tau^2}{2}\right)\frac{\sin 2\theta}{g_o} \quad , \quad \vec{n}\cdot\vec{x}_o = \tau/g_o \tag{2.3.3}$$

so that

$$D_N = h_o \sin \theta - \left(\frac{1-\tau^2}{2}\right)\alpha_o \sin 2\theta$$

$$D_T = h_o\tau \cos \theta - \alpha_o\tau \tag{2.3.4}$$

Consider the solution of (2.2.21) in the neighborhood of the surface of the unit circle (C_o') in the w-plane. Let

$$r = 1 + R/\sigma \tag{2.3.5}$$

so that

$$\nabla^2 = \sigma^2\left[\frac{\partial^2}{\partial R^2} + \frac{1}{\sigma+R}\frac{\partial}{\partial R} + \frac{1}{(\sigma+R)^2}\frac{\partial^2}{\partial \theta^2}\right] \tag{2.3.6}$$

and

$$g^2 = g_o^2(\theta) + O(1/\sigma) \tag{2.3.7}$$

For $\sigma \to \infty$ with $R = O(1)$, we obtain the approximate formula

$$\frac{\partial^2 \Omega}{\partial R^2} - ig_o^2\Omega = 0 \tag{2.3.8}$$

with the solution

$$\Omega = \Omega_o(\theta) e^{-g_o e^{i\pi/4} R}$$

$$= \Omega_o(\theta) e^{-\alpha g_o (r-1)} \qquad (2.3.9)$$

Thus

$$\left.\frac{\partial \Omega}{\partial r}\right|_{r=1} = -\alpha g_o \Omega_o(\theta) \qquad (2.3.10)$$

and from (2.2.24) we obtain

$$\frac{\Omega_o}{{}_o^2} = -\frac{1}{\alpha \dot{g}_o}\frac{\partial H}{\partial \theta} + \frac{D_T}{\alpha g_o} \qquad (2.3.11)$$

With the last result, the boundary condition (2.2.23) becomes (in the circle plane)

$$\frac{\partial H}{\partial r} - \frac{1}{\alpha}\frac{\partial}{\partial \theta}\left(\frac{1}{\dot{g}_o}\frac{\partial H}{\partial \theta}\right) = D_N(\theta) - \frac{1}{\alpha}\frac{\partial}{\partial \theta}\left(\frac{D_T}{g_o}\right) \qquad (2.3.12)$$

Furthermore, we use (2.3.4) to show that

$$\frac{\partial}{\partial \theta}\left(\frac{D_T}{g_o}\right) = -\frac{\tau}{g_o^3} \cdot D_N \qquad (2.3.13)$$

The final boundary value problem for H becomes:

$$\nabla^2 H + k^2 g^2 H = 0 \qquad (2.3.14)$$

$$\left(\frac{\partial H}{\partial r} - \frac{1}{\alpha}\frac{\partial}{\partial \theta}\cdot\frac{1}{g_o}\frac{\partial H}{\partial \theta}\right)_{r=1} = \left(1 + \frac{\tau}{\alpha g_o^3}\right) D_N \qquad (2.3.15)$$

We remark that the last result can be derived for an arbitrary cross section. However, the basic point of this section concerning the nature of the edge loading can be made with the special case of an elliptic cross section. It is important to note, however, that the coupled problem for enthalpy and vorticity has been reduced to a more simple problem for the

enthalpy alone with a higher order boundary condition due to viscosity. Without the second derivative with respect to θ in the boundary condition (2.3.15) the solution of (2.3.14) is in general not unique.

The solution of (2.3.14) can be constructed for arbitrary Helmholtz number k. However, we are trying to deduce the character of the edge loading with the viscous model. It is sufficient to illustrate the nature of the edge load for the compact surface for which k tends to zero. Thus, we consider the solution of Laplace's equation in the circle plane with the generalized viscous boundary condition (2.3.15). Assume a series solution of the form

$$H = \sum_{n=1}^{\infty} A_n \frac{\sin n\,\theta}{r^n} \tag{2.3.16}$$

where the coefficients A_n are to be determined by the surface boundary condition. Substitute (2.3.16) into (2.3.15), multiply by sin m θ, and integrate over $0 < \theta < 2\pi$ to obtain the following system of equations:

$$\sum_{n=1}^{N} C_{mn}\, A_n = G_m \qquad m=1,2,\ldots N \tag{2.3.17}$$

The matrix coefficients and surface enthalpy for the translation and rotation modes are defined below.

Translation

$$C_{mn} = \delta_{mn} - \frac{(2n-1)}{2\alpha}\left[F_{2(m-n)} + F_{2(m+n-1)}\right] \tag{2.3.18}$$

$$G_m = \delta_{m1} + \frac{\tau}{2\alpha}\left[F_{2m} + F_{2(m-1)}\right] \tag{2.3.19}$$

$$H_o(x) = \sum_{n=1}^{N} A_n \sin (2n-1)\theta, \quad \cos\theta = x \tag{2.3.20}$$

Rotation

$$C_{mn} = \delta_{mn} - \frac{n}{\alpha} F_{2(m-n)} + F_{2(m+n)} \tag{2.3.21}$$

$$G_m = \frac{(1-\tau^2)}{4} \delta_{m1} + \frac{\tau}{\alpha} F_{2m} \tag{2.3.22}$$

$$H_o(x) = \sum_{n=1}^{N} A_n \sin 2n\theta \ , \quad \cos \theta = x \tag{2.3.23}$$

The coefficients F_n are defined by the following integral relation:

$$F_n(\tau) = \frac{1}{\pi} \int_o^{2\pi} \frac{\cos n\theta}{g_o(\theta)} d\theta$$

$$= \frac{2}{\pi} \int_o^{\pi} \frac{\cos n\theta \, d\theta}{(\sin^2 \theta + \tau^2 \cos^2 \theta)^{1/2}} \ , \ n=0,2,4... \tag{2.3.24}$$

These coefficients can most easily be calculated with the following recursion formula

$$F_{n+2} = \frac{2(2/k'^2-1)F_n - (1-1/n)F_{n-2}}{1 - 1/n} \tag{2.3.25}$$

and the starting values

$$F_o = \frac{4}{\pi} K(k')$$

$$F_2 = \left(\frac{2}{k'^2} - 1\right) F_o - \frac{8}{\pi k'^2} E(k') \tag{2.3.26}$$

where

$$k' = \sqrt{1-\tau^2} \tag{2.3.27}$$

and $E(k')$, $K(k')$ are the standard elliptic integrals (Ref. 7); i.e.,

$$E(k') = \int_0^{\pi/2} \sqrt{1-k'^2 \sin^2\theta}\, d\theta$$

$$K(k') = \int_0^{\pi/2} \frac{d\theta}{\sqrt{1-k'^2 \sin^2\theta}} \qquad (2.3.28)$$

2.4 Incompressible Viscous Load Calculations

The matrix Eq. (2.3.17) was solved numerically for unit translational and rotational modes of vibration of an elliptic airfoil section. Thickness ratios, $\tau = .05, .1, .2$, and Stokes numbers $\sigma = 10, 100, 400$ were considered. The results for the modal surface load distributions (2.3.16) are presented in Figs. 2.4-1 through 2.4-4. The effect of thickness on the load distribution is relatively small for $\tau < 0.2$. Thus, we have only presented results for all three values of τ for the lowest value of Stokes number; i.e. $\sigma = 10$ in Figs. 2.4-1 and 2.4-2. For $\sigma = 10$ the out of phase (imaginary) part of the load is relatively large and there is a tendency toward a large edge loading. This result is in qualitative agreement with the flat plate viscous calculations of Ref. 5. For $\sigma = 100$ and 400 the out of phase load becomes much smaller, thus indicating that less work is done against the fluid (see Section 4.4). The more important point is that the edge load becomes elliptic in agreement with the result one would obtain by applying the Neumann edge condition to the inviscid calculation. We conclude that with the present method of analysis the combined effect of viscosity and geometric thickness does not lead to a flat edge load distribution of the type that Brooks measured (see Appendix A, Fig. A.2). In the following section we develop the solution of the inviscid problem with Neumann edge condition and compare our results with those of the experiment. In Section 4, we reexamine the viscous problem for the case of zero thickness.

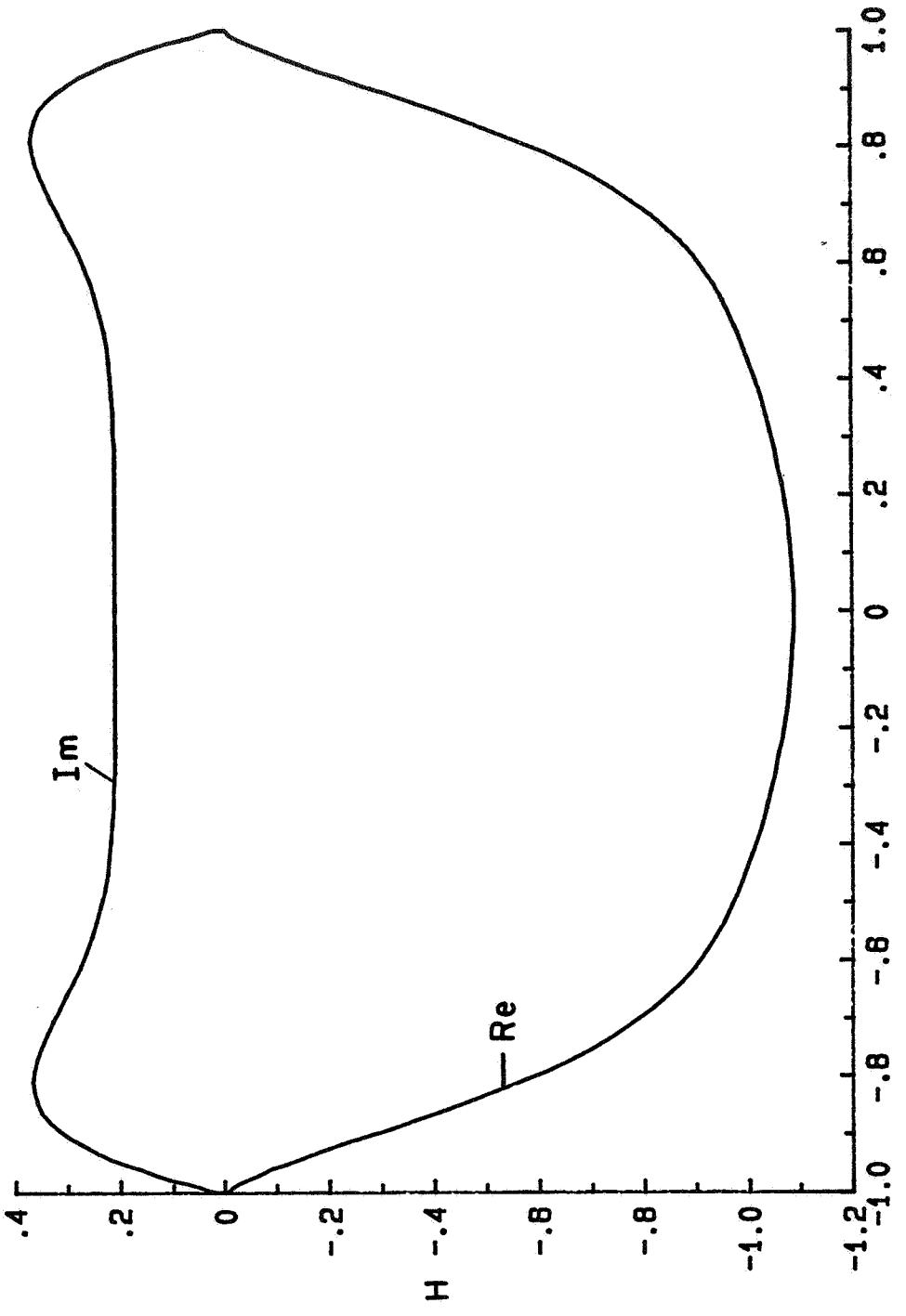

Figure 2.4-1a - Translational Mode: τ=0, σ=10.

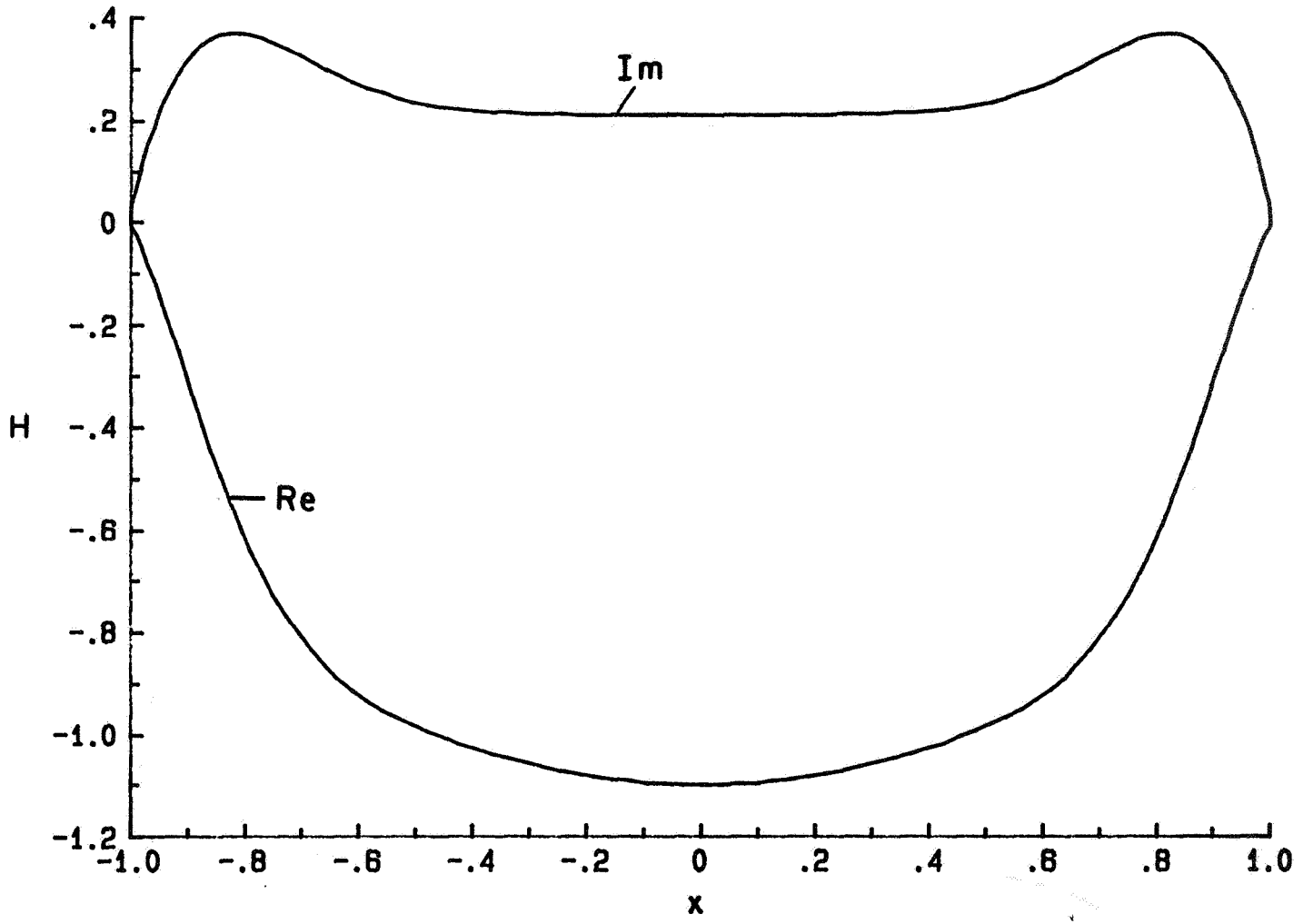

Figure 2.4-1b - Translational Mode: τ=0.1, σ=10.

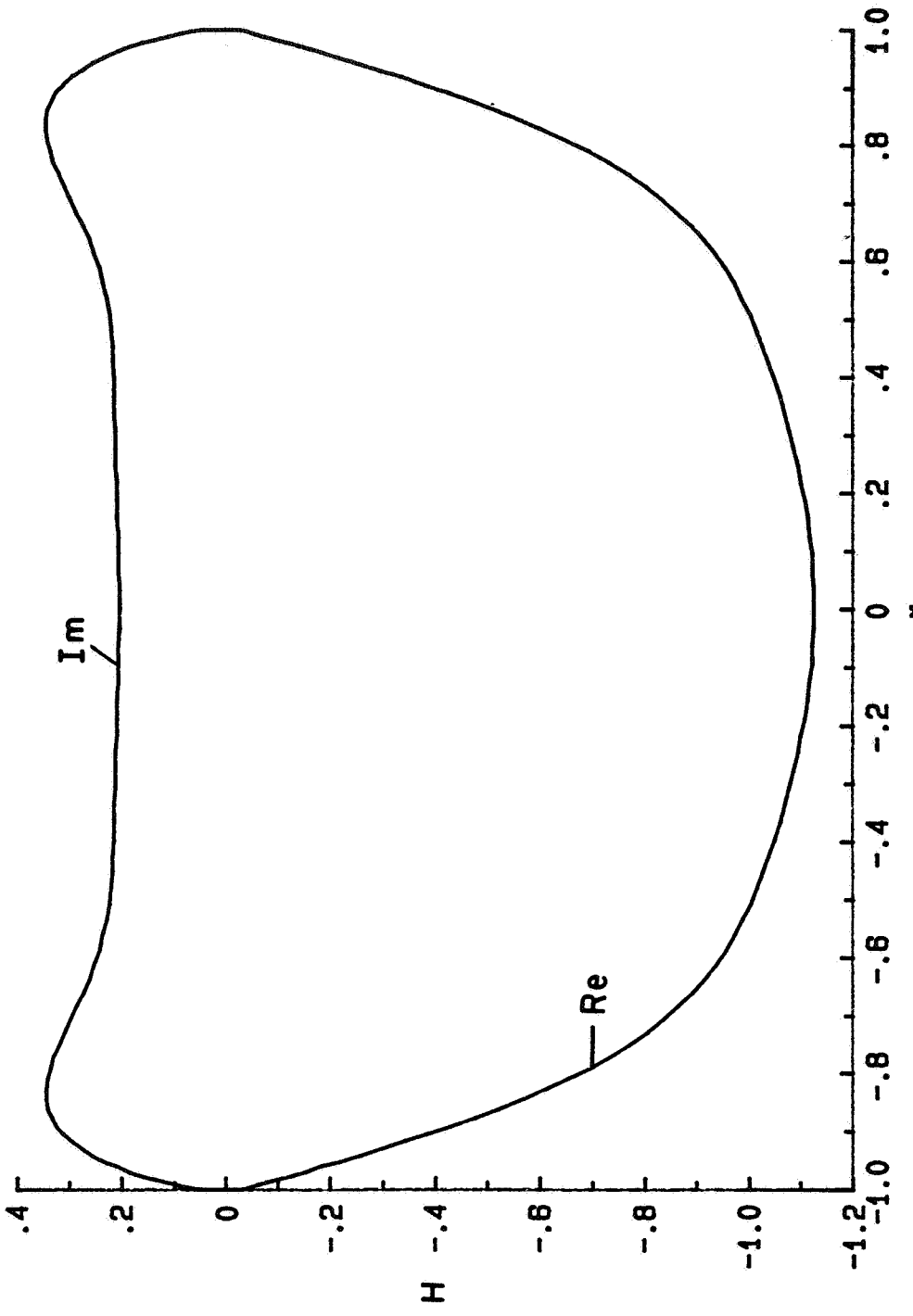

Figure 2.4-1c - Translational Mode: τ=0.2 , σ=10.

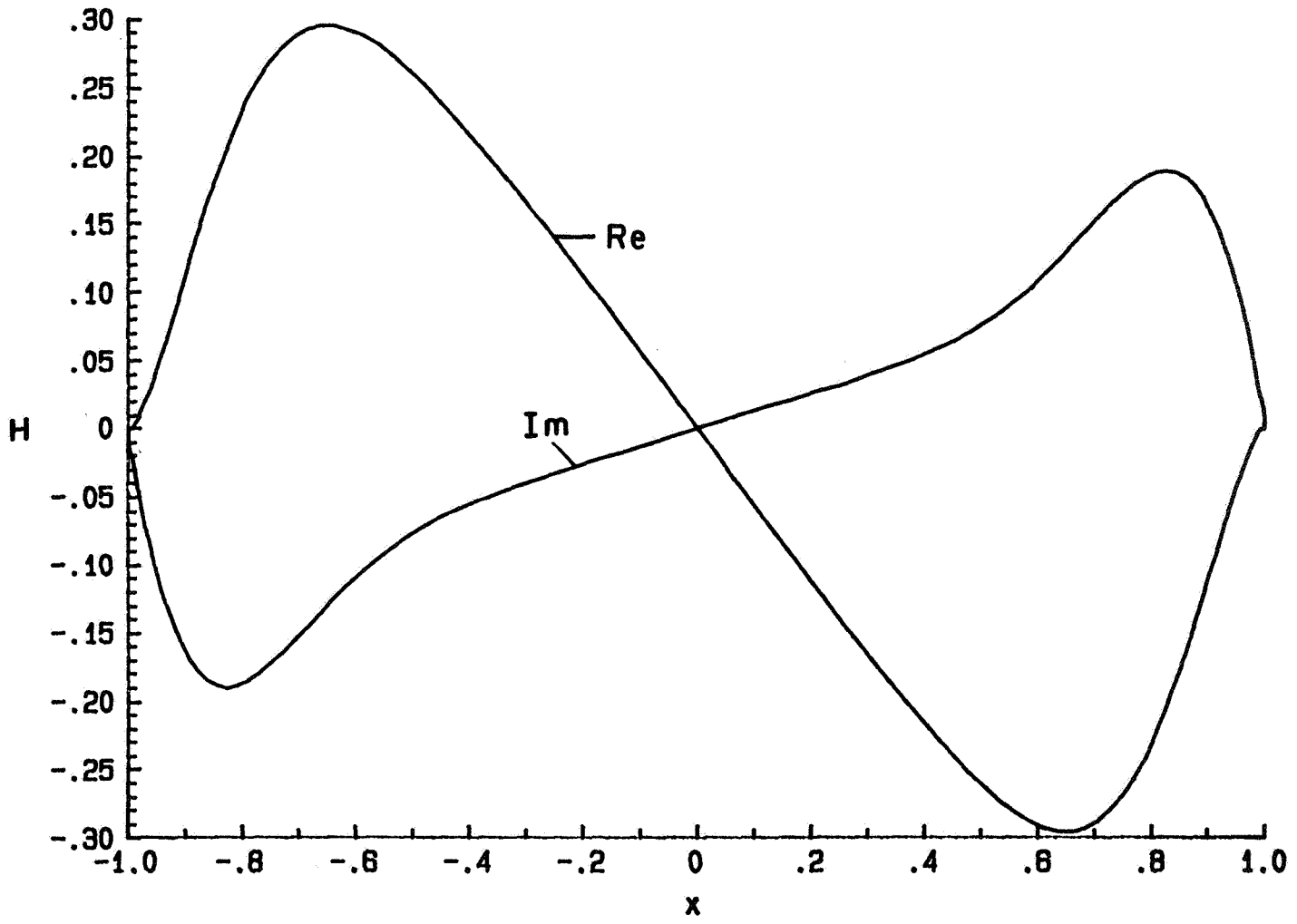

Figure 2.4-2a - Rotational Mode: τ=.05, σ=10.

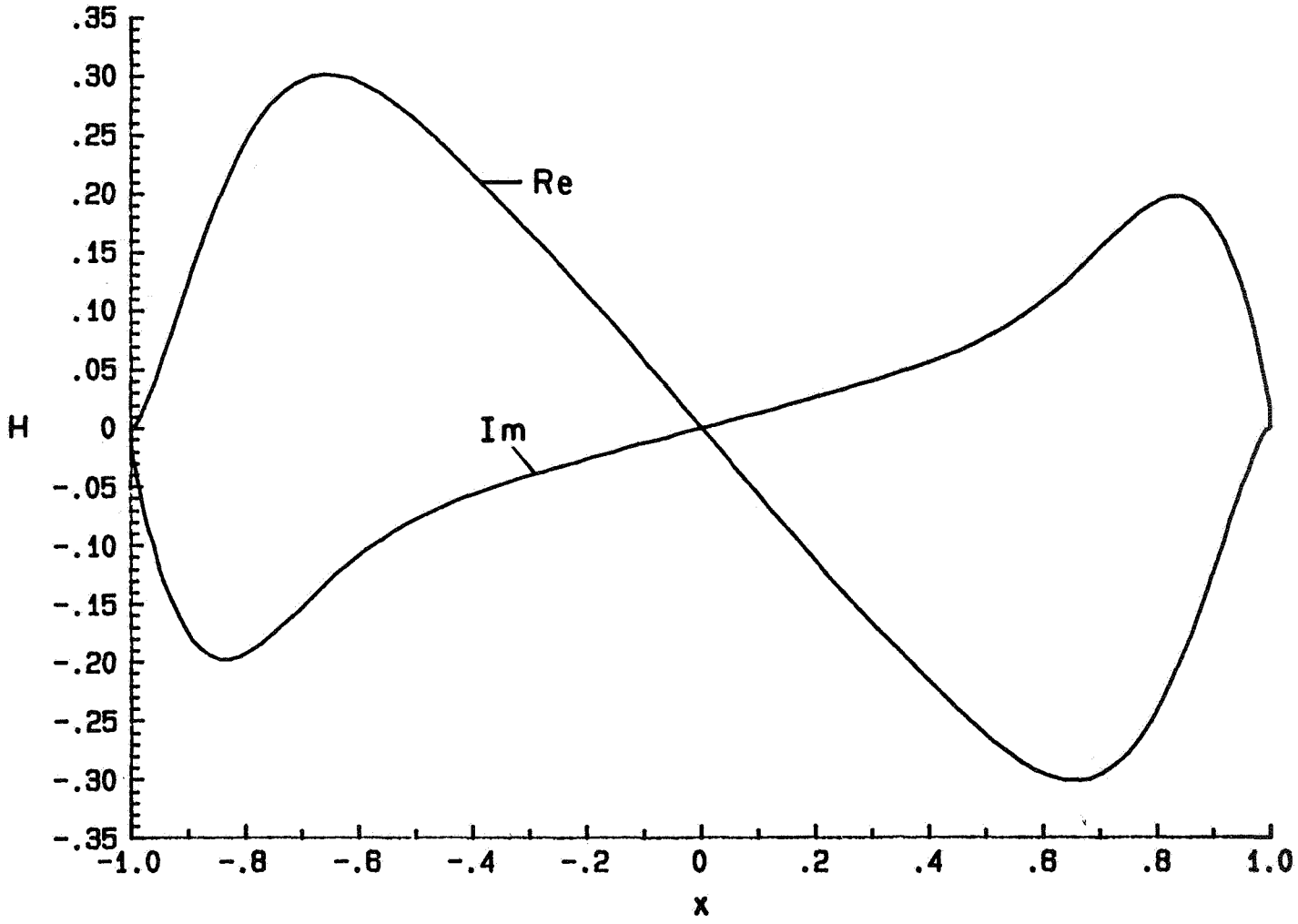

Figure 2.4-2b - Rotational Mode; τ=0.1, σ=10.

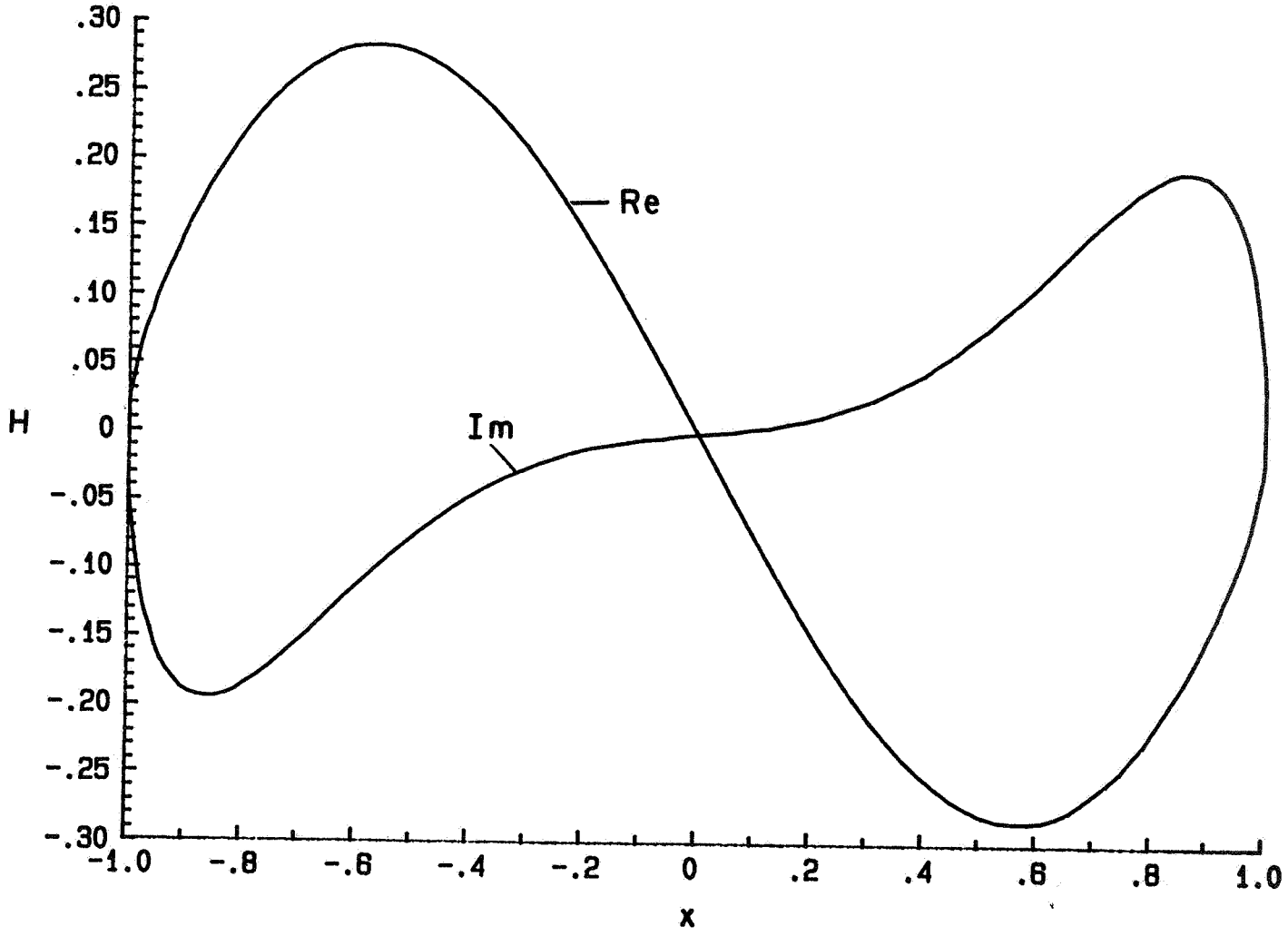

Figure 2.4-2c - Rotational Mode: τ=0.2, σ=10.

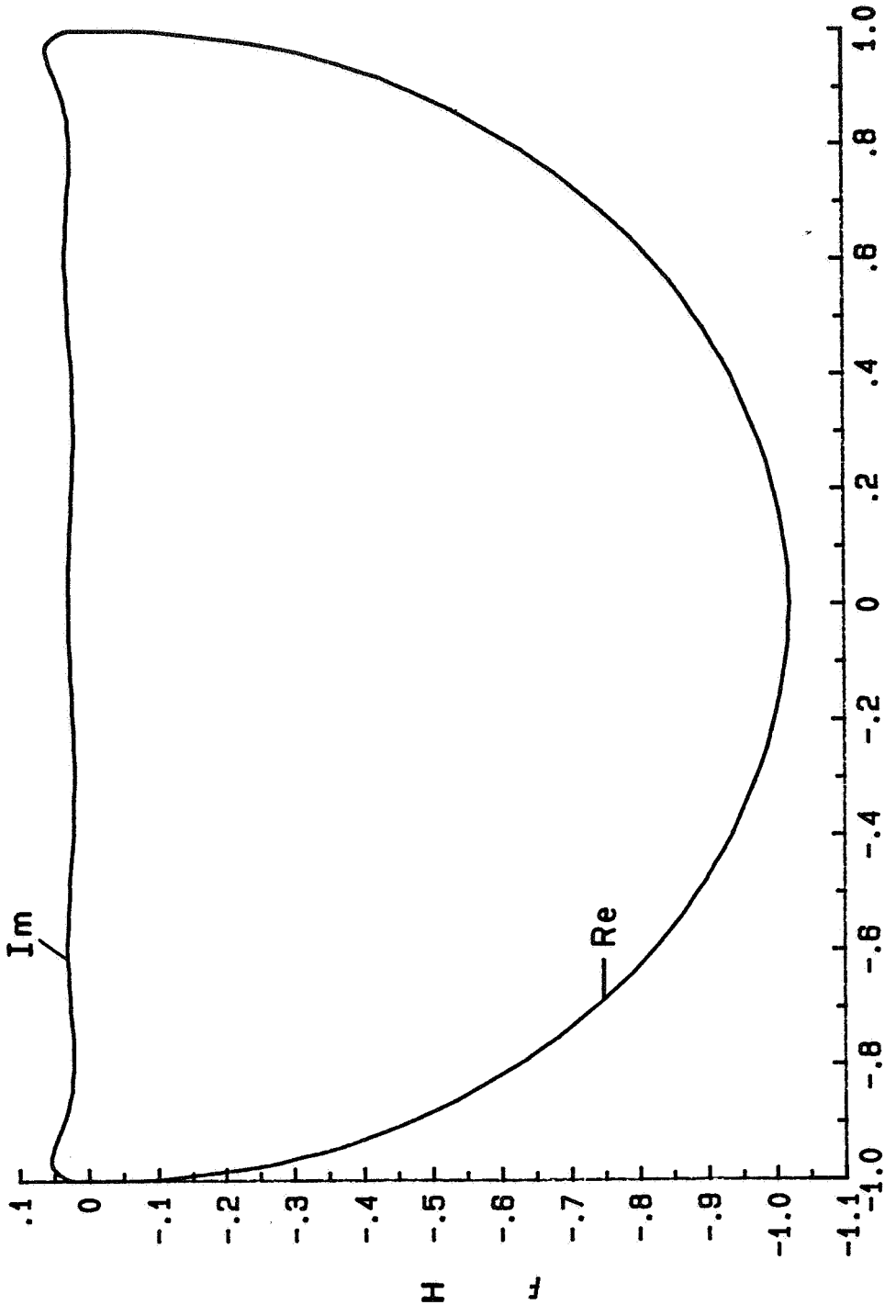

Figure 2.4-3a - Translational Mode; τ=0.1, σ=100.

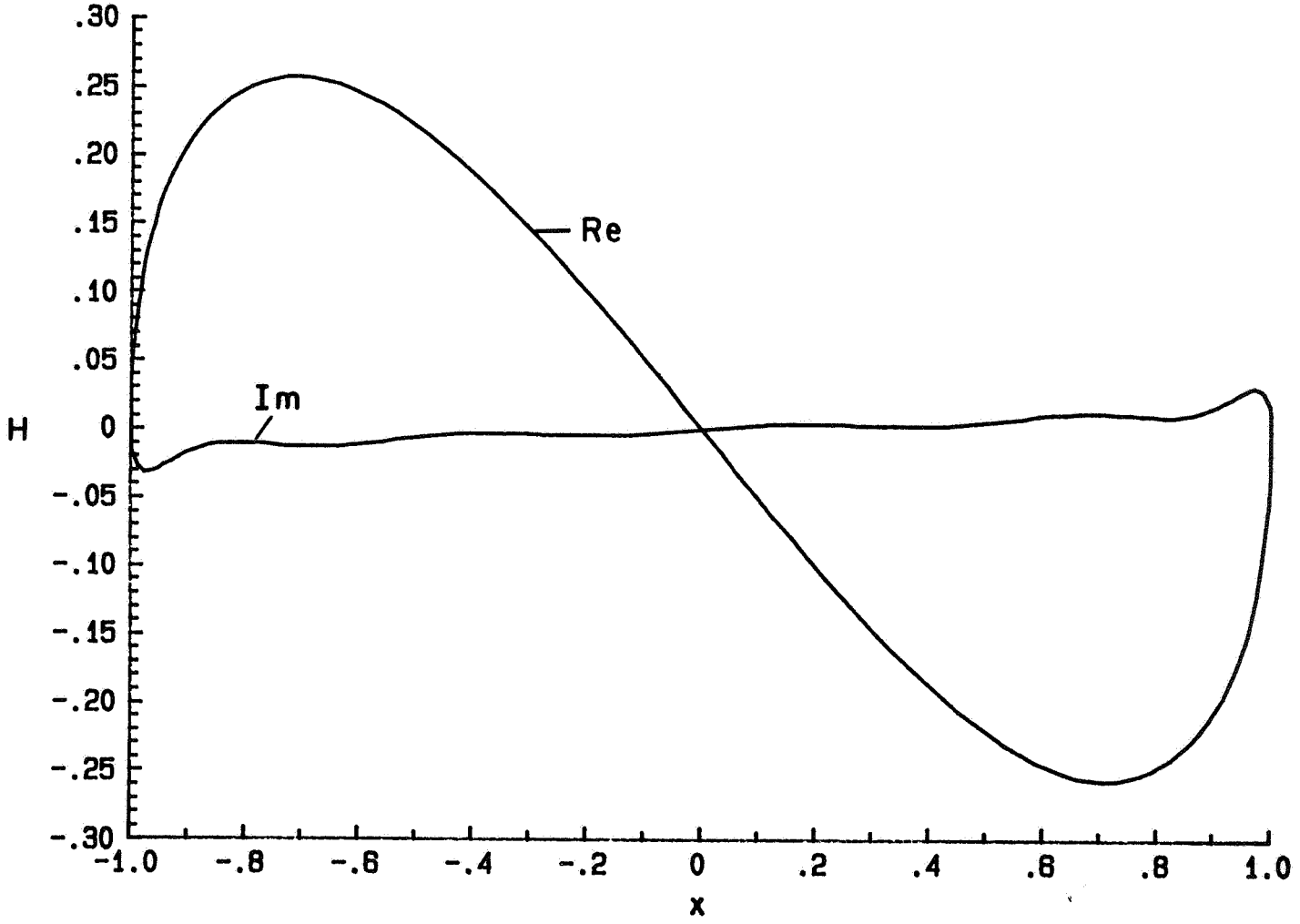

Figure 2.4-3b - Rotational Mode: τ=0.1, σ=100.

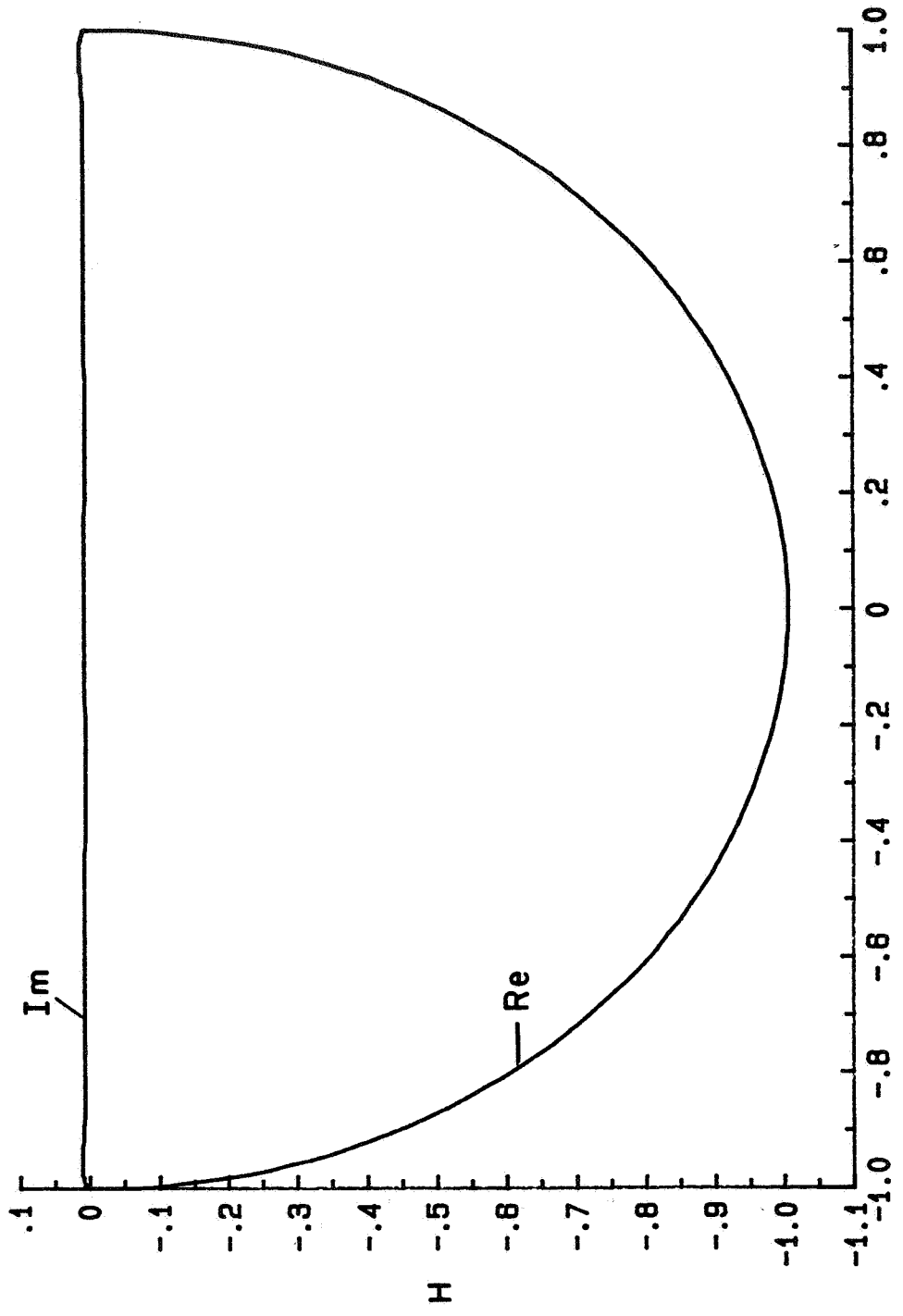

Figure 2.4-4a - Translational Mode: τ=0.1, σ=400.

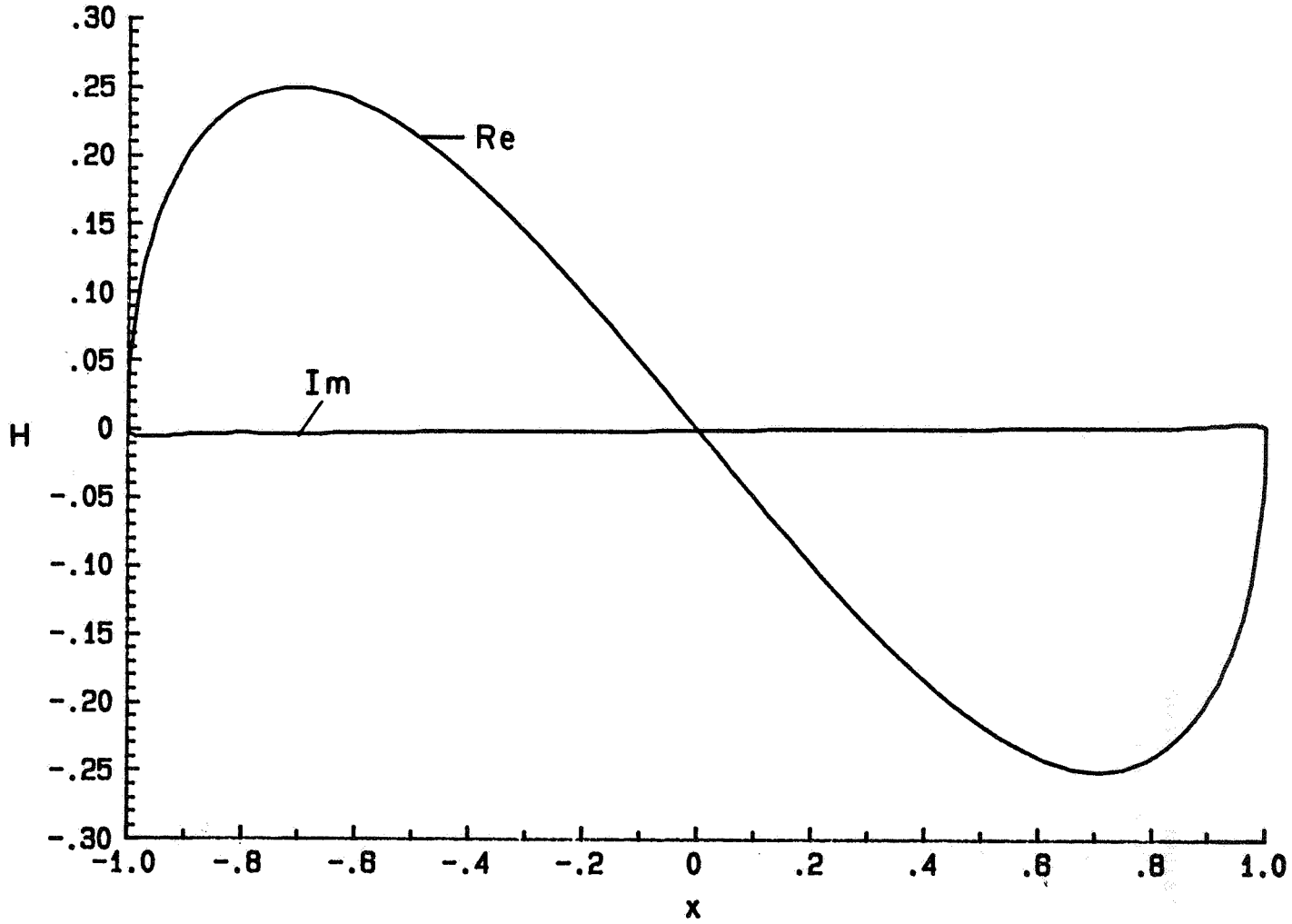

Figure 2.4-4b - Rotational Mode; τ=0.1, σ=400.

3. THREE-DIMENSIONAL INVISCID LOAD AND ACOUSTIC ANALYSIS OF A VIBRATING SURFACE

3.1 Basic Formulation

Consider the problem of a rigid three-dimensional airfoil section that vibrates harmonically with small amplitude in a compressible inviscid medium at rest. Referring to Fig. 3.1-1, the linearized mathematical problem can be stated as follows (see Eqs. (2.1.8) and (2.1.9)):

$$\frac{i\omega}{a^2} h' + \operatorname{div} \vec{v}' = 0 \quad , \quad h' = p'/\rho \tag{3.1.1}$$

$$i\omega\vec{v}' + \operatorname{grad} h' = 0 \tag{3.1.2}$$

where

$$\vec{n}_s^{\pm} \cdot \vec{v}' = i\omega \vec{n}_s^{\pm} \cdot \vec{d}_s' \quad , \quad |\tilde{x}| \leq c/2$$

$$|\tilde{y}| \leq b/2$$

$$\tilde{z} = \pm \frac{\tilde{h}(\tilde{x})}{2} \tag{3.1.3}$$

and

$$\vec{n}_s^{\pm} = \pm \vec{k} - \frac{\vec{i}}{2} \frac{d\tilde{h}(\tilde{x})}{d\tilde{x}} \tag{3.1.4}$$

$$\vec{d}_s' = \vec{k}(\tilde{h}_o - \alpha_o \tilde{x}) + \vec{i}\, \tilde{d}_o \tag{3.1.5}$$

All perturbation quantities h', $\vec{v}'$, $\vec{d}_s'$ are complex. The real time dependent quantity, q, that corresponds to any complex amplitude can be calculated with the relation

$$q = \operatorname{Re}(q' e^{i\omega t}) \tag{3.1.6}$$

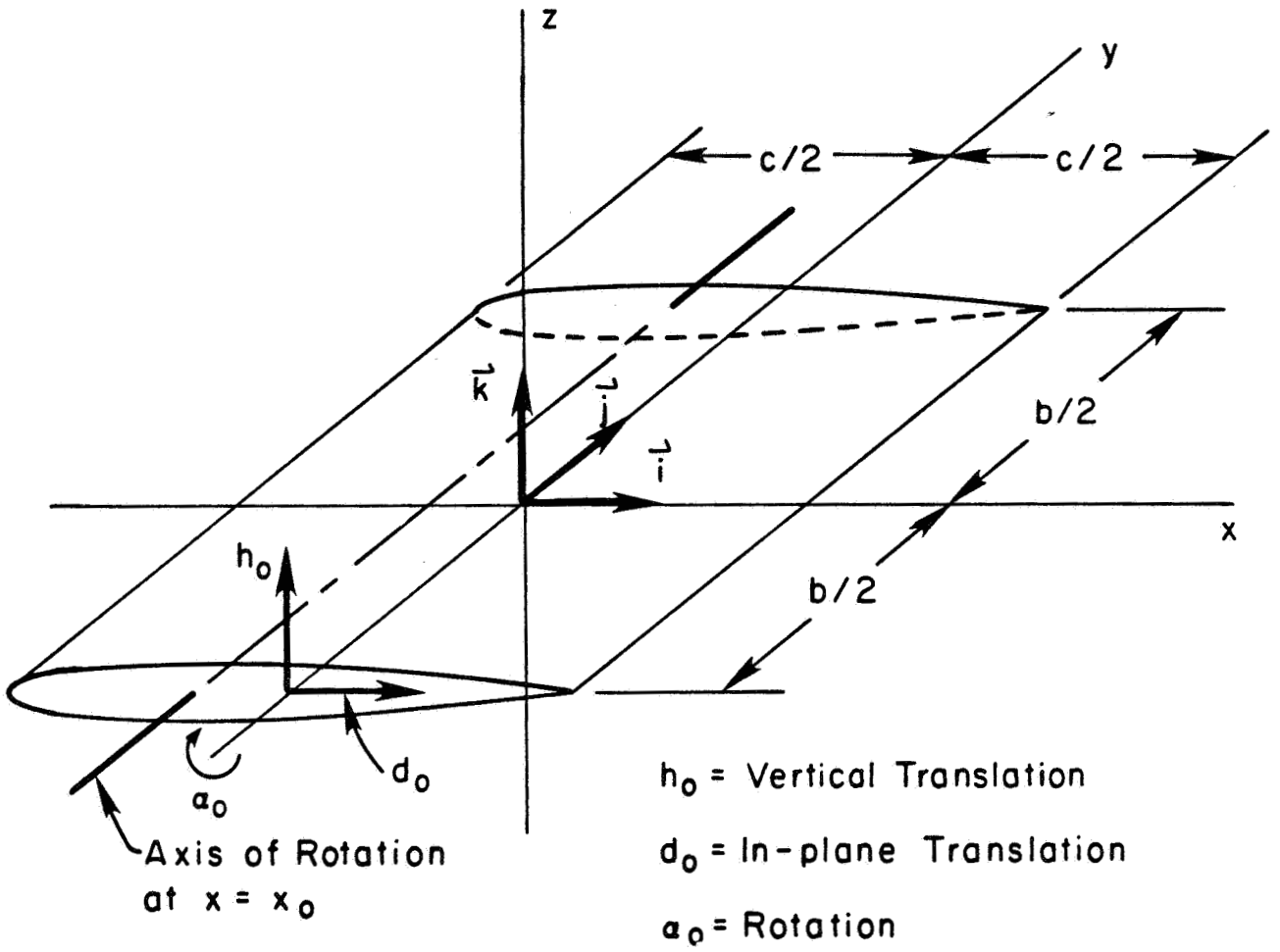

Figure 3.1-1 Coordinate System and Geometry of a Vibrating Airfoil.

The three rigid body modes of vibration that we consider are denoted by h_o, α_o, d_o with the following meaning:

h_o - translation along the z-axis

α_o - rotation about the y-axis (positive, nose up)

d_o - translation along the x-axis

In addition to the above equations, two auxiliary conditions are in general required to obtain a unique solution; i.e.,

1) Outgoing acoustic waves for $|\vec{x}| \sim \infty$.

2) Continuity of h' at the edges (Neumann condition) when needed to establish uniqueness.

To proceed with the solution of the foregoing problem, we first introduce dimensionless variables; i.e.,

$$(\tilde{x},\tilde{y},\tilde{z},\tilde{h}_o,\tilde{d}_o) = \frac{c}{2}(x,y,z,h_o,d_o)$$

$$\tilde{h}(\tilde{x}) = c\,\tau\, f(2\tilde{x}/c)$$

$$h' = \left(\frac{\omega c}{2}\right)^2 H\,, \quad \vec{v}' = \left(\frac{\omega c}{2}\right)\vec{V} \tag{3.1.7}$$

with

$$k = \frac{\omega c}{2a} \qquad \text{Helmholtz Number}$$

$$A = b/c \qquad \text{Aspect Ratio}$$

$$\tau = \text{Max}\ \tilde{h}(\tilde{x})/c \qquad \text{Thickness Ratio} \tag{3.1.8}$$

Equation (3.1.2) implies that h' is the potential of $i\omega\vec{v}'$, the complex acceleration, so that the velocity can be eliminated from the formulation. Also, we transfer the boundary condition (3.1.3) to the plane $z = 0\pm$. The final statement of the dimensionless problem becomes:

$$\nabla^2 H + k^2 H = 0 \tag{3.1.9}$$

$$\left.\frac{\partial H}{\partial z}\right|_{z=0\pm} = h_o - \alpha_o x \mp d_o \tau f'(x) \quad |x| \leq 1, \ |y| \leq A \tag{3.1.10}$$

$$H \sim \frac{e^{-ik|\vec{x}|}}{|\vec{x}|} \quad \text{for } |\vec{x}| \sim \infty \tag{3.1.11}$$

H continuous at the edges when a uniqueness condition is required (3.1.12)

Finally, we observe that the problem as formulated can be split into two parts:

1) Anti-symmetric Enthalpy (or Pressure) Mode

$$\left.\frac{\partial H}{\partial z}\right|_{z=0} = h_o - \alpha_o x \ , \ |x| \leq 1 \ , \ |y| \leq A \tag{3.1.13}$$

with

$$H(x,y,z) = - H(x,y,-z) \tag{3.1.14}$$

2) Symmetric Enthalpy (or Pressure) Mode

$$\left.\frac{\partial H}{\partial z}\right|_{z=0\pm} = \mp d_o \tau f'(x) \tag{3.1.15}$$

with

$$H(x,y,z) = H(x,y,-z) \tag{3.1.16}$$

The first problem is the result of combined translation along the z-axis and rotation about the y-axis while the second problem is the result of translation along the x-axis. We treat the two problems separately in the following discussion.

3.2 Solution of the Anti-Symmetric Transverse Vibration Problem

With the boundary condition (3.1.13), the anti-symmetric solution of (3.1.9) that satisfies the far field radiation condition (3.1.11) can be expressed as a surface distribution of dipoles oriented along the z-axis;

i.e.,

$$H(\vec{x}) = \frac{1}{4\pi} \iint d^2\vec{\xi}\; L(\vec{\xi})\, \frac{\partial}{\partial z} \frac{e^{-ik|\vec{x}-\vec{\xi}|}}{|\vec{x}-\vec{\xi}|} \tag{3.2.1}$$

where

$$L(\vec{\xi}) = H(x,y,0^-) - H(x,y,0^+) \tag{3.2.2}$$

and

$$\iint d^2\vec{\xi} \equiv \int_{-1}^{1} d\xi \int_{-A}^{A} d\eta \tag{3.2.3}$$

The acoustic far field relative to an origin of coordinates at $\vec{x}_0$ can be expressed in the following form:

$$H_f(\vec{y}) = -\frac{ik}{4\pi} \cdot (\vec{k}\cdot\hat{y}) \frac{e^{-ik(|\vec{y}|+\hat{y}\cdot\vec{x}_0)}}{|\vec{y}|} \cdot S(k\hat{y}) \tag{3.2.4}$$

where

$$S(k\hat{y}) = \iint d^2\vec{\xi}\; e^{ik\hat{y}\cdot\vec{\xi}}\, L(\vec{\xi}) \tag{3.2.5}$$

$$\vec{y} = \vec{x} - \vec{x}_0 \;, \quad \hat{y} = \vec{y}/|\vec{y}| \tag{3.2.6}$$

The unknown load distribution $L(\vec{\xi})$ satisfies a singular integral equation that we derive by applying the boundary condition (3.1.13) to the dipole representation (3.2.1); i.e.,

$$\frac{1}{4\pi} \iint d^2\vec{\xi}\; L(\vec{\xi})K(\vec{x}-\vec{\xi}) = -h_o + \alpha_o x \tag{3.2.7}$$

where

$$K(\vec{x}) = \left(\frac{\partial^2}{\partial x^2} + \frac{\partial^2}{\partial y^2} + k^2\right) \frac{e^{-ikR}}{R} \tag{3.2.8}$$

with

$$R = (x^2 + y^2)^{1/2} \tag{3.2.9}$$

The solution of (3.2.7) is not unique. However, we are interested in constructing a solution that satisfies the Neumann condition at all edges of the airfoil section. Thus, we assume a solution of the form

$$L(\vec{x}) = \frac{2}{\pi A^2} \sqrt{A^2-y^2}\ \sqrt{1-x^2} \cdot \alpha_o \cdot \sum_{n=1}^{\infty} L_n U_{n-1}(x) \qquad (3.2.10)$$

where $U_n(x)$ is the Chebyshev polynomial of the second kind; i.e.,

$$U_n(\cos\theta) = \frac{\sin(n+1)\theta}{\sin\theta}\ , \quad x = \cos\theta \qquad (3.2.11)$$

For convenience we assume the simple elliptic spanwise dependence of the load in (3.2.10). Calculation of the chordwise pressure distribution along the center of the airfoil is our primary concern (see discussion in Section 3.4)

With the assumed form of the load distribution we now derive an algebraic system of equations for the unknown load coefficients L_n as follows. Substitute (3.2.10) into (3.2.7), multiply the result by

$$-\frac{4}{\pi^2 A^2 \alpha_o} \sqrt{A^2-y^2}\ \sqrt{1-x^2}\ U_{m-1}(x) \qquad (3.2.12)$$

and integrate over the planform to obtain the following matrix equation for L_n.

$$\sum_{n=1}^{\infty} C_{mn} L_n = g_m\ , \quad m=1,2,\ldots \qquad (3.2.13)$$

where

$$g_m = -\frac{4}{\pi^2 A^2 \alpha_o} \iint dxdy\ \sqrt{A^2-y^2}\ \sqrt{1-x^2}\ U_{m-1}(x)\ (-h_o + \alpha_o x)$$

$$= x_o \delta_{m1} - \frac{1}{2}\delta_{m2} \qquad m=1,2,\ldots \qquad (3.2.14)$$

with

$$x_o = h_o/\alpha_o \ , \quad \text{(defines the axis of rotation, see Fig. 3.1-1)} \tag{3.2.15}$$

and

$$\delta_{mn} = 0 \quad m \neq n$$

$$= 1 \quad m = n \tag{3.2.16}$$

Also

$$C_{mn} = -\frac{1}{4\pi} \iint dxdy \cdot \frac{4}{\pi^2 A^2} \sqrt{A^2-y^2}\ \sqrt{1-x^2}\ U_{m-1}(x)$$

$$\cdot \frac{2}{\pi A} \iint d\xi d\eta\ \sqrt{A^2-\eta^2}\ \sqrt{1-\xi^2}\ U_{n-1}(\xi)\ K(x-\xi, y-\eta) \tag{3.2.17}$$

To evaluate C_{mn}, we introduce a double Fourier transform representation of the Kernel function; i.e.,

$$K(x,y) = -\frac{1}{2\pi} \iint d\alpha d\beta\ e^{i(\alpha x+\beta y)} \cdot \lambda \tag{3.2.18}$$

with

$$\lambda = (\alpha^2 + \beta^2 - k^2)^{1/2} \ , \quad \alpha^2 + \beta^2 \geq k^2$$

$$= i(k^2 - \alpha^2 - \beta^2)^{1/2} \ , \quad \alpha^2 + \beta^2 \leq k^2 \tag{3.2.19}$$

and

$$\iint d\alpha d\beta \equiv \int_{-\infty}^{\infty} d\alpha \int_{-\infty}^{\infty} d\beta \tag{3.2.20}$$

With the Fourier representation (3.2.18), the four-fold integral over the planform in (3.2.17) can be reduced to a two-fold integral over the Fourier space. Also, we note that C_{mn} is symmetric and zero unless m,n are both odd or both even. Thus, we can split (3.2.13) into two separate problems for the translation and rotation modes as follows:

Translation

$$\sum_{n=1,3}^{2N-1} C_{mn} L_n^{(h)} = x_o \cdot \delta_{m1} \quad , \quad m=1,3,\ldots 2N-1 \qquad (3.2.21)$$

Rotation

$$\sum_{n=2,4}^{2N} C_{mn} L_n^{(\alpha)} = -\frac{1}{2} \delta_{m2} \quad , \quad m=2,4,\ldots 2N \qquad (3.2.22)$$

The symmetric matrix elements C_{mn} can be reduced to the following set of integrals:

$$C_{mn} = \frac{4k^3}{\pi} \cdot m \cdot n (-1)^{\frac{m-n}{2}} \left[P_{mn}(k) + iQ_{mn}(k) \right]$$

$$P_{mn} = \int_o^\infty S_{mn}\,(k \cosh t) \cosh t \sinh^2 t \, dt$$

$$Q_{mn} = \int_o^{\pi/2} S_{mn}\,(k \sin t) \sin t \cos^2 t \, dt$$

$$S_{mn}(\rho) = \int_o^{\pi/2} d\theta \left[\frac{J_1(\rho A \sin\theta)}{\rho A \sin\theta} \right]^2 \frac{J_m(\rho \cos\theta) J_n(\rho \cos\theta)}{\rho^2 \cos^2\theta} \qquad (3.2.23)$$

The solution of (3.2.10) for the combined translation and rotation modes is constructed from the solution of (3.2.21) and (3.2.22) with

$$L_n = L_n^{(h)} \quad \text{for} \quad n \quad \text{odd}$$

$$= L_n^{(\alpha)} \quad \text{for} \quad n \quad \text{even} \qquad (3.2.24)$$

Both the surface enthalpy distribution and the far field can be calculated in terms of the load coefficients L_n. The resulting expressions are given below:

Surface Enthalpy

$$H_o(x,y) = H(x,y,0^+) = - L(x,y)/2$$

$$= - \frac{\alpha_o}{\pi A^2} \sqrt{A^2-y^2} \sum_{n=1}^{2N} L_n \sin n\,\theta \qquad (3.2.25)$$

with

$$\theta = \cos^{-1}x \quad , \quad 0 \leq \theta \leq \pi \qquad (3.2.26)$$

Far Field Enthalpy

Referring to Fig. 3.2-1, we evaluate the far field in the center plane of the airfoil ($y = 0$) at a fixed distance $|\vec{y}|$ from the center of rotation as a function of the directivity angle ψ. The result is

$$H_f = - \frac{\alpha_o e^{-ik(|\vec{y}|+x_o \cos\psi)}}{4|\vec{y}|} \cdot \tan\psi \sum_{n=1}^{2N} L_n \cdot n \cdot i^n J_n(k \cos\psi) \qquad (3.2.27)$$

To conclude this section we note the following formulae that enable us to translate any near or far field complex enthalpy distribution into a magnitude and phase angle and the magnitude into an r.m.s. pressure level in dB:

$$H = |H| e^{i\Phi} \qquad (3.2.28)$$

where H is any complex enthalpy, $|H|$ is the absolute value of H and Φ is the phase relative to the surface displacement at the leading edge. When we compare with data of Brooks, the phase will be shifted by π to refer it to the surface acceleration at the leading edge. Finally, we note that the root mean square (rms) pressure is given by

$$p'_{rms} = \frac{\gamma p k^2 |H|}{\sqrt{2}} \qquad (3.2.29)$$

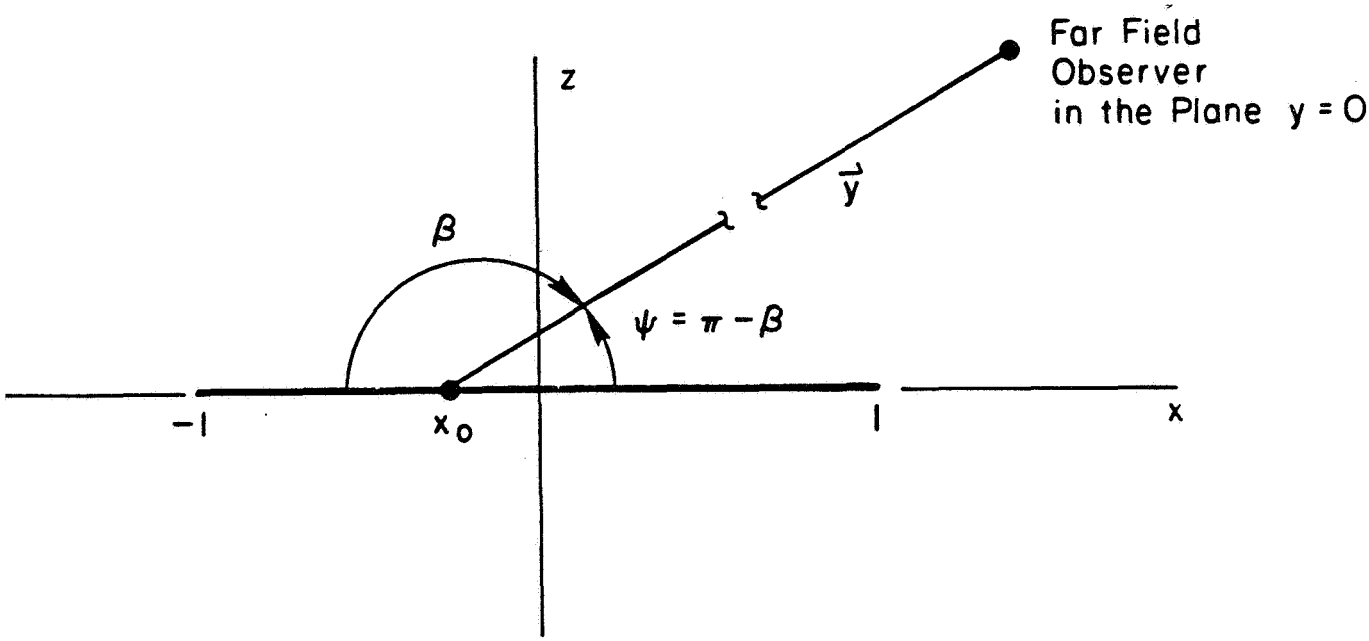

Figure 3.2-1 Acoustic Far Field Evaluation.

Let

$$P = 20 \log_{10} (p'_{rms}/p_{ref}) \quad (dB) \tag{3.2.30}$$

where $p_{ref} = 2 \times 10^{-4}$ dynes/cm^2, the standard reference pressure for dB. Substitute (3.2.29) into (3.2.30) to get

$$P = 20 \log_{10} \left(\frac{k^2 |H|}{2} \right) + 200 \quad (dB) \tag{3.2.31}$$

3.3 Solution of the Symmetric Problem (Thickness Noise)

With the boundary condition (3.1.15), the symmetric solution of (3.1.9) that satisfies the far field radiation condition (3.1.11) can be expressed as a surface distribution of dipoles oriented along the x-axis; i.e.;

$$H(\vec{x}) = \frac{d_o \tau}{2\pi} \iint d^2\vec{\xi}\, f(\xi) \frac{\partial}{\partial x} \frac{e^{-ik|\vec{x}-\vec{\xi}|}}{|\vec{x}-\vec{\xi}|} \tag{3.3.1}$$

where the dipole strength (determined by the boundary condition (3.1.15)) is proportional to the airfoil thickness distribution. Thus, the solution of the symmetric problem has been reduced to a double integral of known functions. The surface and far field enthalpy distributions are evaluated as follows:

Surface Enthalpy Distribution

It is convenient to integrate (3.3.1) by parts with respect to the ξ-coordinate, assuming that $f(\pm 1) = 0$. The resulting expression can then be evaluated on the actual surface to obtain

$$H_o(x,y) = H(x,y,\tau f(x))$$

$$= \frac{d_o \tau}{2\pi} \iint d\xi d\eta\, f'(\xi) \frac{e^{-ikR}}{R} \tag{3.3.2}$$

where

$$R = \left[(x-\xi)^2 + (y-\eta)^2 + \tau^2 f^2(x) \right]^{1/2} \tag{3.3.3}$$

For the NACA 0012 airfoil section used in the Brooks experiment, the section shape function and its derivative are given by the following analytic expression.

NACA Four-Digit Series Airfoils (Ref. 8)

$$f(x) = 1.4845\sqrt{s} - 0.63\,s - 1.758\,s^2 + 1.4215\,s^3 - 0.5075\,s^4 \tag{3.3.4}$$

$$f'(x) = \frac{0.371125}{\sqrt{s}} - 0.315 - 1.758\,s + 2.13225\,s^2 - 1.015\,s^3 \tag{3.3.5}$$

where

$$s = \frac{1 + x}{2} \tag{3.3.6}$$

For the Four-Digit series airfoils the surface enthalpy distributions can most readily be evaluated with the following integral expression:

$$H_o(x,y) = \frac{d_o\tau}{2\pi}\int_o^{\pi} f'(\cos\theta)\sin\theta\,d\theta \int_{-A}^{A} \frac{e^{-ikR}}{R}\,d\eta \tag{3.3.7}$$

where

$$R = \left[(x - \cos\theta)^2 + (y - \eta)^2 + \tau^2 f^2(x)\right]^{1/2} \tag{3.3.8}$$

Far Field Enthalpy Distribution

We use the integral solution (3.3.1) directly to evaluate the acoustic far field relative to the same origin of coordinates that we used in the anti-symmetric problem (see Fig. 3.2-1). Also, we evaluate the enthalpy on the plane y = 0. The result is

$$H_f = -ikd_o\frac{\tau A}{\pi}\,\frac{e^{-ik(|\vec{y}| + x_o\cos\psi)}}{|\vec{y}|}\cdot\cos\psi\cdot S(k\cos\psi) \tag{3.3.9}$$

where

$$S(\beta) = \int_0^{\pi} e^{i\beta \cos \theta} f(\cos \theta) \sin \theta \, d\theta \qquad (3.3.10)$$

and $f(\cos \theta)$ is given by (3.3.4) for the NACA Four-Digit Series airfoil section.

3.4 Comparison of Flat Plate Inviscid Theory with Experiment

The theoretical results presented in Appendix B are calculated with the solution of the Anti-Symmetric Problem in Section 3.2. The surface pressure and phase are calculated with (3.2.25) and the far field pressure is calculated with (3.2.27). The results are presented in exactly the same format as those of Brooks (Ref. 1) with the discrete symbols denoting the experimental results and the solid curves denoting the calculations of inviscid theory. The solid curve denoted "base line (A)" in each figure is calculated with the vibration amplitude (α_0) reported in the experiment and the actual geometric aspect ratio A = 0.666. The remaining solid curves differ by 2 dB increments and are convenient for reading off the differences between theory and experiment.

The dashed curve in each figure is calculated for an aspect ratio A* = 0.8 and is included for two reasons. First, we can deduce the sensitivity of the surface and far field pressure to changes in aspect ratio. Second, we suggest that the calculations based on A* can be compared directly with the experimental results. The reason is that we have used a single spanwise pressure mode shape of the form $\sqrt{1-(y/A)^2}$ to simplify our theoretical calculations. Emphasis has been placed on the representation of the chordwise load distribution. In Fig. 3.4-1 we compare the theoretical spanwise distribution with the experimental distributions (see Appendix A, Fig. A.3). For convenience we arbitrarily set the center line pressure to 100 dB. It is seen that the assumed theoretical elliptic load based on the actual aspect ratio decays more rapidly than the experimental load near the spanwise edges. The rational way to determine whether the theory will predict the spanwise load is to include more modes in the assumed spanwise load distribution. This task should be carried out at some point. A simple and somewhat ad hoc alternative is to adjust the single assumed spanwise mode with the aspect ratio parameter such that the integrals of the experimental and theoretical mode shapes are the same. This leads to the value A* = 0.8 and the intermediate load curve in Fig. 3.4-1. Also, in Fig. 3.4-2 we plot the peak surface and far field pressure as a function of aspect ratio for k = 1.255. The center line surface pressure is only increased by about 1 dB with the increase in aspect ratio while the far field pressure is increased by 3 dB. It is the authors opinion that the calculations with the single spanwise mode based on A* are more representative of the solution that would be obtained with more assumed modes. The important point is that the modifications only

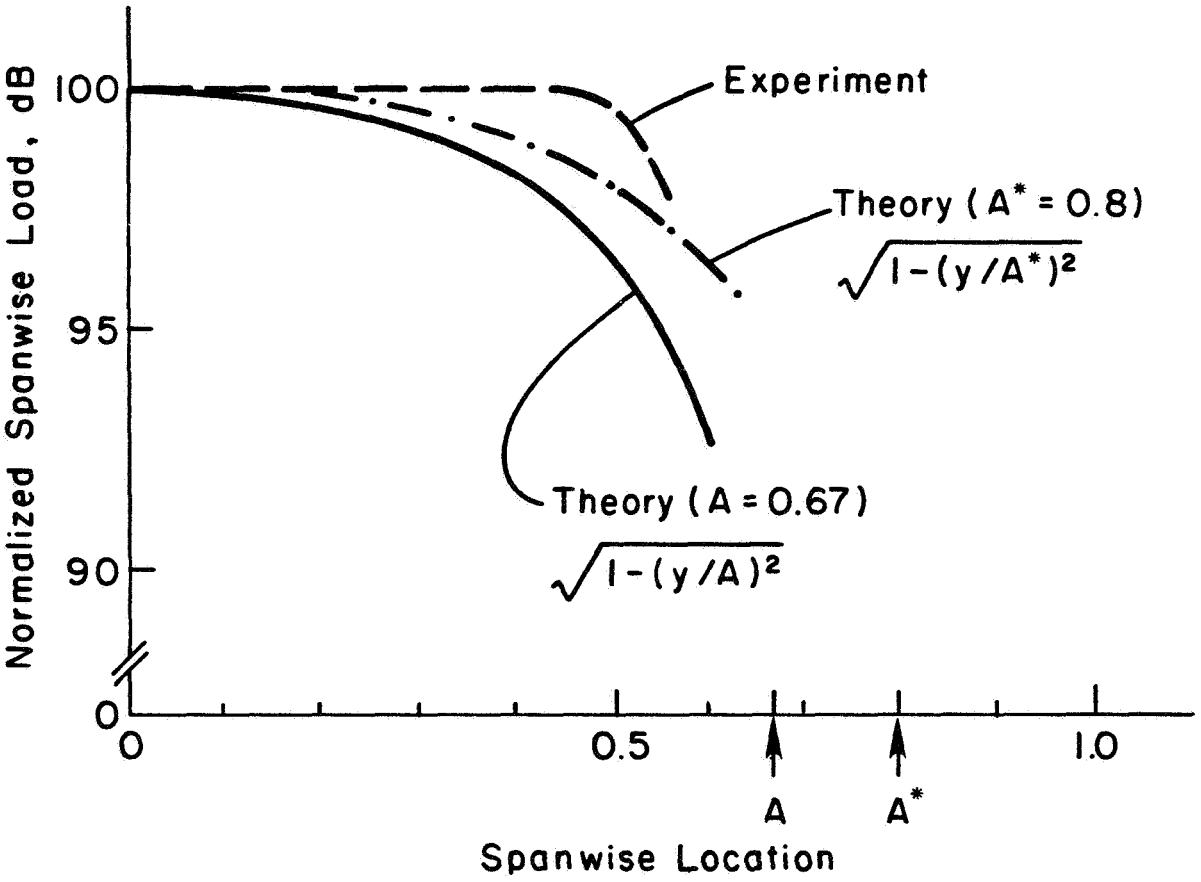

Figure 3.4-1 - Comparison of Theoretical and Experimental Spanwise Load Distributions.

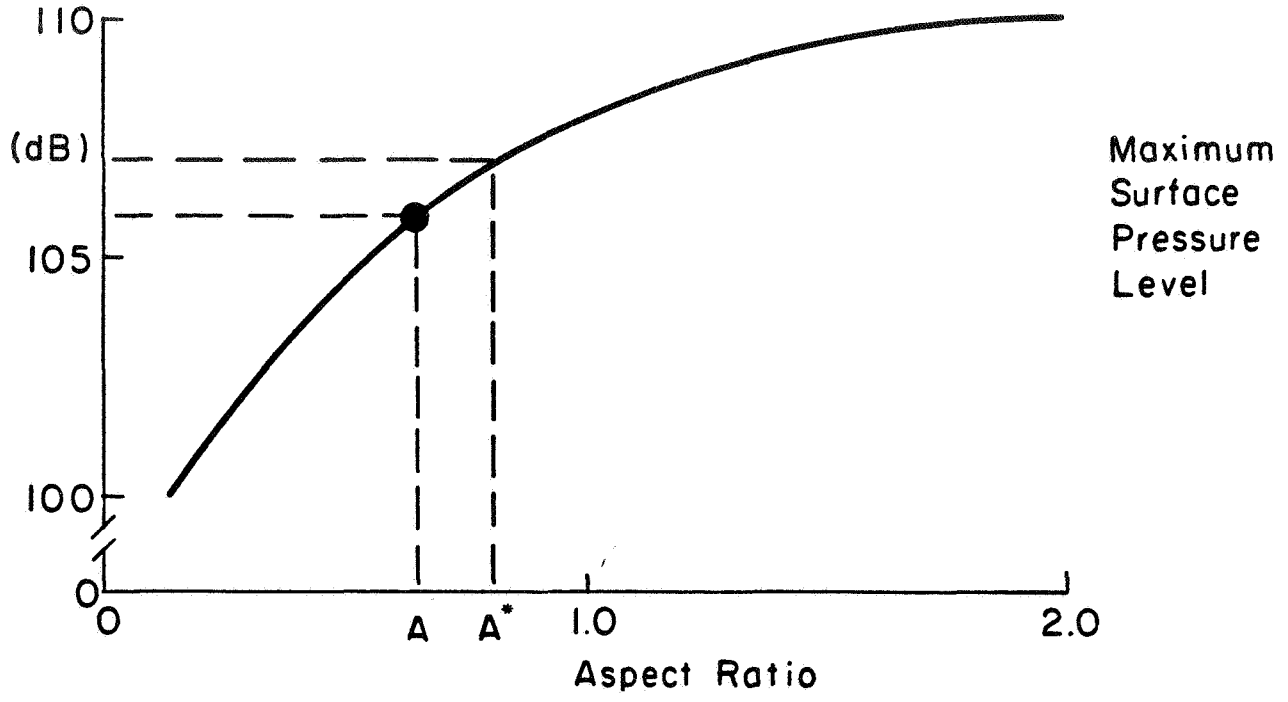

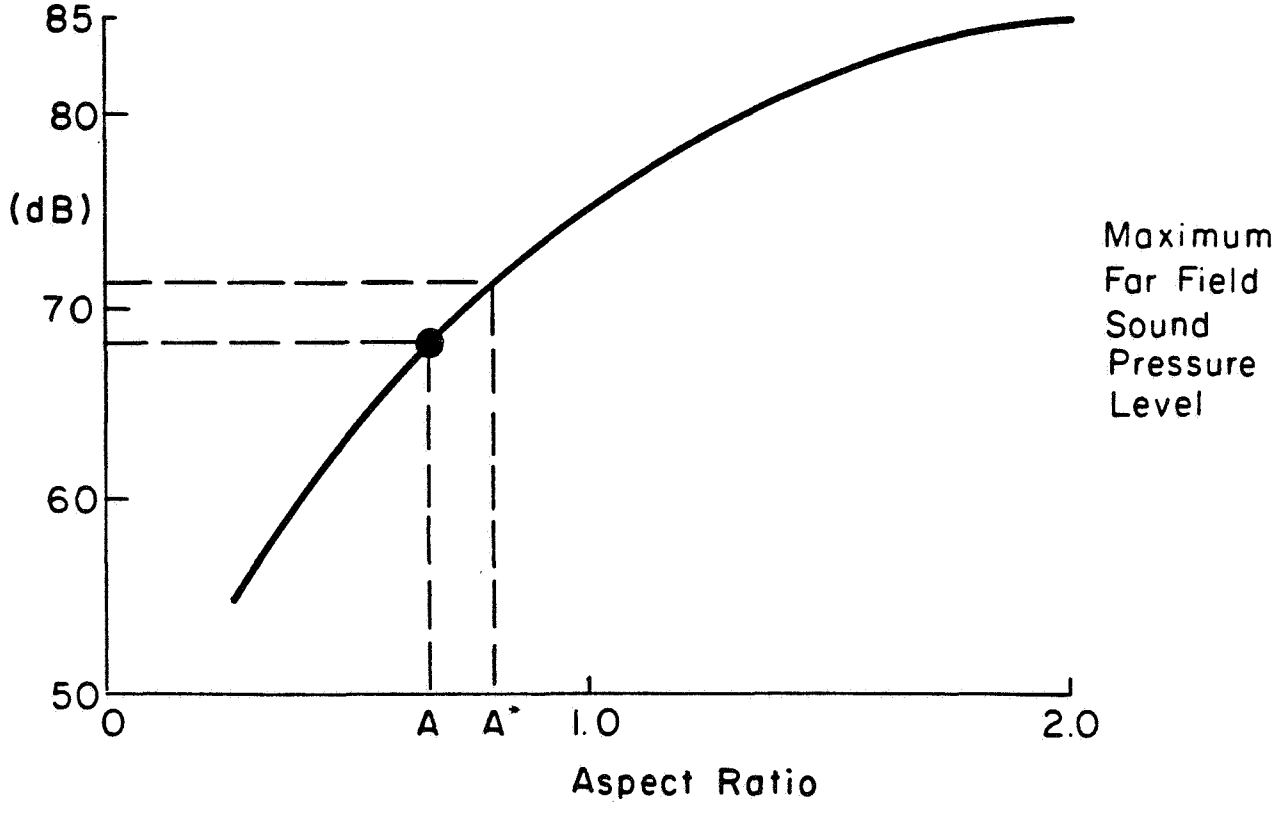

Figure 3.4-2 - Effect of Aspect Ratio on the Surface and Far Field Pressure.

affect the acoustic far field in any significant way with virtually no change in the centerline surface pressure.

Several qualitative differences between theory and experiment are noted:

1. Since we have built in a Neumann continuity condition, the theoretical edge loading is elliptic while the experimental behavior is more or less flat to within a few percent of the edges.

2. The surface pressure is underpredicted across the entire chord with the largest discrepancy appearing in the region forward of the axis of rotation.

3. With the aspect ratio A* the far field pressure amplitude is predicted within 1 or 2 dB. We also note that if we choose the curve of surface amplitude that is in best agreement with the measurements, then the corresponding far field amplitude is in excess of the experimental measurements. The inviscid calculation of Brooks also showed this behavior.

4. The phase calculations are in qualitative agreement with the measurements. However, the theory does not predict the far field phase blip near 150 deg that is present in all of the experimental data.

A summary of the quantitative differences between inviscid theory and experiment is presented in Table 3.1. The surface pressure amplitudes forward of the axis of rotation (leading edge) are 5 to 7 dB smaller than the measurements and the levels aft of the axis of rotation (trailing edge) are 3 to 5 dB smaller. These dB differences correspond to amplitude ratios of 1.5 to 2.5 and are totally unacceptable from the standpoint of an aerodynamic load calculation whether or not the aspect ratio correction is admitted. The far field sound pressure levels based on A* are only 1 or 2 dB smaller than the measured values, and the functional form of the calculated amplitude is in reasonably good agreement with the experimental results. With the geometric aspect ratio the far field sound pressure is underpredicted by 3 to 5 dB. The surface phase calculations are generally within 5 to 10 degrees of the measured values except for the case $k = 1.255$ with amplitude 82.1 μrad where the differences on the rearward part of the surface are 15 to 20 deg. The far field phase differences range from 10 to 20 degrees.

TABLE 3.1 SUMMARY OF DIFFERENCES BETWEEN INVISCID FLAT PLATE THEORY AND EXPERIMENT

Helmholtz Number (k)		1.255		1.989	
α_o (μrad)		82.1	259.3	30.8	97.6
Surface Amplitude (dB)	L.E.	5	7	6	6
	T.E.	3	5	4	4
Surface Phase (deg)		15-20	5-10	±10	±10
Far Field Amplitude (dB)	A*	0	2	1	1
Far Field Phase (deg)		20	10	10-15	10-15

The main conclusion of this section is that inviscid theory based on the measured antisymmetric vibration mode shape cannot predict the measured surface pressure. The far field sound pressure is predicted with satisfactory accuracy when calculated with A*. In the following sections we investigate two plausible explanations for the large differences between the experimental and theoretical surface pressures.

3.5 Effect of Acceleration on Surface Pressure Measurements

The point of view that we adopt in this and the following section is that inviscid theory (with the actual aspect ratio A) is capable of predicting the outcome of a surface vibration experiment. We then focus on two possible sources of experimental error. In this section we suppose that the surface pressure transducers measure a component of acceleration in addition to pressure. Since the two signals are nearly in phase, there must be an enhancement of measured surface pressure level. Also, since the acceleration increases linearly towards the leading and trailing edges, there will be a tendency to "flatten" out the expected edge load distribution. To estimate the effect of the supposed acceleration contamination, we add an arbitrary component of acceleration to the surface pressure or we can add an arbitrary component of displacement to the enthalpy given by (3.2.25); i.e.,

$$H_o^{(e)} = H_o + e \cdot \alpha_o \cdot (x-x_o) \tag{3.5.1}$$

where e is a measure of the level of acceleration contamination. Alternatively, we can write the transducer signal s' as a linear combination of pressure and acceleration; i.e.,

$$s' = p' + e' \ddot{\varepsilon}$$

$$= \rho\left(\frac{\omega c}{2}\right)^2 H_o + \varepsilon' \frac{c\omega^2}{2} \alpha_o (x - x_o)$$

$$= \rho\left(\frac{\omega c}{2}\right) [H_o + e \cdot \alpha_o (x - x_o)] \qquad (3.5.2)$$

with

$$e' = \frac{\rho\left(\frac{\omega c}{2}\right)}{\frac{c\omega^2}{2}} e$$

$$= 2.76 \quad \text{Pascals/g} \qquad (3.5.3)$$

The surface and far field calculations, based on the modified surface pressure (3.5.1) are compared in Appendix C. The conclusions are as follows. The peak surface pressure levels are clearly much closer to the edges (note the dashed lines), and the edge pressure distribution is much flatter when an acceleration component is added to the base line pressure. The value of e that gives the best agreement of measured and calculated surface pressure data is about .4 to .5 or e' = 1.08 to 1.35 Pascals/g. It should also be noted that the postulated acceleration contaminant brings the surface signals both fore and aft of the axis of rotation into much better agreement with the data. The far field sound pressure levels corresponding to the best fit of the near field (i.e., e = .4 to .5) are greater than the measured sound by 3 to 5 dB. It is important to keep in mind that if the measured surface pressure levels were contaminated by acceleration then it would be necessary to remove the error before calculating the far field.

In conclusion we remark that extensive calibration and acceleration sensitivity studies were made in preparation for the experiment (Brooks, private communication). Our estimated sensitivity value e' of the order of 1 Pascal/g is considered to be much too large.

3.6 Effect of In-Plane Vibration on the Surface Pressure and Far Field

One of the fundamental assumptions of the Brooks experiment is that the surface pressure amplitudes are identical on opposite sides of the airfoil but exactly 180 degrees out of phase. Unfortunately, the mode shape was measured with a single accelerometer near the leading edge that was oriented to measure only the transverse acceleration, the assumption being that the airfoil with its counterweights (see Appendix A, Fig. A.1) vibrates in a pure torsional mode about the axis of the attached shafts. The maximum amplitudes of vibration are of the order of 10^{-3} inches. It seems possible that due to misalignment of the counterweight shafts that the vibration mode is actually a coupled torsion and in-plane bending vibration mode. This would require, of course, that the resonant frequency of the pure in-plane bending mode be very close to the torsional frequency. These speculations could be checked with a simple vibration analysis or with a measurement of the in-plane acceleration. A recommendation to this end will be made in Section 5. Here we examine the consequences of adding an arbitrary component of in-plane vibration to the transverse vibration mode. The important point is that such a vibration mode leads to a component of surface pressure that is in phase on opposite sides of the airfoil. If an in phase component were present in the Brooks experiment, the corresponding surface pressure would have been treated as a lateral dipole because of the assumed symmetry. Thus, it is doubly important that both the vibration mode and the surface pressure be measured to check the assumed symmetry.

To calculate the effect of in-plane vibration we combine the results of Sections 3.2 and 3.3. Thus,

$$H_o = H_o^{(\ell)} + e\, H_o^{(a)} \qquad \text{Surface} \tag{3.6.1}$$

$$H_f = H_f^{(\ell)} + e\, H_f^{(a)} \qquad \text{Far Field} \tag{3.6.2}$$

where $H_o^{(\ell)}$ and $H_o^{(a)}$ are given by (3.2.25) and (3.3.7), respectively, and $H_f^{(\ell)}$ and $H_f^{(a)}$ are given by (3.2.27) and (3.3.9). The factor e in the present calculation is the precentage of the in-plane vibration mode. The results of the combined calculation are presented in Appendix D. The base line curve with e = 0 is indicated on each graph. The successive curves are presented for increments of e = 0.2. Note that a value of e = 1.0 means that the amplitude of in-plane vibration is equal to the lateral displacement at the trailing edge due to the torsion mode. The calculations were carried out for the NACA 0012 airfoil. The pressure singularity at the leading edge is due to the infinite slope of the thickness distribution and could be removed. The significant point is that the surface pressure levels can be increased by in-plane vibration with the largest increase forward of the hinge axis. On the other hand, the far field amplitude is not changed appreciably except for relatively large

values of in-plane displacement. Also, the surface phase is relatively insensitive to the in-plane modal amplitude but there is an effect on the far field phase.

It is not intended that the calculations presented in Appendix D be compared directly with the experimental results to draw concrete conclusions. We do not know what portion of the modal amplitude, if any, is due to in-plane motion or what its phase may be relative to the torsional motion. We present these results to draw attention to the fact that in-plane vibration could lead to an enhancement of the surface pressure with a much flatter edge loading like the one that was measured. A vibration analysis and further measurements, will be essential to verify or discount the supposition considered in this section.

4. ANALYSIS OF A VIBRATING SURFACE OF ZERO THICKNESS IN A COMPRESSIBLE VISCOUS FLUID MEDIUM IN UNIFORM MOTION

4.1 Statement of the Problem

In Section 2, we have shown, via a viscous analysis for finite thickness airfoils, that the Neumann edge condition is applicable as a uniqueness criterion for inviscid analysis when the Stokes number σ is of order 100 or greater. (The Stokes number is of order 3000 in the Brooks experiment, see Appendix A.) In Section 3, we showed that the inviscid analysis with Neumann edge conditions cannot predict the surface pressure measurements of the Brooks experiment. The alternative is that either something has been overlooked in the viscous analysis or in the experiment. We further discussed two possibilities for experimental error. In the following, we re-examine the zero thickness problem for a compressible viscous medium with a low speed flow that could, for example, be maintained by acoustic streaming. The relationship between the surface load and shed vorticity is our main concern. Direct load calculations will not be made. In addition, we examine the energy balance in the presence of flow and generalize the arguments developed previously (Ref. 2) that led us to consider the viscous problem.

The mathematical problem is obtained by a straightforward generalization of (2.1.8) and (2.1.9). We replace the local time derivative by the linearized convective derivative; i.e.,

$$\frac{\partial}{\partial t} \to \frac{\partial}{\partial t} + v_\infty \frac{\partial}{\partial x} \tag{4.1.1}$$

where v_∞ is an assumed low speed flow. With the same dimensionless variables used in Sections 2 and 3, we obtain the following simple harmonic boundary value problem:

$$k^2 \frac{DH}{Dx} + \mathrm{Div}\ \vec{V} = 0 \tag{4.1.2}$$

$$\frac{D\vec{V}}{Dx} + \mathrm{Grad}\ H = -\frac{1}{\sigma^2} \mathrm{Curl}(\mathrm{Curl}\ \vec{V}) \tag{4.1.3}$$

with

$$\frac{D}{Dx} = s \frac{\partial}{\partial x} + i \tag{4.1.4}$$

$$s = \frac{2v_\infty}{\omega c} \tag{4.1.5}$$

and the boundary conditions

$$\left.\begin{aligned} \vec{k}\cdot\vec{V} &= -i\alpha_o(x-x_o) \\ \vec{k}\times\vec{V} &= 0 \end{aligned}\right\} \quad |x| \leq 1, \quad |y| \leq A, \quad z = 0 \pm \tag{4.1.6}$$

Also, we derive the following second order dimensionless energy balance by cross multiplying (4.1.2) and (4.1.3) with H* and $\vec{V}$* (complex conjugates of H and V) and integrating over a large spherical volume $|\vec{x}| < r_o$. The result is

$$\mathscr{W}_o = \mathscr{P}_a + \mathscr{P}_v \tag{4.1.7}$$

where

$$\mathscr{W}_o = \iint dxdy\cdot\alpha_o(x-x_o)\cdot \text{Im } L \qquad \text{Surface Work} \tag{4.1.8}$$

$$\mathscr{P}_a = \int_{\vec{x}=r_o>>1} dS\ \text{Re}(H_f^* V_r) \qquad \text{Radiated Acoustic Energy} \tag{4.1.9}$$

$$\mathscr{P}_v = \frac{1}{\sigma^2}\int_{|\vec{x}|<r_o} dV\ |\vec{\Omega}|^2 \qquad \text{Dissipated Vortical Energy} \tag{4.1.10}$$

All symbols have the same meaning as in Sections 2 and 3.

4.2 Representation of the Solution in Fourier Space

Following the analysis of Section 3, we first derive a representation of the solution of Eqs. (4.1.2) and (4.1.3) in Fourier space. These results are used in the subsequent section to derive a relation for the dissipation and an expression for the shed vorticity in terms of the load. Introduce the double Fourier transform pair; i.e.,

$$\mathscr{F}_{oq} \equiv q^+(\alpha,\beta) = \iint dxdy\ e^{-i(\alpha x+\beta y)}\ q(x,y) \tag{4.2.1}$$

$$\mathscr{F}^{-1}{}_{oq^+} \equiv q(x,y) = \frac{1}{(2\pi)^2}\iint d\alpha d\beta\ e^{i(\alpha x+\beta y)}\ q^+(\alpha,\beta) \tag{4.2.2}$$

Then transform Eqs. (4.1.2) and (4.1.3) and seek a solution of the form

$$q^+ = q^+ e^{-\lambda|z|} \tag{4.2.3}$$

There are two modes with which we can construct a complete representation of the solution; i.e.,

$$\lambda_o = [\alpha^2 + \beta^2 + i\sigma^2(1+\alpha s)]^{1/2} \qquad \text{Viscous} \tag{4.2.4}$$

$$\lambda_1 = [\alpha^2 + \beta^2 - k^2(1+\alpha s)^2]^{1/2} \qquad \text{Compressible} \tag{4.2.5}$$

If L^+ denotes the transform of the surface load distribution, then we have the following representation of the transformed solution:

Enthalpy

$$H^+ = -\frac{L^+}{2} e^{-\lambda_1|z|} \operatorname{sgn} z \tag{4.2.6}$$

Velocity

$$U^+ = -\frac{\alpha L^+}{2(1+\alpha s)}\left(e^{-\lambda_o|z|} - e^{-\lambda_1|z|}\right) \operatorname{sgn} z \tag{4.2.7}$$

$$V^+ = -\frac{\beta L^+}{2(1+\alpha s)}\left(e^{-\lambda_o|z|} - e^{-\lambda_1|z|}\right) \operatorname{sgn} z \tag{4.2.8}$$

$$W^+ = \frac{L^+}{2i(1+\alpha s)} \frac{\alpha^2+\beta^2}{\lambda_o}\left(e^{-\lambda_o|z|} - \lambda_1 e^{-\lambda_1|z|}\right) \tag{4.2.9}$$

Vorticity

$$\Omega_x^+ = \frac{\beta\sigma^2 L^+}{2i\lambda_o} \cdot e^{-\lambda_o|z|} \tag{4.2.10}$$

$$\Omega_y^+ = -\frac{\alpha\sigma^2 L^+}{2i\lambda_o} \cdot e^{-\lambda_o|z|} \tag{4.2.11}$$

$$\Omega_z^+ = 0 \tag{4.2.12}$$

If we invert Eq. (4.2.9) for the z component of velocity and evaluate the result on the plane $z = 0^+$, we obtain the following:

Integral Equation for the Transformed Load

$$\frac{1}{2(2\pi)^2} \oint d\alpha d\beta \; e^{i(\alpha x+\beta y)} \cdot \frac{L^+}{(1+\alpha s)} \left(\lambda_1 - \frac{\alpha^2+\beta^2}{\lambda_o}\right) = -\alpha_o(x-x_o) \tag{4.2.13}$$

where the boundary condition (4.1.6) has been used to evaluate the right hand side.

We do not propose to solve the integral equation (4.2.13). Rather, our objective is to calculate the shed vorticity and dissipation in terms of the load distribution and to provide an energy budget for the experiment.

4.3 Distribution of Spanwise Vorticity

In this section we derive an expression for the total spanwise vorticity that is shed from the trailing edge in the presence of a low speed flow for a load distribution of the form

$$L(x,y) = \frac{2}{\pi A^2} \sqrt{A^2-y^2} \cdot L(x) \tag{4.3.1}$$

with

$$L(x) = P(x)\,(1-x)^{\varepsilon} \tag{4.3.2}$$

where P(x) is bounded near the trailing edge for some value of ε. Thus

$$P(1) = \lim_{x\to 1} \frac{L(x)}{(1-x)^{\varepsilon}} \quad \text{for some} \quad \varepsilon \tag{4.3.3}$$

Furthermore, we calculate the following weighted average of the total spanwise vorticity; i.e.,

$$\gamma(x) = \frac{3\pi^2}{2A} \cdot \int_{-A}^{A} \sqrt{A^2-y^2} \cdot \gamma_y \, dy \tag{4.3.4}$$

where

$$\gamma_y = \int_{-\infty}^{\infty} \Omega_y \, dz \quad , \quad \Omega_y = \mathcal{F}^{-1} \circ \Omega_y^+ \tag{4.3.5}$$

With (4.2.11) we get

$$\gamma_y^+ = \frac{i\alpha\sigma^2 L^+}{\lambda_o^2} \tag{4.3.6}$$

and with (4.3.1) and (4.3.4) we obtain

$$\gamma(x) = \frac{3\pi A\sigma^2}{4} \frac{\partial}{\partial x} \int_{-\infty}^{\infty} e^{i\alpha x} L^+(\alpha) d\alpha \cdot \int_{-\infty}^{\infty} \left(\frac{J_1(\beta A)}{\beta A}\right)^2 \frac{d\beta}{\lambda_o^2} \tag{4.3.7}$$

For large Stokes number ($\sigma >> 1$) the double integral can be evaluated asymptotically; i.e.,

$$\gamma(x) = 2\sigma^2 \frac{\partial}{\partial x} \cdot \int_{-\infty}^{\infty} e^{i\alpha x} \frac{L^+(\alpha) d\alpha}{\alpha^2 + i\sigma^2(1+\alpha s)} \tag{4.3.8}$$

The last integral can be expressed as a convolution of the load with exponential functions that correspond to the roots of the denominator. The final result for the total vorticity downstream of the trailing edge is

$$\gamma(x) = -\frac{\sigma\lambda}{p \cdot q} \cdot \int_{-1}^{1} L(\xi) e^{-\lambda(1-\xi)} d\xi \cdot e^{-\lambda(x-1)} \quad , \quad x > 1 \tag{4.3.9}$$

where

$$\lambda = \sigma p(q-1) \tag{4.3.10}$$

$$p = \frac{\sigma s}{2} = \frac{1}{2}\frac{V_\infty}{\sqrt{\omega\nu}} \tag{4.3.11}$$

$$q = \left(1 + i/p^2\right)^{1/2} \tag{4.3.12}$$

The last result has been derived under the condition that $\sigma >> 1$ and $p = O(1)$. Finally, we use the asymptotic form of the load distribution near the trailing edge (4.3.2) to evaluate (4.3.9) for large λ. We get

$$\gamma(x) = -\frac{\sigma\lambda}{p\cdot q}\cdot P(1)\cdot e^{-\lambda(x-1)}\int_{-1}^{1}(1-\xi)^{\varepsilon}\, e^{-\lambda(1-\xi)}\, d\xi$$

$$= -\frac{\sigma P(1)\Gamma(1+\varepsilon)}{p\cdot q\ \lambda^{\varepsilon}}\cdot e^{-\lambda(x-1)}\quad,\quad x \geq 1 \tag{4.3.13}$$

where $\Gamma(z)$ is the gamma function. The total vorticity downstream of the trailing edge is

$$\Gamma = \int_{1}^{\infty}\gamma(x)dx$$

$$= -\frac{1}{\sigma^{\varepsilon}}\ \frac{P(1)\Gamma(1+\varepsilon)}{p\cdot q[p(q-1]^{1+\varepsilon}} \tag{4.3.14}$$

For all edge loads that tend to zero (i.e., $\varepsilon > 0$) the total shed vorticity decreases with increasing Stokes number and is of $O(1/\sigma^{\varepsilon})$. For a constant edge load (i.e., $\varepsilon = 0$), the total shed vorticity is only a function of the speed ratio and is of $O(1)$.

Typical results for the decay of wake vorticity are presented in Figs. 4.3-1a, 1b, 1c for $p = 0,1,2$. The abscissa is the product of Stokes number and distance downstream in semi-chords. For the Brooks experiment with $\sigma \approx 3000$, the actual downstream extent of the entire wake structure is of O(.002, .016, .1) semi-chords, respectively for the three values of p. If the assumed streaming velocity is of the order of the trailing edge velocity of vibration, then the experimental value of p is at most about 0.35 based on data in Appendix A, Table A.2. Thus, the entire wake structure decays within a distance of about .01 semi-chords.

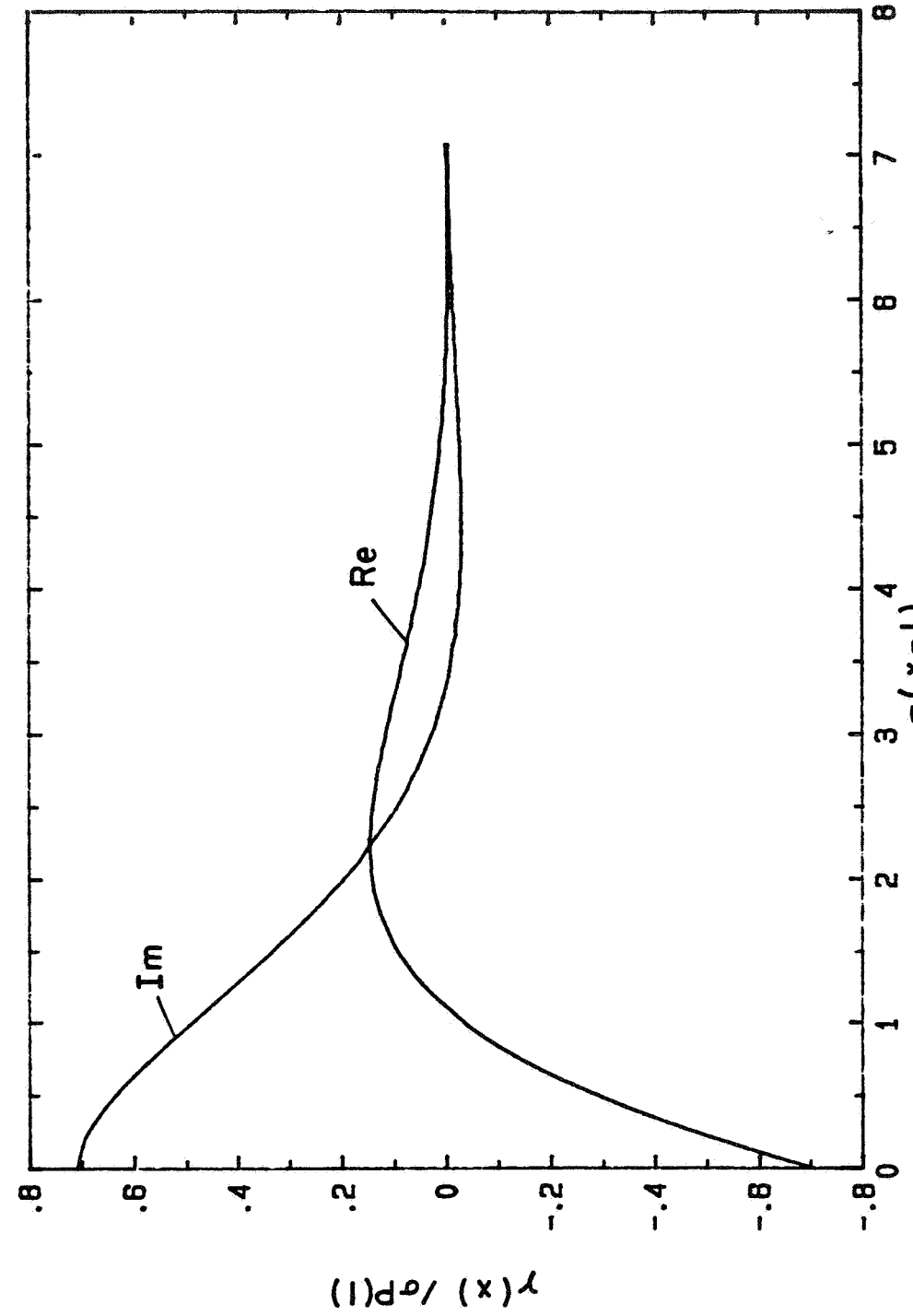

Figure 4.3-1a - Convective Decay of Wake Vorticity for a Flat Trailing Edge Load; p=0 (No Flow).

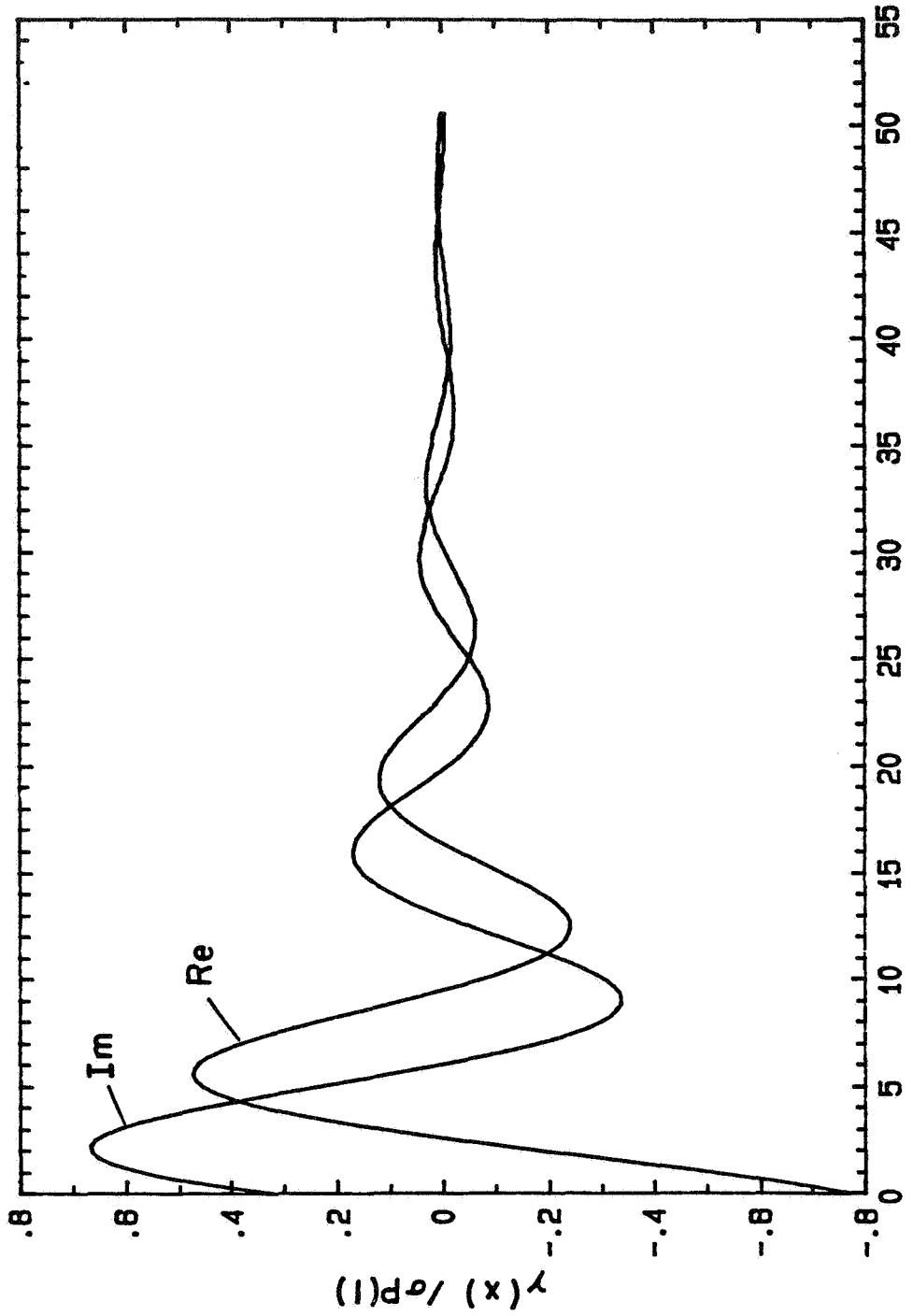

Figure 4.3-1b - Convective Decay of Wake Vorticity for a Flat Trailing Edge Load; p=1.0.

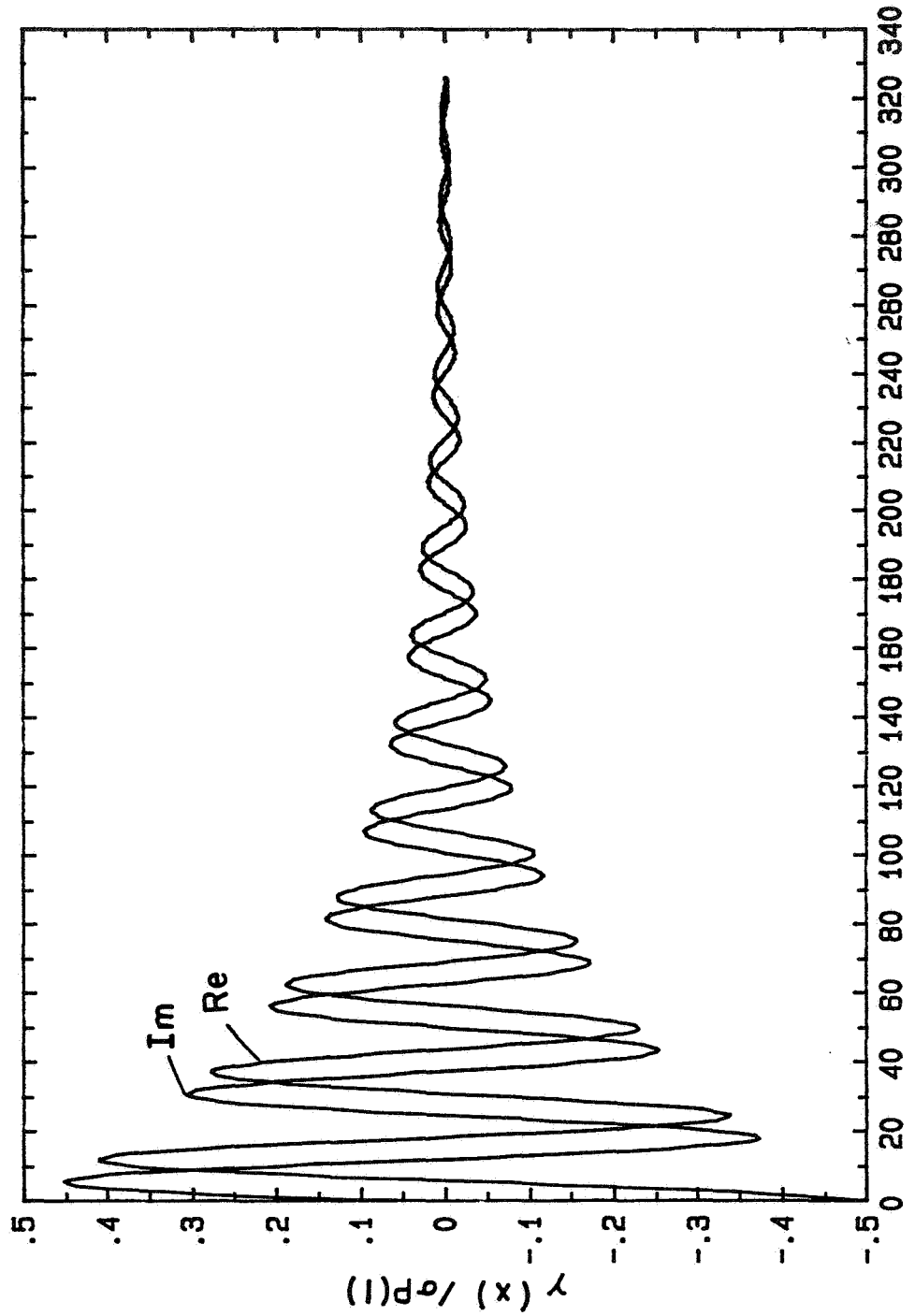

Figure 4.3-1c - Convective Decay of Wake Vorticity for a Flat Trailing Edge Load; p=2.0.

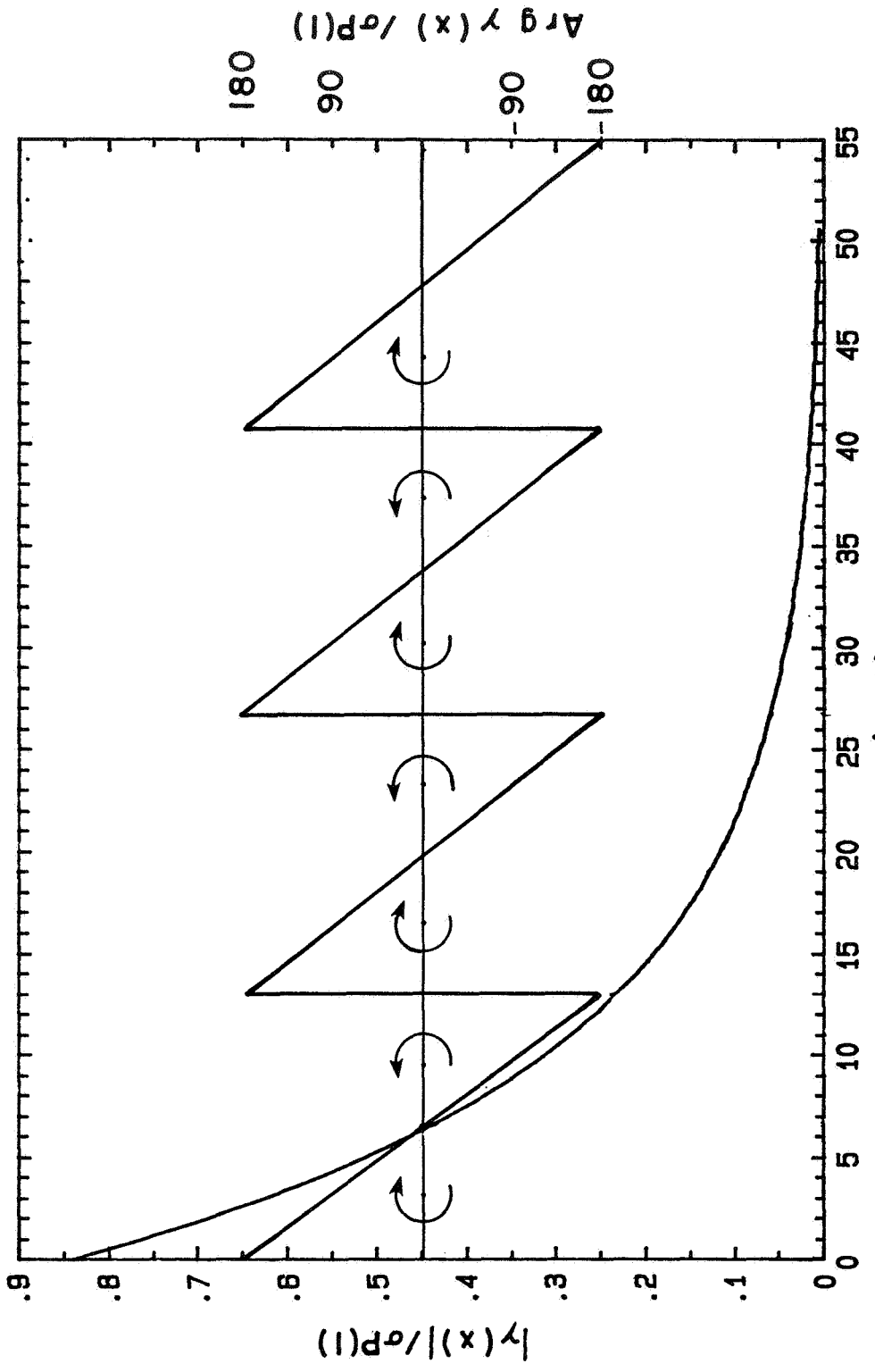

Figure 4.3-2 - Variation of Amplitude and Phase of Shed Vorticity; p=1.0
(Compare Figure 4.3-1b).

The results in Fig. 4.3-2 are presented in the form of amplitude and phase for $p = 1$ and $\varepsilon = 0$. The amplitude decays exponentially downstream while the phase increases linearly. Thus the wake can be envisioned as a train of discrete vortices that convect at constant speed, v_∞, and decay (dissipate) with increasing distance. The magnitude of the first or starting vortex is proportional to $\sigma^{1-\varepsilon}$. Thus, we conclude what is intuitively obvious that a flat edge load ($\varepsilon = 0$), if it can exist, must have a vortex that is $\sqrt{\sigma}$ stronger than a trailing edge that is elliptically loaded ($\varepsilon = 1/2$).

4.4 Energy Balance

In Ref. 2 we presented an argument for the internal consistency of the Brooks surface and far field data. We estimated the viscous dissipation and far field acoustic energy. For the Helmholtz numbers of the Brooks experiment and the measured load distributions, the surface work is almost equally partitioned into sound and vortical energy (see Ref. 2). The argument is based on two-dimensional analysis and the conclusions based on the energy argument led to our subsequent studies of the surface load with the viscous theory. As reported in Section 2, the theory has been unsuccessful in reproducing the Brooks edge loading and always leads to the same conclusion; i.e., the Neumann condition with inviscid theory is a valid approach. The puzzle still remains, however, and we want to reexamine the energy argument in this section with the complete three-dimensional compressible viscous theory. In particular, we estimate the surface work $\mathscr{W}_o$, the radiated acoustic energy $\mathscr{P}_a$ and the dissipated vortical energy $\mathscr{P}_v$. The appropriate dimensionless formulae are given by Eqs. (4.1.8), (4.1.9), and (4.1.10). The dimensional work or energy can be calculated with the formula

$$\mathscr{P}^{dim} = \frac{\rho a^3}{2}\left(\frac{c}{2}\right)^2 \cdot k^3 \cdot \mathscr{P}^{non\text{-}dim} \tag{4.4.1}$$

where $\mathscr{P}^{non\text{-}dim}$ is either of $\mathscr{W}_o$, $\mathscr{P}_a$ or $\mathscr{P}_v$. Also, the power level in dB is given by

$$(dB) = 10 \log_{10} \frac{\mathscr{P}^{dim}}{\mathscr{P}_{ref}} \tag{4.4.2}$$

where $\mathscr{P}_{ref}$ is the standard reference power of 10^{-12} watts.

Surface Work, $\mathscr{W}_o$

For the theory and experiment, we adopt a load distribution of the form

$$L(x,y) = \frac{2}{\pi A^2}\sqrt{A^2-y^2}\,L(x) \quad |x| < 1 \ , \ |y| < A \tag{4.4.3}$$

Substitute (4.4.3) into (4.1.8) to obtain

$$\mathscr{W}_o = \alpha_o \int_{-1}^{1} (x-x_o)\ \mathrm{Im}\ L(x)dx \tag{4.4.4}$$

For the theoretical load distribution we have (see (3.2.6))

$$L(x) = \alpha_o \sqrt{1-x^2} \sum_{n=1}^{\infty} L_n\, U_{n-1}(x) \tag{4.4.5}$$

so that

$$\mathscr{W}_o = \frac{\pi}{2} \cdot \alpha_o^2 \left(-x_o\ \mathrm{Im}\ L_1 + \frac{1}{2}\ \mathrm{Im}\ L_2\right) \quad \text{Theory} \tag{4.4.6}$$

For the flat edge load of the experiment we assume

$$L(x) = \alpha_o \sum_{n=1}^{\infty} L_n\, P_{n-1}(x) \tag{4.4.7}$$

where $P_n(x)$ is the Legendre polynomial. Thus, we obtain

$$\mathscr{W}_o = 2\alpha_o^2 \left(-x_o\ \mathrm{Im}\ L_1 + \frac{1}{3}\ \mathrm{Im}\ L_2\right) \quad \text{Experiment} \tag{4.4.8}$$

where L_1 and L_2 are to be evaluated from the experimental load distribution; i.e.,

$$\mathrm{Im}L_n = \left(n - \frac{1}{2}\right)\int_{-1}^{1} x^{n-1}dx \int_{-A}^{A} dy \, \frac{L_{exp}(x,y)}{\alpha_o} \qquad n=1,2 \qquad (4.4.9)$$

Radiated Acoustic Energy, $\mathscr{P}_a$

With (4.1.9) and the fact that in the far field

$$V_r \approx k\, H_f \qquad (4.4.10)$$

we obtain

$$\mathscr{P}_a = k\int_{|\vec{x}|=r_o} d\Omega \; r_o^2 \; |H_f|^2 \qquad (4.4.11)$$

and with (3.2.4) and (3.2.5) of Section 3 we get

$$|H_f| = \frac{k}{4\pi} \cdot \frac{z}{r^2} \, |S| \qquad (4.4.12)$$

where

$$S = \iint d^2\vec{\xi} \; e^{ik\hat{y}\cdot\vec{\xi}} \qquad (4.4.13)$$

Introduce spherical coordinates

$$(x,y,z) = r(\cos\psi\cos\phi, \; \cos\psi\sin\phi, \; \sin\psi) \qquad (4.4.14)$$

and evaluate

$$S = \frac{2\alpha_o}{\pi A^2} \int_{-A}^{A} d\eta \, \sqrt{A^2-\eta^2} \; e^{ik\cdot\eta\cos\psi\sin\phi}$$

$$\cdot \sum_{n=1}^{\infty} L_n \cdot \int_{-1}^{1} d\xi \, \sqrt{1-\xi^2} \; U_{n-1}(\xi) \; e^{ik\cdot\xi\cos\psi\cos\phi}$$

$$= \frac{2\pi\alpha_o}{i} \frac{J_1(\lambda)}{\lambda} \cdot Q \qquad (4.4.15)$$

where

$$Q = \sum_{n=1}^{\infty} L_n \cdot n \cdot i^n \frac{J_n(\beta)}{\beta} \tag{4.4.16}$$

with

$$\lambda = kA \cos\psi \sin\phi$$

$$\beta = k \cos\psi \cos\phi \tag{4.4.17}$$

The final formula for the sound power is

$$\mathscr{P}_a = \alpha_o^2 \cdot k^3 \int_0^{\pi} d\phi \int_0^{\pi/2} \cos\psi \sin^2\psi d\psi \left[\frac{J_1(\lambda)}{\lambda}\right]^2 |Q|^2 \tag{4.4.18}$$

Note that the sound power depends on all of the load coefficients (see (4.4.16)) in contrast to the surface work.

Dissipated Vortical Energy, $\mathscr{P}_v$

We turn now to the calculation of the energy that is dissipated in the form of vorticity. From (4.1.10), and the Parseval relation

$$\oint dxdy\ |Q|^2 = \frac{1}{(2\pi)^2} \oint d\alpha d\beta\ |Q^+|^2 \tag{4.4.19}$$

we obtain

$$\mathscr{P}_v = \frac{1}{(2\pi)^2 o^2} \int_{-\infty}^{\infty} dz \oint d\alpha d\beta \left(|\Omega_x^+|^2 + |\Omega_y^+|^2\right) \tag{4.4.20}$$

From (4.2.10) and (4.2.11) we have further

$$|\Omega_x^+|^2 + |\Omega_y^+|^2 = \frac{o^4(\alpha^2+\beta^2)|L^+|^2}{4|\lambda_o|^2} e^{-2Re\lambda_o|z|} \tag{4.4.21}$$

so that the integration over z can be carried out in (4.4.20) to obtain

$$\mathscr{P}_v = \frac{\sigma^2}{4(2\pi)^2} \oint_{\sigma} d\alpha d\beta \, \frac{(\alpha^2+\beta^2)|L^+|^2}{|\lambda_o|^2 \mathrm{Re}\lambda_o} \tag{4.4.22}$$

To evaluate (4.4.22) we adopt the following generalization of the surface load distribution with which we can simulate the theoretical or experimental results:

$$L(x,y) = \frac{2\alpha_o}{\pi A^2} \sqrt{A^2-y^2} \, (1+x)^{\nu} \, (1-x)^{\varepsilon} \, P(x) \tag{4.4.23}$$

where $P(x)$ is a polynomial and ε, ν are to be determined by an appropriate limit process at the leading and trailing edges (see Section 4.3 for details). The asymptotic evaluation of (4.4.22) is a tedious step that we outline in Appendix E. The final result is, for $\varepsilon = \nu$

$$\mathscr{P}_v = \frac{4^{\varepsilon}(\Gamma(1+\varepsilon))^2}{\sigma^{2\varepsilon}} \left(\frac{2\sqrt{2}\,\alpha_o^2}{3\pi^3 A} \right) \cdot \quad \varepsilon(\sigma s)(|P(-1)|^2 + |P(1)|^2) \tag{4.4.24}$$

where

$$\mathscr{I}_{\varepsilon}(\delta) = \int_{-\infty}^{\infty} \frac{du}{|u|^{2\varepsilon}\left[u^4+(1+\delta u)^2\right]^{1/2}\left\{u^2+\left[u^4+(1+\delta u)^2\right]^{1/2}\right\}^{1/2}} \tag{4.4.25}$$

For any $0 < \varepsilon < 1/2$, the dissipation is of order $1/\sigma^{2\varepsilon}$ and tends to zero with increasing Stokes number. We can compare this with the results of Section 4.3 where we found that the shed vorticity also has a similar behavior. The interesting fact is that the dissipation is practically independent of Stokes number for the flat edge load; i.e.,

For $\varepsilon = 0$

$$\mathscr{P}_v = \frac{2\sqrt{2}}{3\pi^3 A} \cdot \alpha_o^2 \cdot (|P(-1)|^2 + |P(1)|^2) \cdot \mathscr{I}_o(\sigma s) \tag{4.4.26}$$

where

$$\mathscr{J}_0(\delta) = \int_{-\infty}^{\infty} \frac{du}{\left[u^4(1+\delta u)^2\right]^{1/2}\left\{u^2+\left[u^4+(u^4(1+\delta u)^2\right]^{1/2}\right\}^{1/2}} \qquad (4.4.27)$$

The function $\mathscr{J}_0(\delta)$ is plotted in Fig. 4.4-1. We see that the dependence on δ is relatively weak; $2 \leq \mathscr{J}_0 \leq 4.5$ over the full range of δ. Thus, the total dissipation is primarily a function of the edge loads and is proportional to α_0^2.

In Table 4.1, we give the energy budget for the Brooks experiment. The total acoustic sound power is estimated with (4.4.18) with α_0 chosen to give the experimental sound pressure levels in the far field (see Figs. A.4, A.5, Appendix A).

Table 4.1 Energy Budget for the Brooks Experiment

k	α_0 (μrad)	$\mathscr{P}_a$ (dB)	$\mathscr{P}_v$ (dB)	$\mathscr{W}_0$	$\mathscr{P}_a + \mathscr{P}_v$	Δ dB
1.255	82.1	86.9	94.9	91.9	95.5	3.6
1.255	259.3	98.9	106.8	103.9	107.6	3.7
1.989	30.8	91.2	94.4	94.2	96.1	1.9
1.989	97.6	101.2	104.4	104.2	106.1	1.9

The total surface work is estimated indirectly with the inviscid acoustic calculation. The surface work is equal to the sound power radiated when the inviscid formula is used. Thus, we use (4.4.18) with α_0 chosen to give the far field sound pressure levels calculated by Brooks (see Figs. A.4, A.5, Appendix A). The viscous dissipation is estimated with (4.4.26) where the value of $\mathscr{J}_0$ corresponding to the no flow condition is used, i.e., $\mathscr{J}_0 = 2.2$, see Fig. 4.4-1. The difference between the surface work and the sum of the sound power and dissipation is 3.6 dB for $k = 1.255$ and 2 dB for $k = 1.989$. These results are in qualitative agreement with our initial estimate of the energy partitioning in Ref. 2. As a matter of interest, we also show in Fig. 4.4-2 the results for the surface work and sound power of a completely inviscid calculation over the Helmholtz number range from $0.3 < k < 4.0$ at a constant amplitude of 30.8 μradians. The energy is conserved (maximum error ≈ 2 dB) and grows monotonically with increasing k. These results provide an indirect check on the spectral method of calculation used in Section 3.

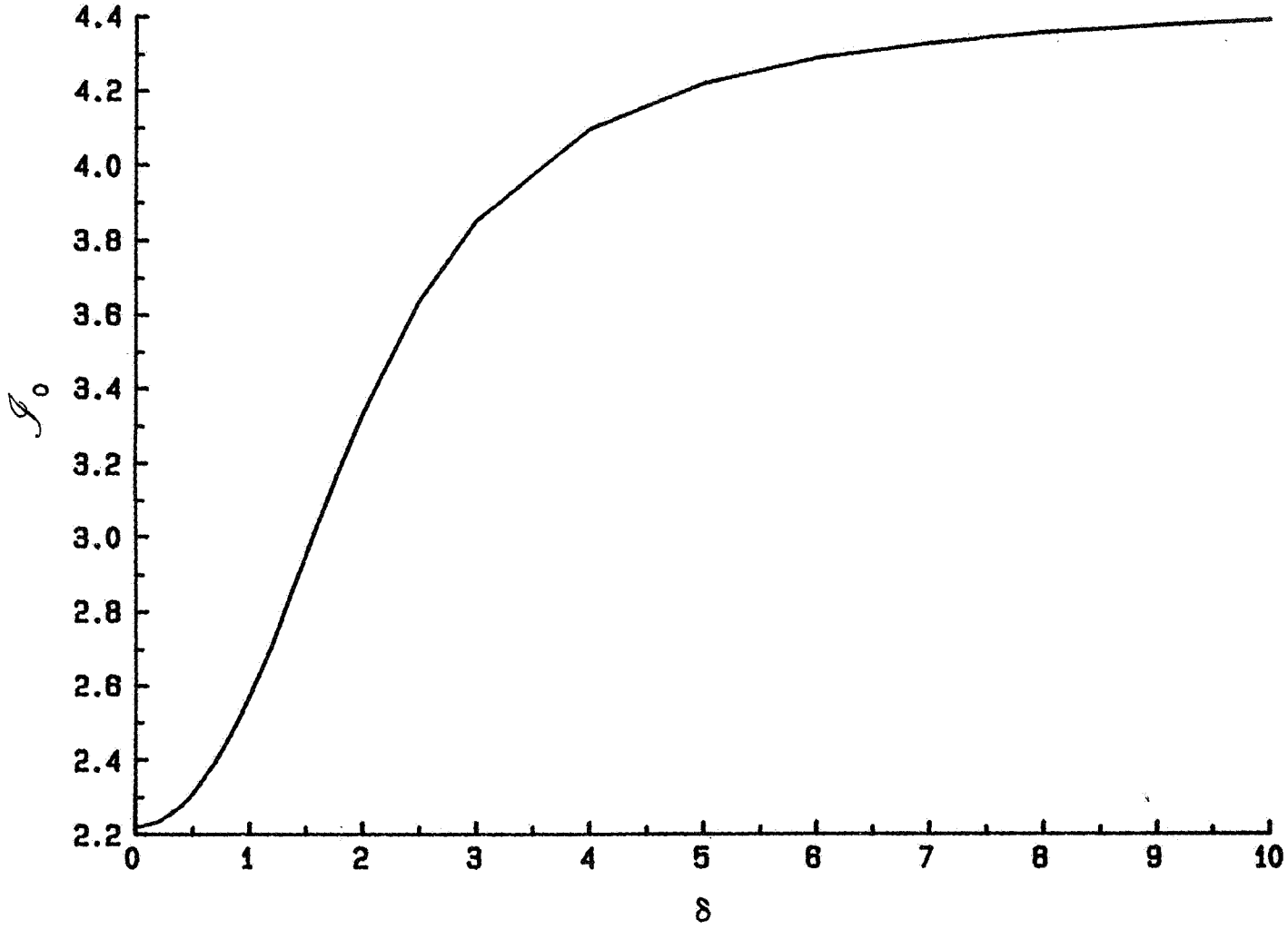

Figure 4.4-1 - Dissipation Integral (see (4.4.27) as a Function of the Dimensionless Streaming Velocity.

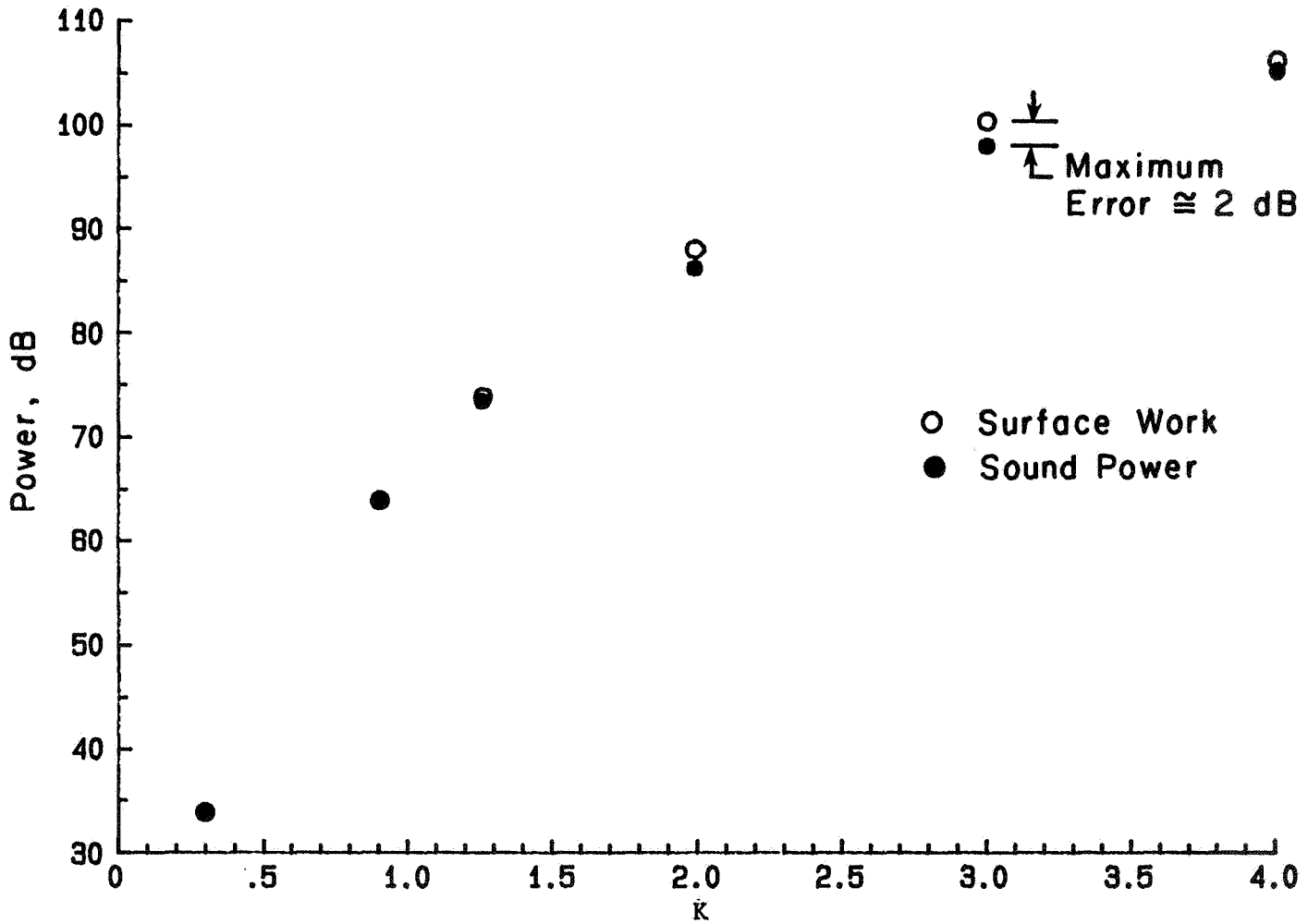

Figure 4.4-2 - Surface Work and Sound Power Versus Helmholtz Number k for the Inviscid Calculation; α_o=30.8 μ rad.

In conclusion, we reiterate the fact that even though the viscous energy estimates can be used to argue the internal consistency of the surface and far field data of Brooks, all attempts to directly calculate the surface load have led to the conclusion that a flat edge loading is not possible.

5. CONCLUSIONS AND RECOMMENDATIONS

A comprehensive analytical study of the Brooks experiment with a vibrating airfoil has been completed. The analysis is based on linearized theory. The effectsof viscosity, compressibility, and finite thickness of the vibrating surface have been investigated. The conclusions of our study are summarized below.

5.1 Three-Dimensional Inviscid Theory with Prescribed Neumann Edge Conditions

1. With he modified aspect ratio A*, the calculated acoustic far field pressure amplitudes are within 1 or 2 dB of the experimental measurements. With the geometric aspect ratio the differences are 4to 5 dB.

2. The calculated phase of the far field pressure is generally within 10 to 15 degrees of the experimental value.

3. The calculated peak surface pressure amplitudes are under-predicted by 3 to 7 dB, with or without the suggested aspect ratio corrections. The calculated pressure decays elliptically near the leading and trailing edges in accordance with the prescribed Neumann condition. The experimental pressure distributions are nearly flat near the edges.

4. The calculated phase of the surface pressure is within 5 to 15 degrees of the measured value. Also, the surface pressure is nearly in phase with the local surface cceleration over the entire chord.

5. Inviscid theory with prescribed Neumann edge conditions cannot predict the measured chordwise surface pressure distribution either in magnitude or in functional form. The theory can predict the form and phase of the far field sound pressure, but the amplitude is somewhat sensitive to the choice of spanwise surface pressure mode shape. With a suggested aspect ratio correction, the far field amplitude can be predicted with 1 or 2 dB.

5.2 Viscous Theory

1. An energy theorem is derived that balances the work done by the vibrating surface against the energy converted into vorticity and sound.

2. With the flat edge loading and Helmholtz numbers of the Brooks experiment the energy is nearly equally partitioned into sound and vorticity. With the elliptically loaded edge nearly all of the surface work is converted into sound.

3. A postulated small streaming velocity does not alter the last conclusion. However, the vorticity produced is convected downstream while it decays.

4. All of the viscous load calculations with or without finite airfoil thickness have led to the same conclusion. For all Stokes numbers ($\sigma = c/2\sqrt{\omega/\nu}$) greater than approximately 100 the calculated viscous load distribution decays elliptically and agrees with the inviscid elliptic distribution near the edges.

5. If the viscous theory is correct, then for Stokes numbers σ of order 3000, as in the Brooks experiment, the inviscid theory with prescribed Neumann edge conditions is completely adequate to predict the outcome of a surface vibration experiment.

Alternative

Either the viscous theory is inadequate to predict the measured surface load distribution or there is a source of error in the measured surface load that has not been detected.

5.3 Possible Sources of Experimental Error

1. The effect of contaminating the inviscid surface pressure calculations with acceleration was considered. The effect of acceleration is to increase the magnitude of the surface pressure with very little change in the phase. Also, the pressure peaks calculated with inviscid theory are shifted closer to the edges and the edge load distribution becomes more flat. However, to account for the 3 to 7 dB differences between the measured and calculated surface pressure amplitude, an acceleration sensitivity of approximately 1 Pascal per g would be necessary. Based on the calibration studies of Brooks where the question of acceleration contamination was carefully considered, a sensitivity of this magnitude is not believed to be possible.

2. A basic assumption in the experiment is that the pressure is 180 degrees out of phase on opposite sides of the airfoil and that the vibration mode shape is a pure torsional oscillation. The effect of violating these conditions was investigated. The effect of adding in a component of in-plane vibration was calculated. The surface pressure amplitude is increased and the distribution becomes flatter near the edges. The pressure on opposite sides of the airfoil due to the in-plane mode of vibration is in phase. The far field sound pressure field is affected but to a lesser degree than the near field. To account for the 3 to 7 dB difference between the calculated and experimental surface pressures, an in phase vibration amplitude of the order of the trailing edge displacement due to torsional vibration would be necessary.

Recommendations

1. It is recommended that the experiment be partially repeated with the following changes:

   a. Mount additional accelerometers on the vibrating airfoil to ascertain the precise vibration mode shape. In particular, determine whether a component of in-plane vibration is present.

   b. Measure the surface pressure on both sides of the airfoil near the leading and trailing edges.

   c. Reexamine the acceleration sensitivity of the surface pressure transducers.

2. To support the experimental measurements, it is also recommended that a vibration analysis be completed to calculate the frequencies of the in-plane bending vibration mode and the torsion mode. If these two frequencies are close together, it can be expected that any misalignment of the torsion shafts would lead to a coupled bending torsion vibration mode shape even though an attempt is made to excite only one mode.

3. Finally, it is recommended that the inviscid surface and far field calculations be repeated with more assumed spanwise pressure modes. The ambiguity associated with the choice of aspect ratio in Section 3.4 can then be resolved.

APPENDIX A
BRIEF DESCRIPTION OF THE BROOKS EXPERIMENT AND SUMMARY OF RELEVANT DATA

The Brooks experiment (Ref. 1) was designed to check the validity of the inviscid Kirchhoff integral relation

$$p'(\vec{x}) = \frac{1}{4\pi} \iint_S dS \left[p'(\vec{y}) \frac{\partial}{\partial n} \frac{e^{-ik|\vec{x}-\vec{y}|}}{|\vec{x}-\vec{y}|} + i\omega\rho v_n'(\vec{y}) \frac{e^{ik|\vec{x}-\vec{y}|}}{|\vec{x}-\vec{y}|} \right] \quad (A.1)$$

where $p'(\vec{y})$ and $v_n'(\vec{y})$ denote pressure and velocity (complex amplitude) on a vibrating surface S and $p'(\vec{x})$ is the pressure in the free field. A segment of a NACA 0012 airfoil was oscillated in an anechoic chamber at frequencies of 301 and 477 Hz (see Fig. A.1). The surface pressure and velocity and the far field acoustic pressure were measured simultaneously. The far field was also calculated with (A.1) using the measured surface quantities. The main results of the measurement and calculation are summarized in Figs. A.2, through A.5. The data required to perform the calculations in the present report are summarized below:

Geometry (See Fig. A.1)

AIRFOIL TYPE	NACA 0012
Chord (c)	1.5 ft
Span (b)	1.0 ft
Aspect Ratio (A)	0.666
Axis of Rotation	7.5 in. aft of the leading edge
Location of Transducer Array	1.25 in. outboard of center span
Radius of Microphone Array from Center of Rotation ($\|\vec{y}\|$)	7.25 ft

Atmospheric Data

Pressure (p)	1.013×10^5 Pa (1 Pa $\doteq 10$ dynes/cm^2)
Sound Speed (a)	1130 ft/sec

Ratio of Specific Heats (γ) 1.4

Kinematic Viscosity (ν) 1.6×10^{-4} ft^2/sec (68^oF)

In addition to the above data, we summarize in Tables A.1 and A.2 the frequency data and some information on peak amplitudes and trailing edge conditions. The data in Table A.3 are from Ref. 1.

TABLE A.1 Frequency Dependent Parameters

Frequency Hz (Rad/sec)	Helmholtz Number $k = \omega c/4a$	Stokes Number $\sigma = \frac{c}{2}\sqrt{\frac{\omega}{\nu}}$	Streaming Velocity $\sqrt{\omega\nu}$ (ft/sec)
301 (1981)	1.255	2578	0.55
477 (2997)	1.989	3236	0.69

TABLE A.2 Amplitude Data

Frequency (Hz)	Peak Angle of Rotation α_o (μrad)	Trailing Edge Peak Values		
		Deflection(ε) (in x 10^3)	Velocity($\dot{\varepsilon}$) ft/sec ($\dot{\varepsilon}/\sqrt{\omega\nu}$)	Acceleration($\ddot{\varepsilon}$) $\ddot{\varepsilon}$/g
301	82.1	0.862	0.136 (.247)	7.99
	259.3	2.72	0.429 (.779)	25.2
477	30.8	0.323	0.0807 (.117)	7.51
	97.6	1.02	0.255 (.369)	23.7

TABLE A.3 - TEST CONDITIONS AND SURFACE PRESSURE RESULTS (see Ref. 1, p. 26)

Transducer number	Transducer location, percent chord	f = 301 Hz; α = 82.1 μrad		f = 301 Hz; α = 259.3 μrad		f = 477 Hz; α = 30.8 μrad		f = 477 Hz; α = 97.6 μrad	
		Peak pressure, $\lvert P_m \rvert$, Pa	Phase, * $\varphi_p - \varphi_a$ deg	Peak pressure, $\lvert P_m \rvert$, Pa	Phase, $\varphi_p - \varphi_a$ deg	Peak pressure, $\lvert P_m \rvert$, Pa	Phase, $\varphi_p - \varphi_a$ deg	Peak pressure, $\lvert P_m \rvert$, Pa	Phase, $\varphi_p - \varphi_a$ deg
1	1.4	5.77	356	24.47	356	7.65	3	22.73	4
2	9.7	5.63	359	21.36	355	6.17	0	19.53	0
3	21.2	5.31	359	21.35	355	6.64	6	20.43	6
4	31.9	1.58	0	7.42	343	3.09	22	9.26	23
5	48.6	2.91	161	11.14	169	3.01	139	9.62	140
6	61.8	6.44	164	26.27	175	7.34	171	23.53	171
7	78.1	9.49	164	37.93	175	11.03	170	34.88	170
8	88.9	10.39	162	40.26	176	11.96	171	38.34	173

* $\phi_p - \phi_a$ is the Phase by Which the Surface Pressure Leads the Normal Surface Acceleration Near Airfoil Leading Edge.

1 Pa=10 dynes/cm (Pascal)

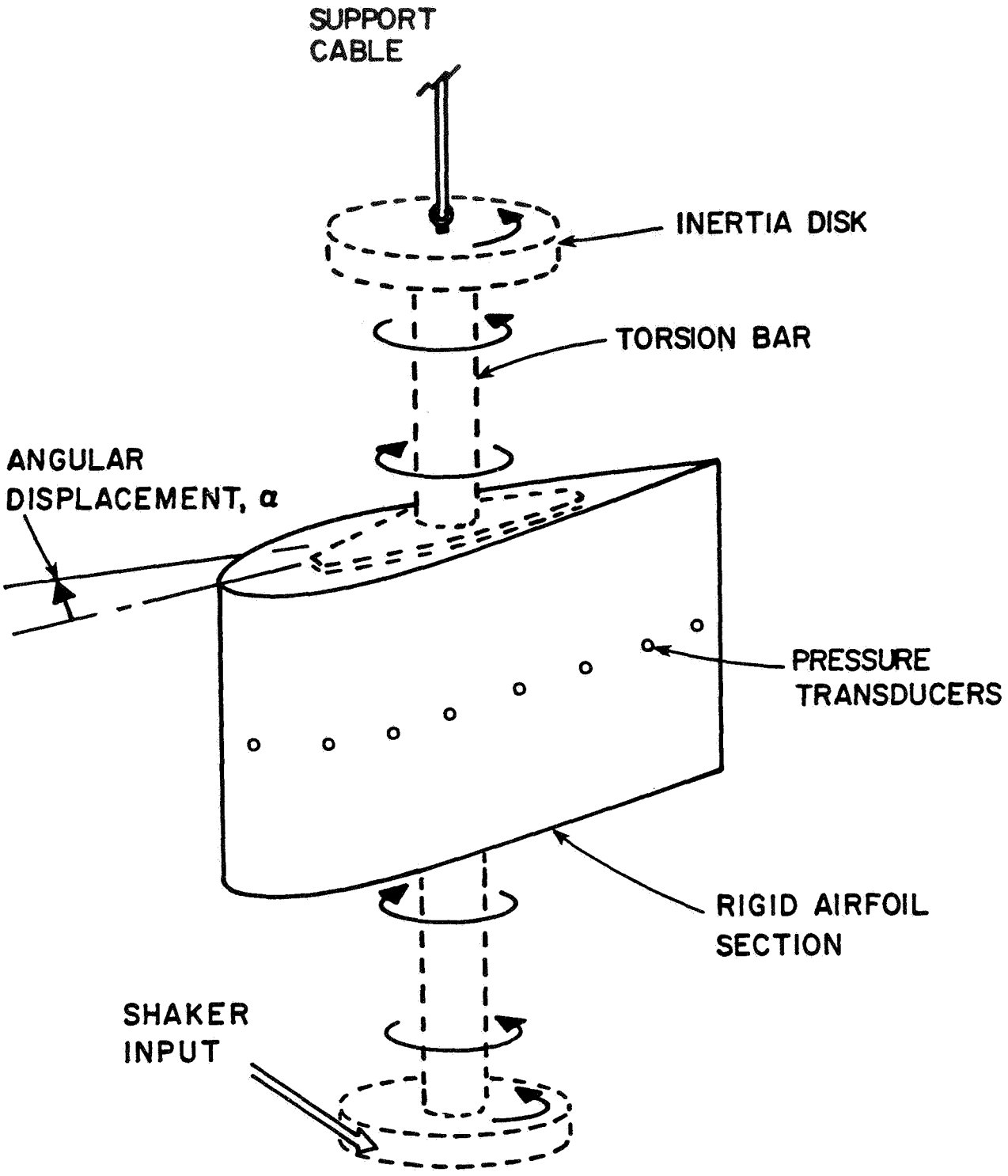

Figure A.1 Experimental Model and Torsional Vibration System.

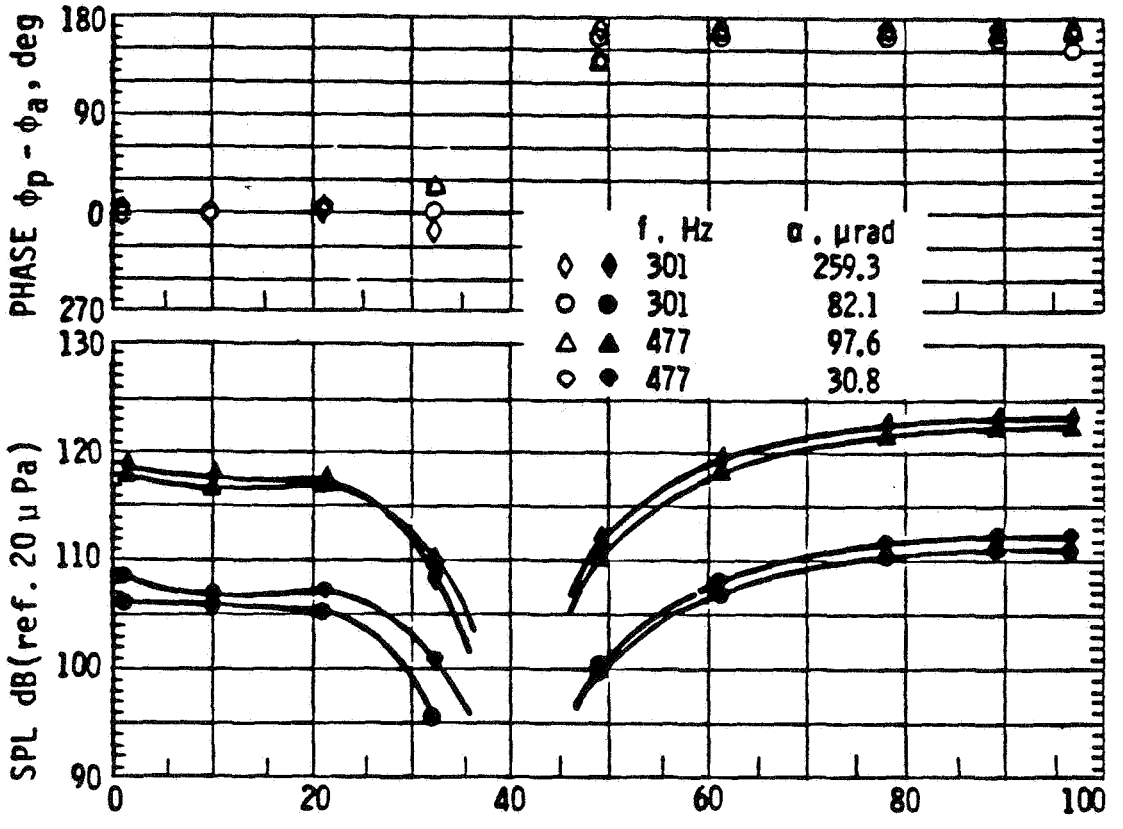

Figure A.2 Surface Pressure Level and Phase as a Function of Transducer Location.

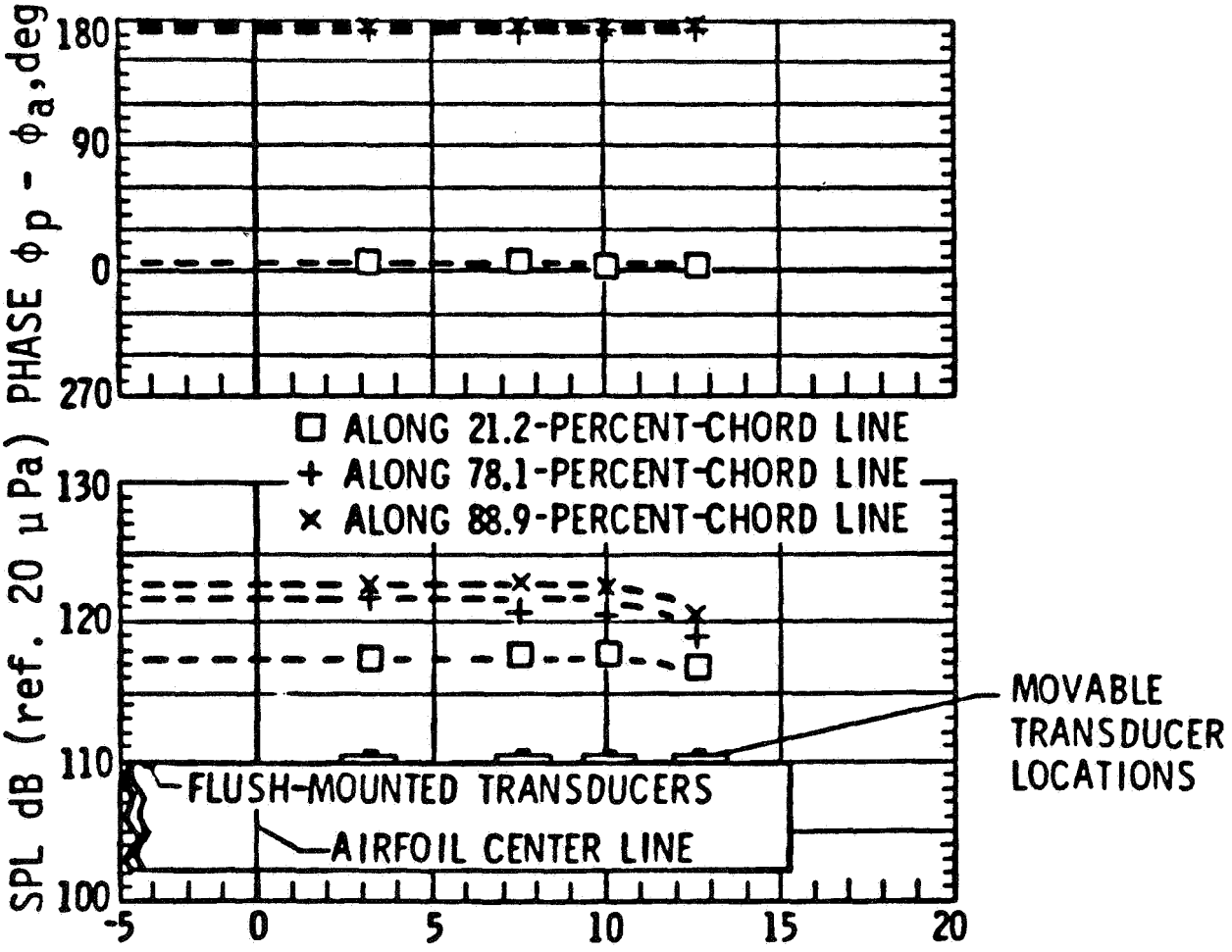

Figure A.3 Results of Spanwise Pressure Survey - Surface Pressure Level and Phase as a Function of Spanwise Location for f=447 Hz.

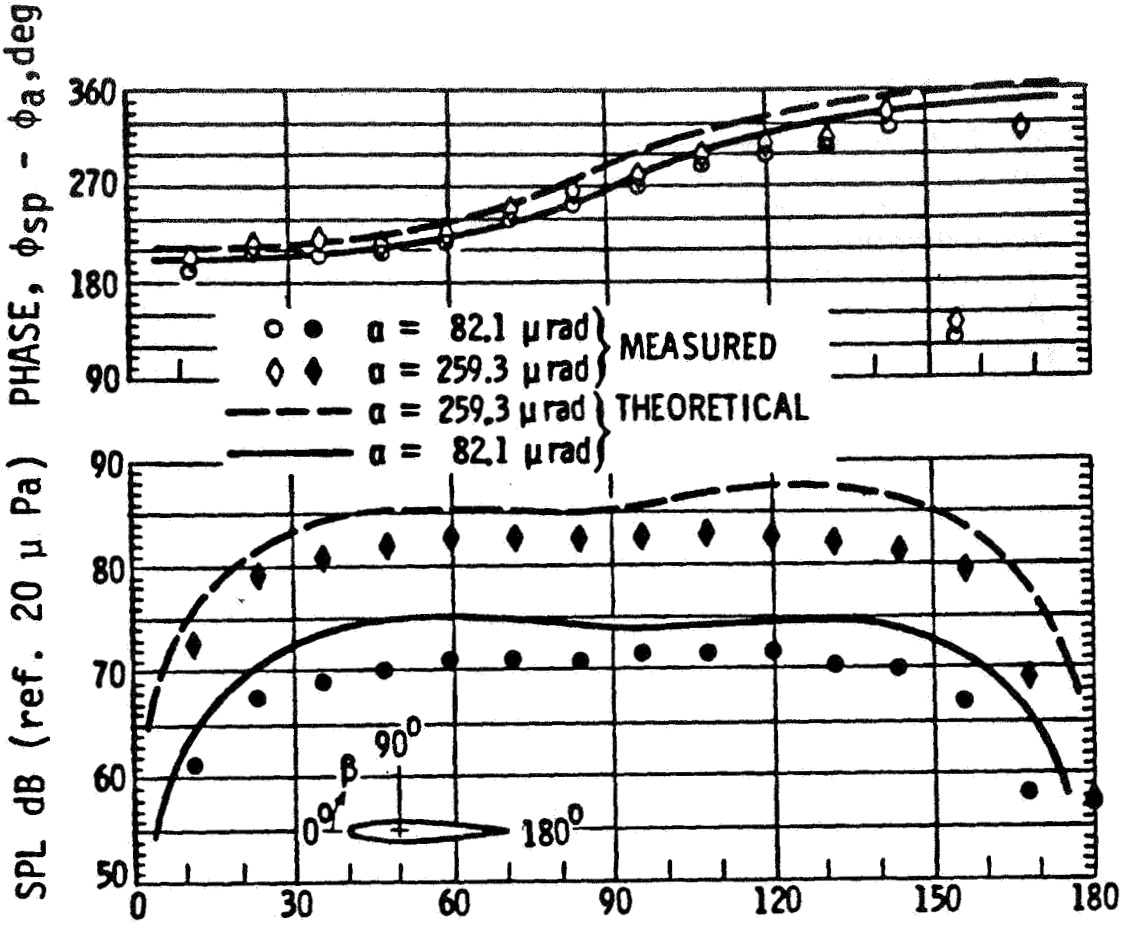

Figure A.4 Sound Pressure Level and Phase as a Function of Directivity Angle β at a Measurement Radius of 2.210 m (7.25) ft) for Airfoil Oscillating at f=301 Hz.

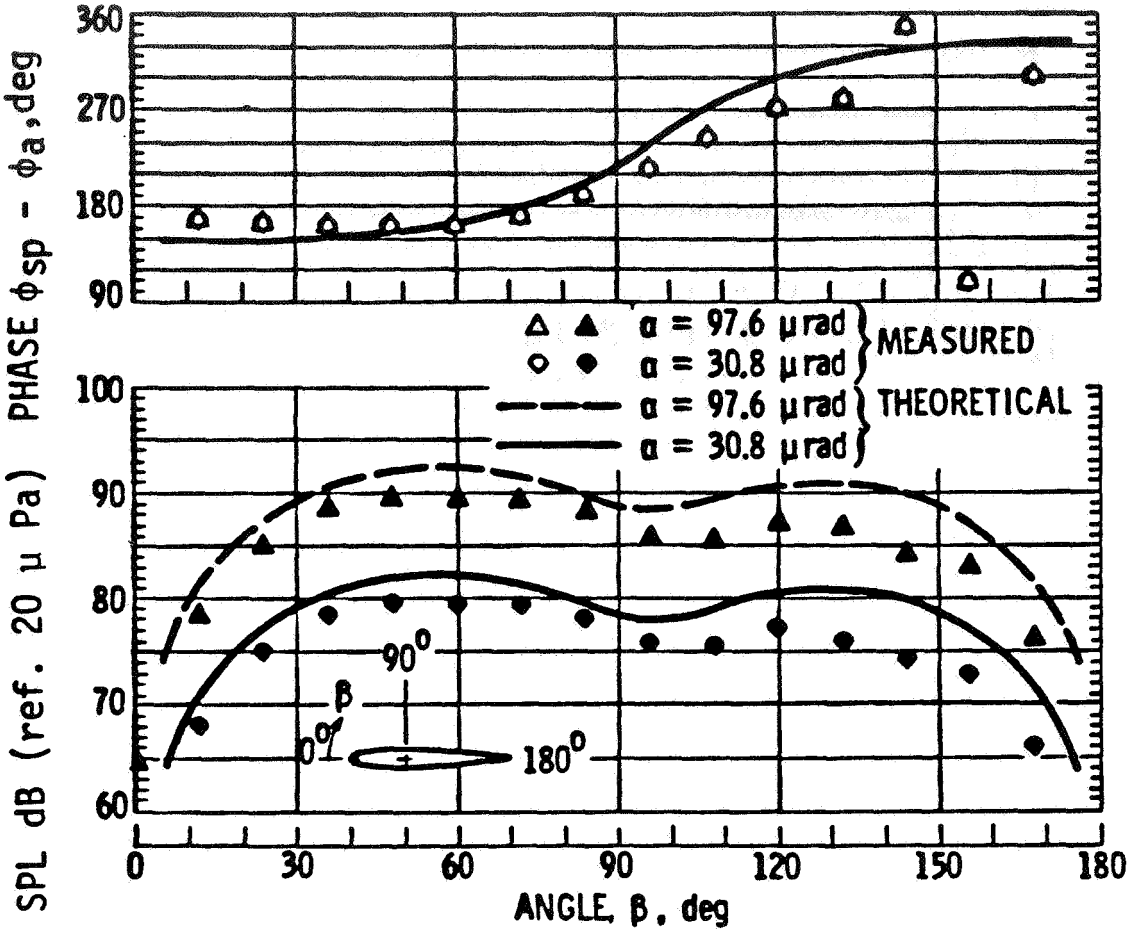

Figure A.5 Sound Pressure Level and Phase as a Function of Directivi Angle β at a Measurement Radius of 2.210 m (7.25 ft) for Airfoil Oscillating, at 477 Hz.

APPENDIX B
COMPARISON OF FLAT PLATE INVISCID THEORY WITH EXPERIMENTAL RESULTS

The theoretical calculations presented in this Appendix (Figs. B.1 through B.4) are based on Eq. (3.2.25) for the surface pressure and phase and on Eq. (3.2.27) for the far field (FF) sound pressure and phase. A complete discussion of these results is given in Section 3.4. The solid curves on each amplitude graph are calculated with the geometric aspect ratio (A = 0.0667). The dashed curve is calculated with the corrected aspect ratio (A* = 0.8) discussed in Section 3.4. The experimental amplitude data of Ref. 1 are denoted by the solid symbols, and the phase data are denoted by open symbols. The Helmholtz number, k, and micro-radian amplitude, α_o, are noted in the title of each graph.

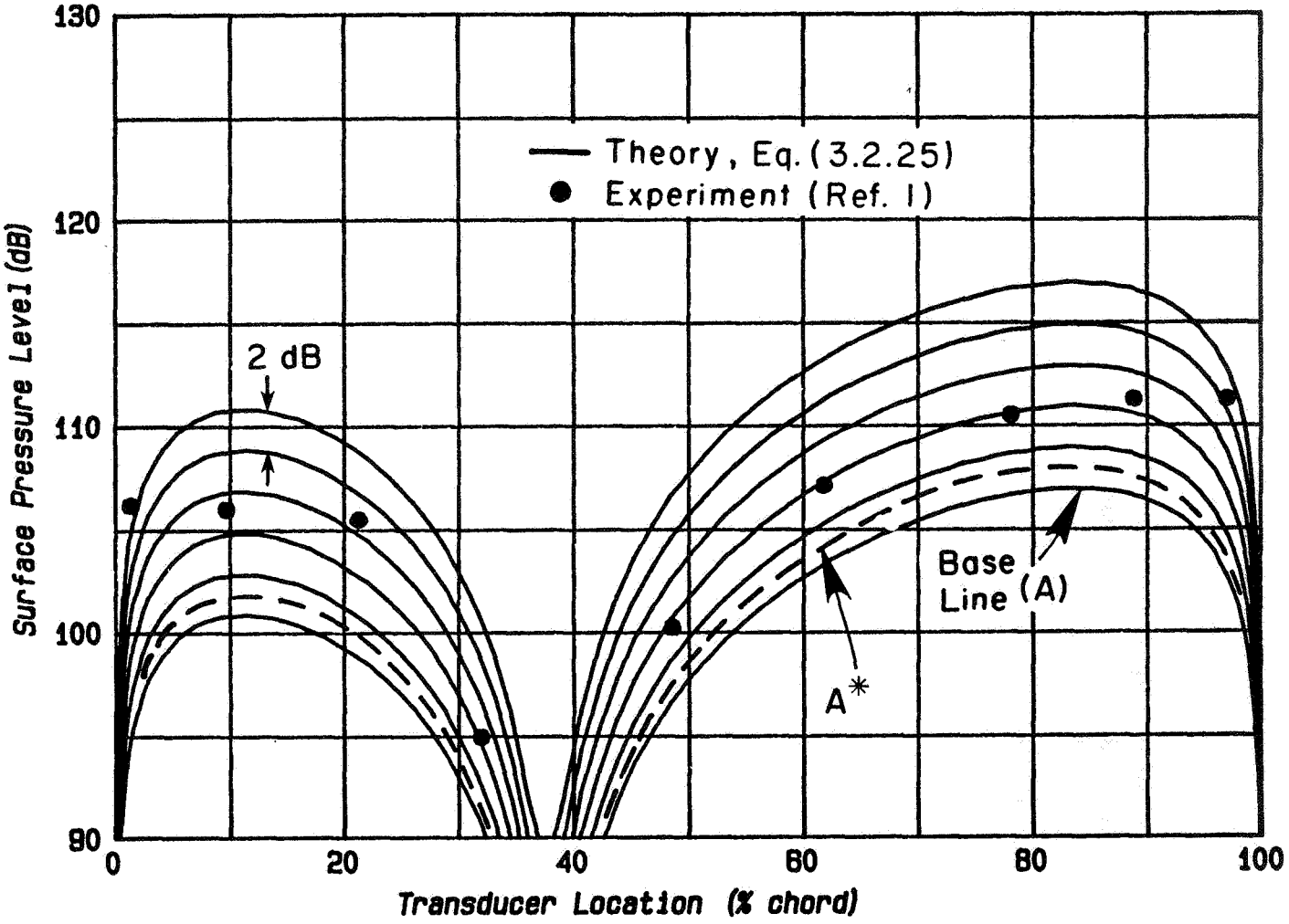

Figure B.1a Comparison of Inviscid Theory and Experiment; k=1.255, α_o=82.1 μrad.

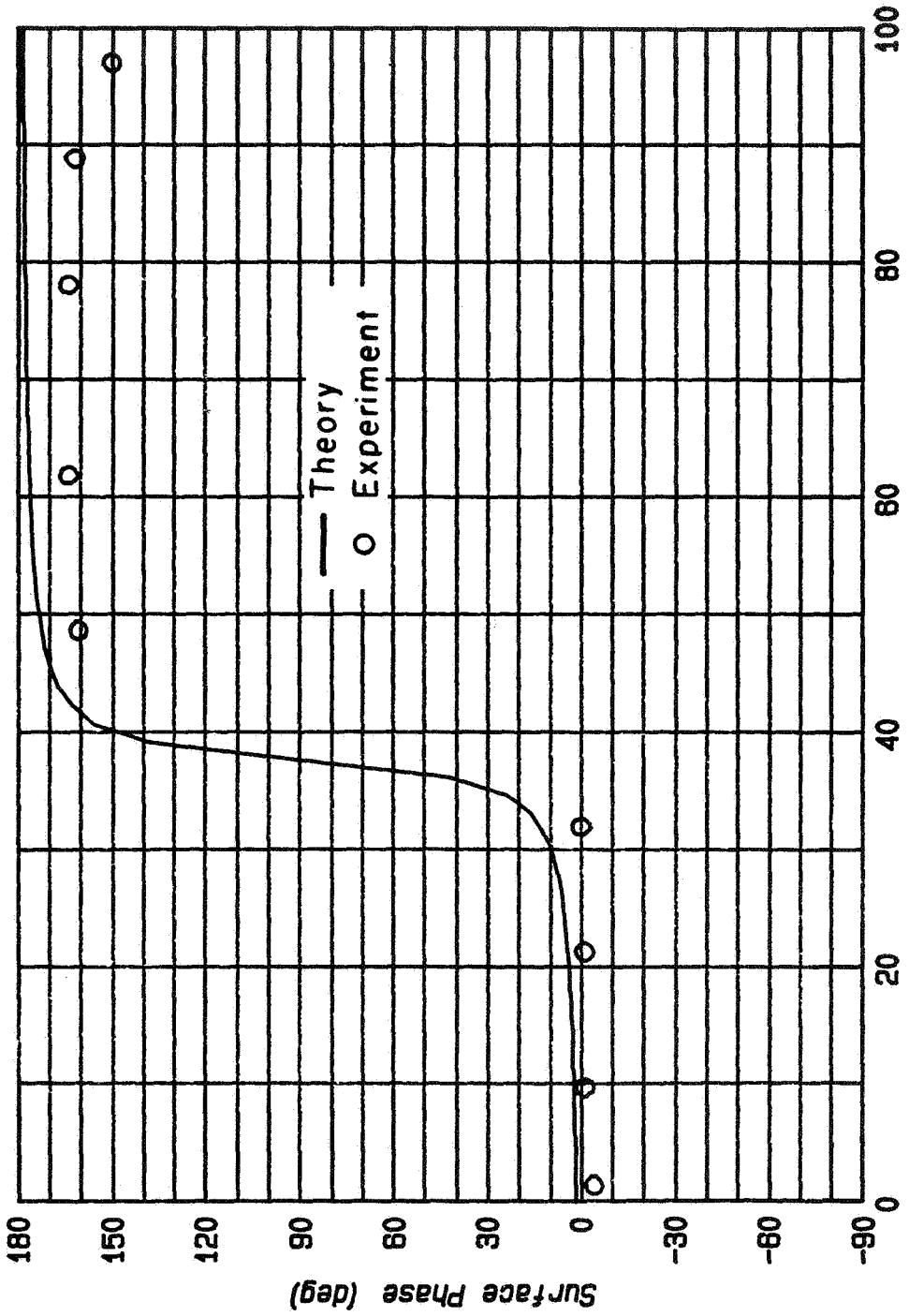

Figure B.1b Comparison of Inviscid Theory and Experiment; k=1.255, α_o=82.1 μrad.

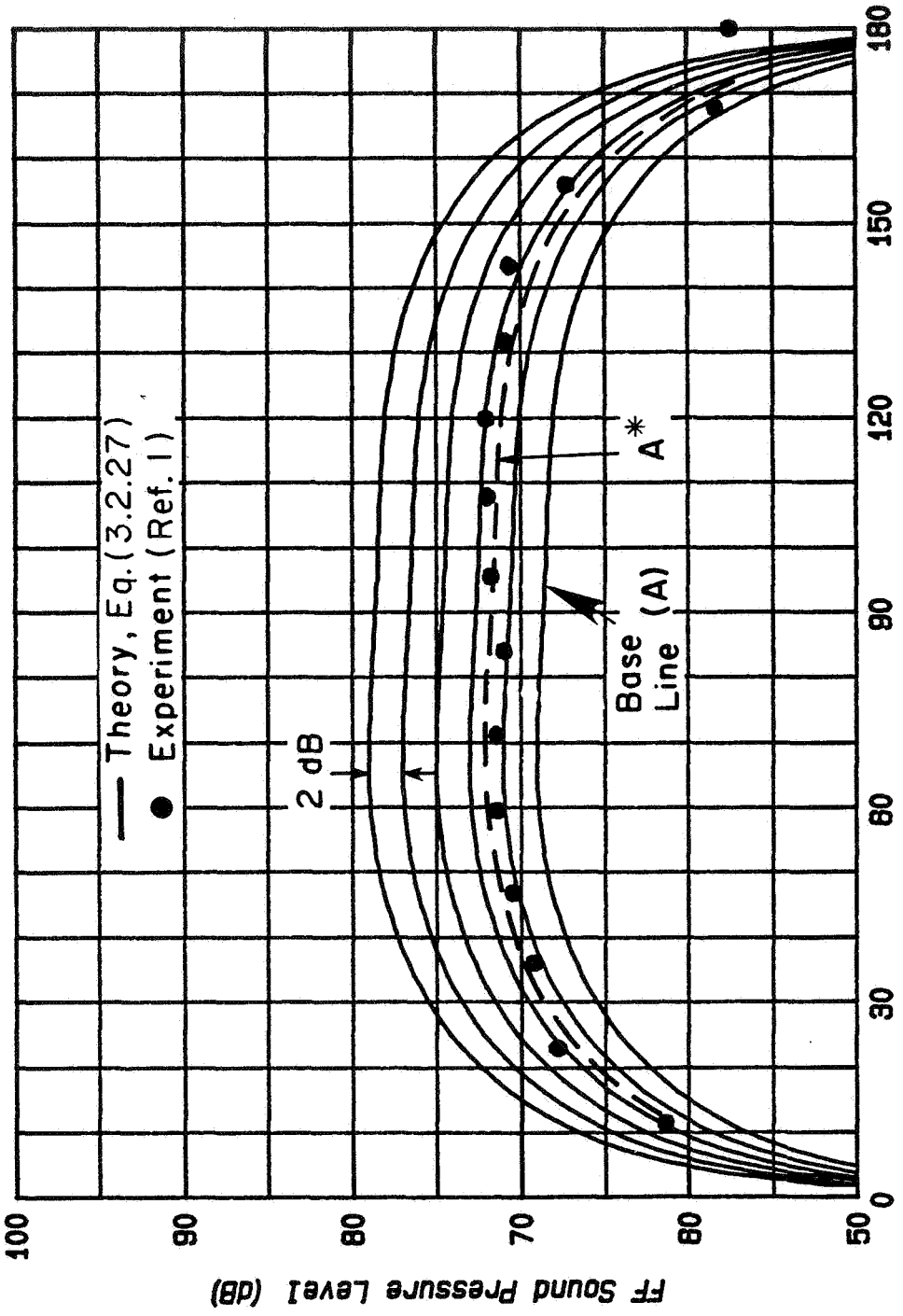

Figure B.1c Comparison of Theory and Experiment; $k=1.255$, $\alpha_o=82.1$ μrad.

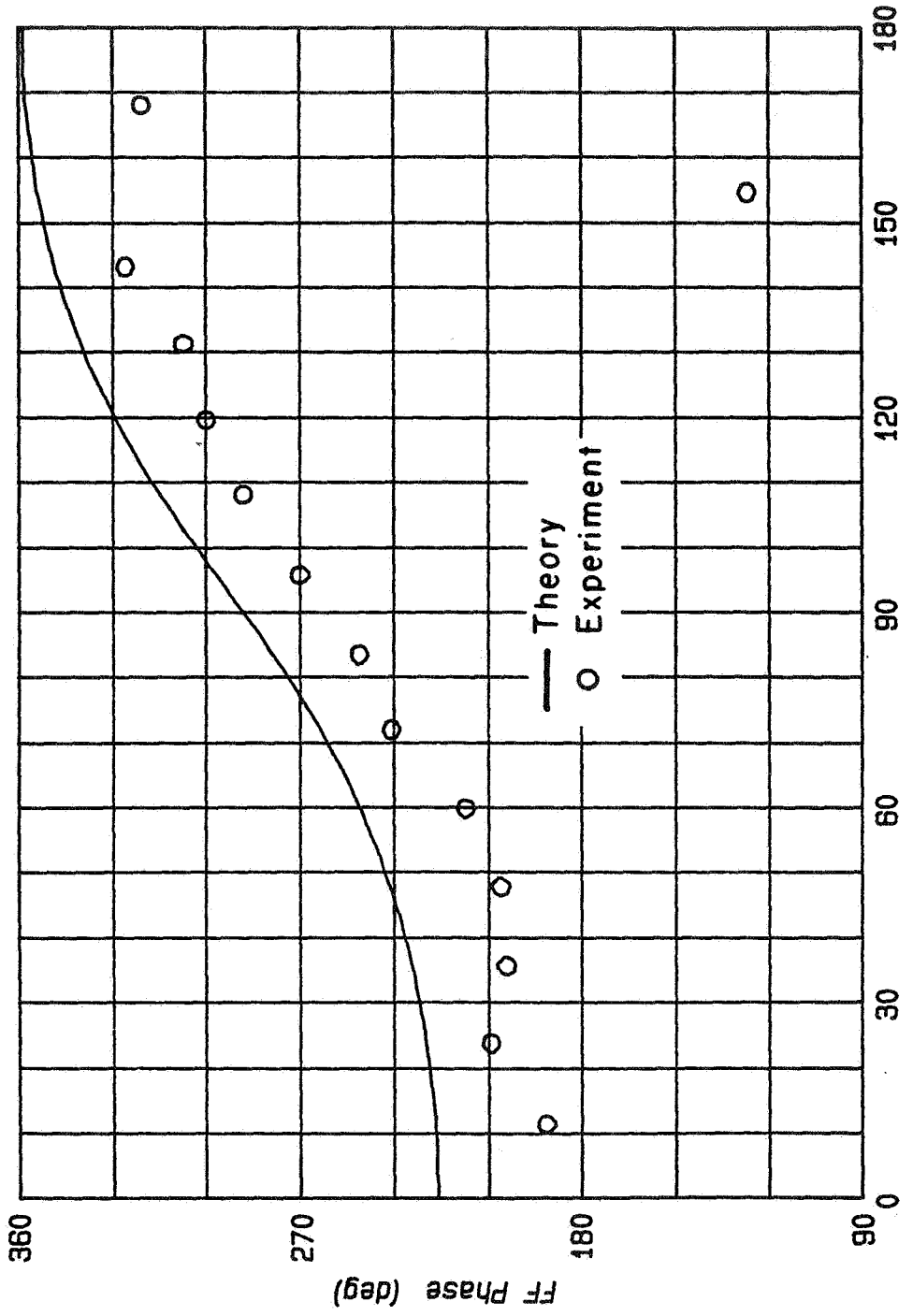

Figure B.1d Comparison of Theory and Experiment; k=1.255, α_o=82.1 μrad.

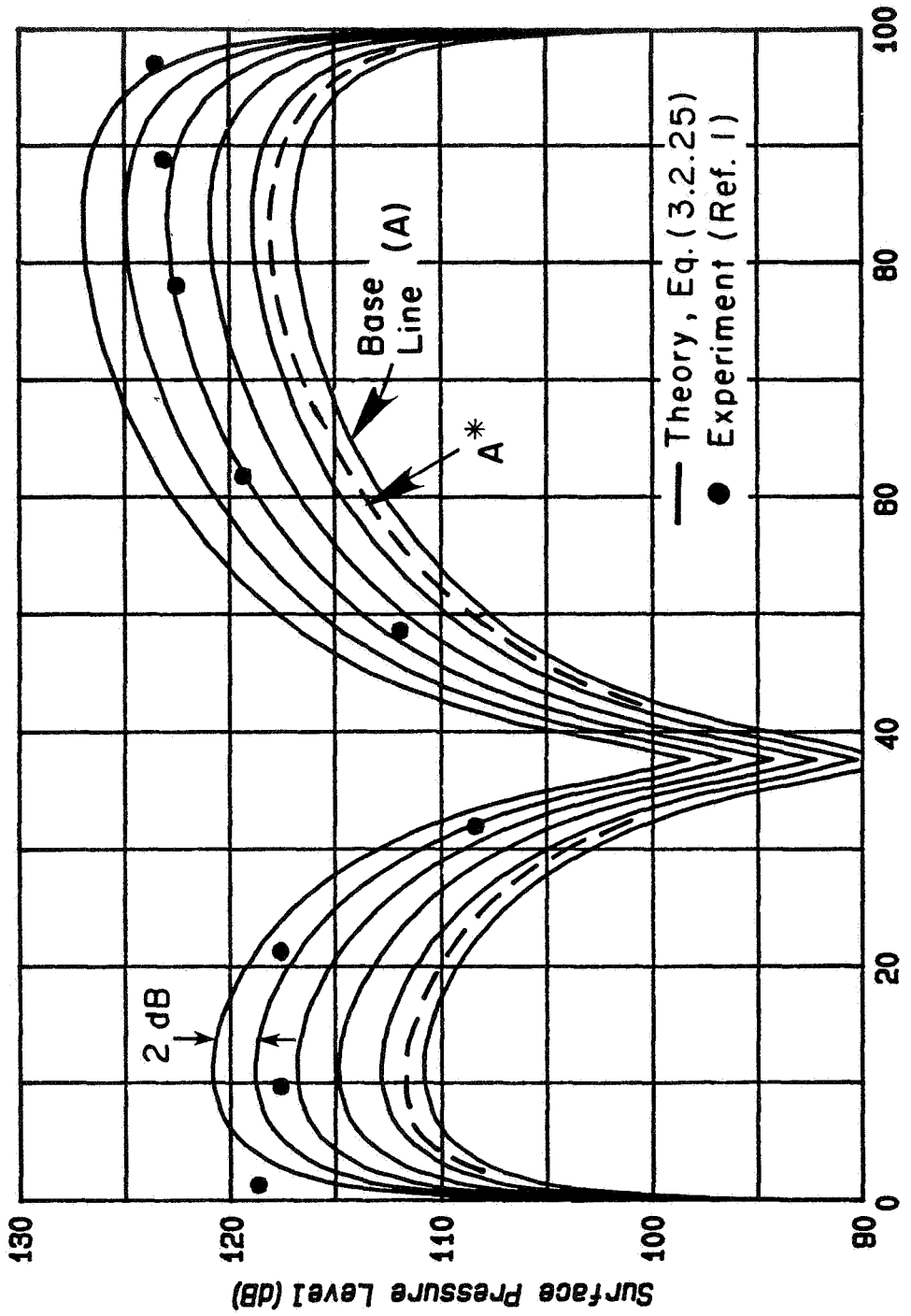

Figure B.2a Comparison of Theory and Experiment; k=1.255, α_o=259.3 μrad.

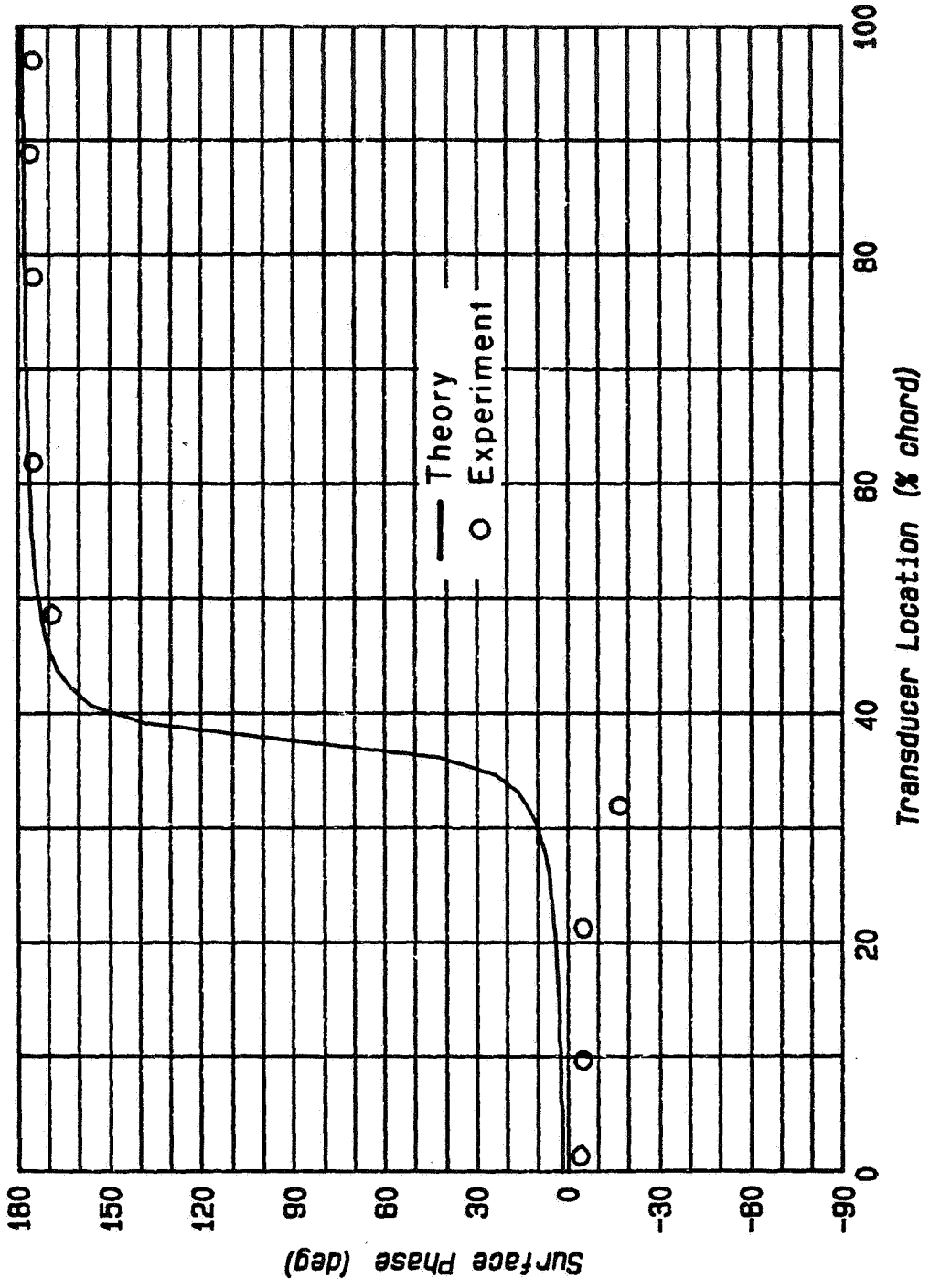

Figure B. 2b Comparison of Theory and Experiment; k=1.255, α_o=259.3 µrad.

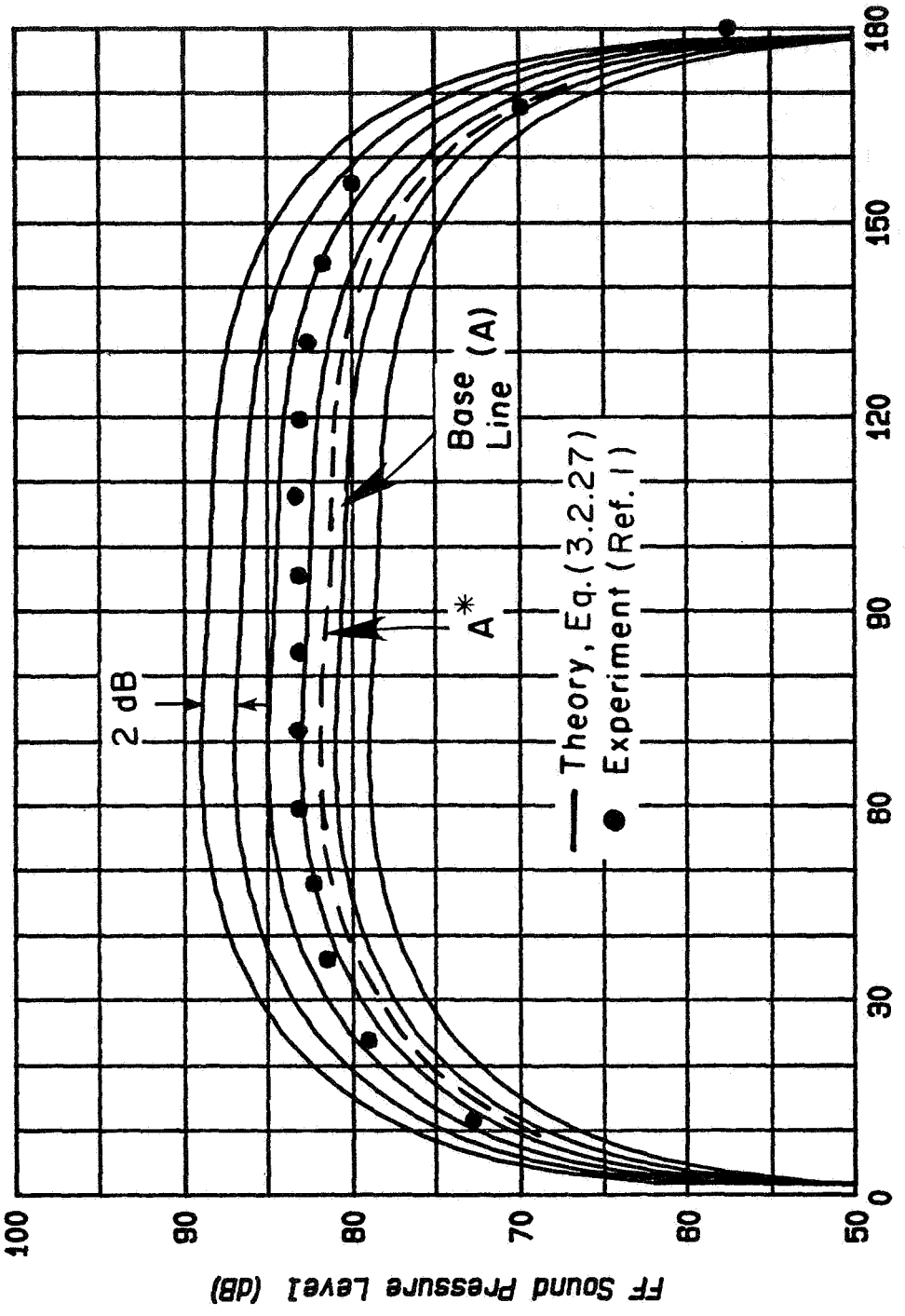

Figure B.2c Comparison of Theory and Experiment; k=1.255, α_o=259.3 μrad.

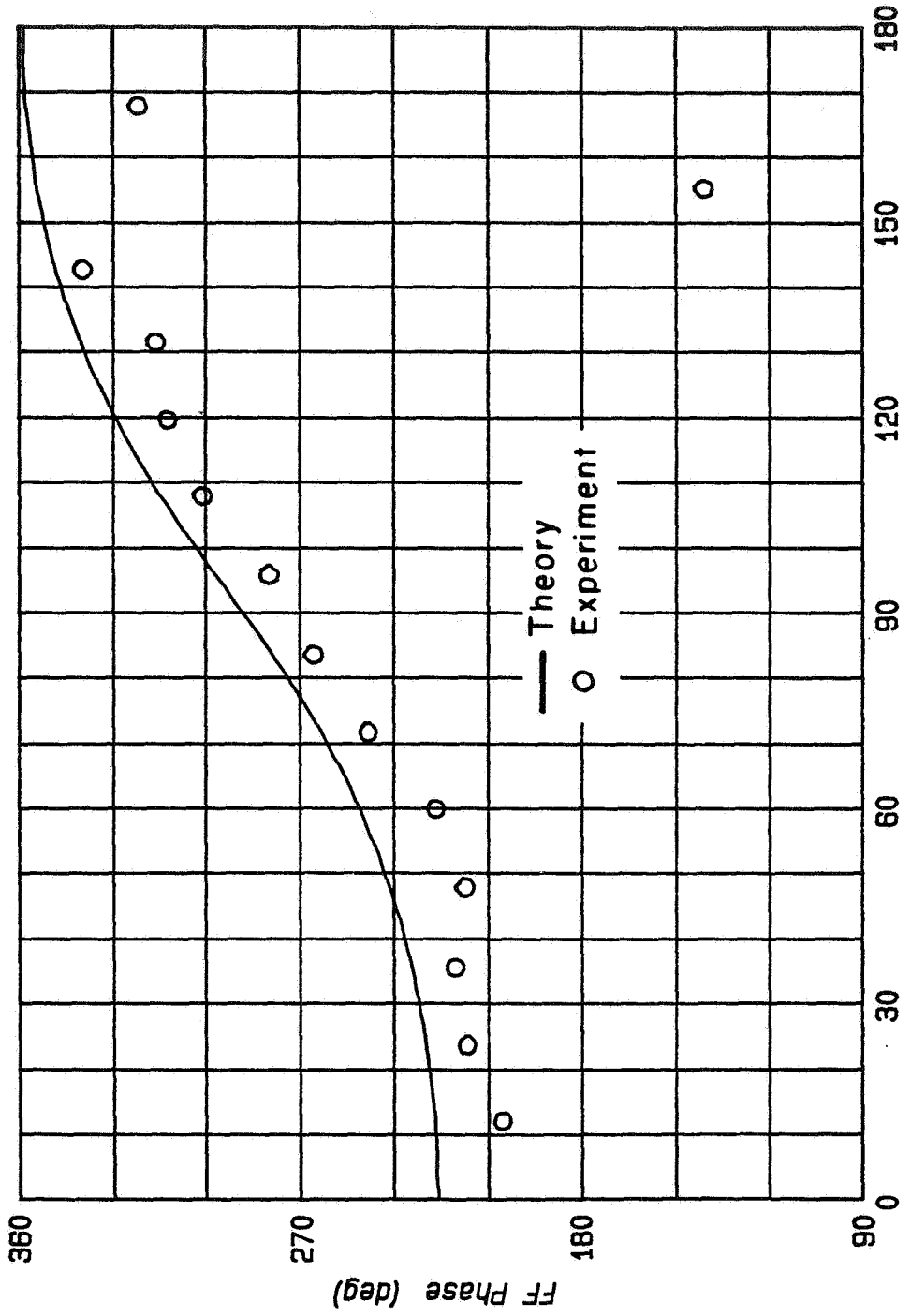

Figure B.2d Comparison of Theory and Experiment; k=1.255, α_o=259.3 μrad.

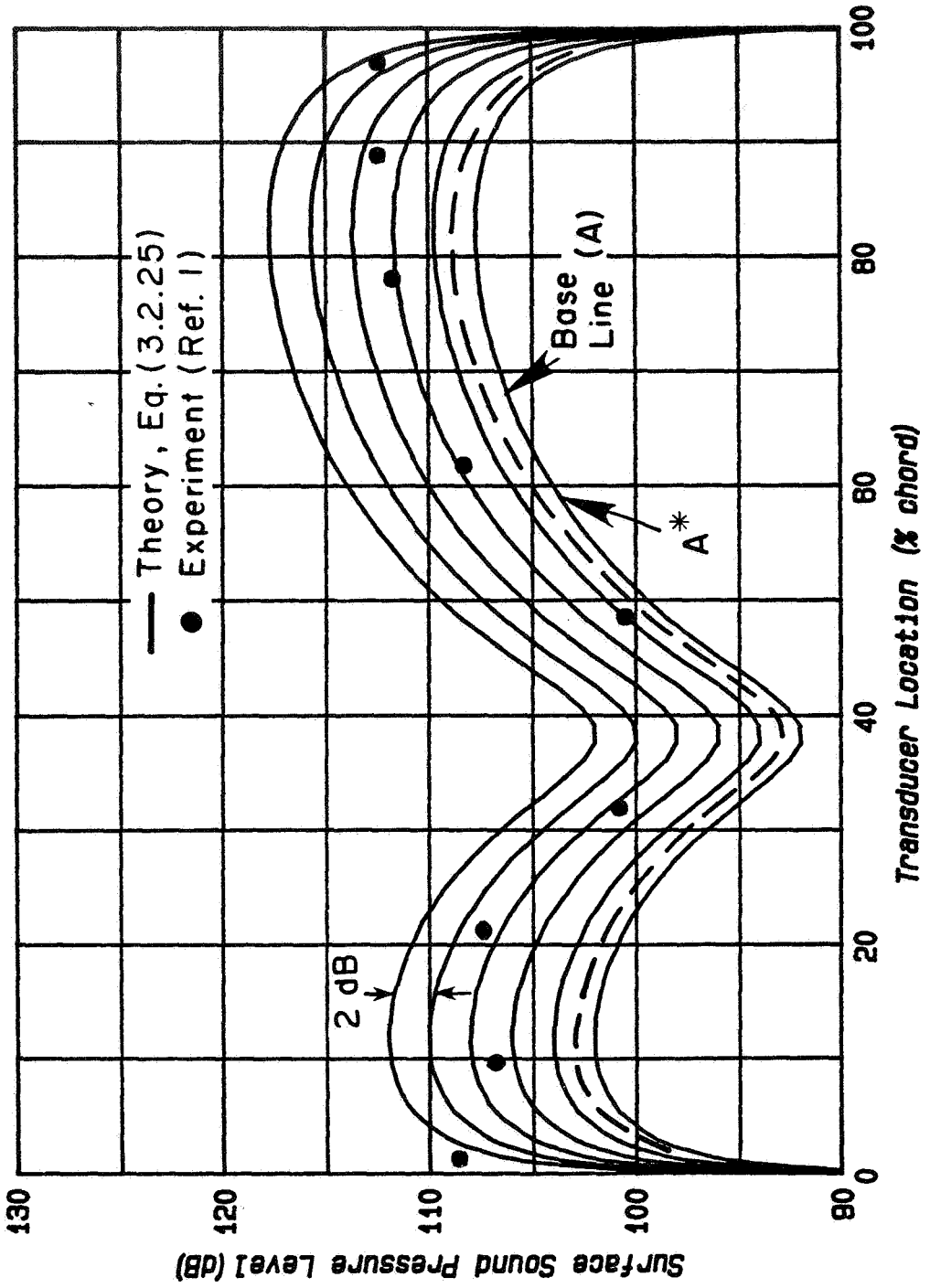

Figure B.3a Comparison of Theory and Experiment; k=1.989, α_o=30.8 μrad.

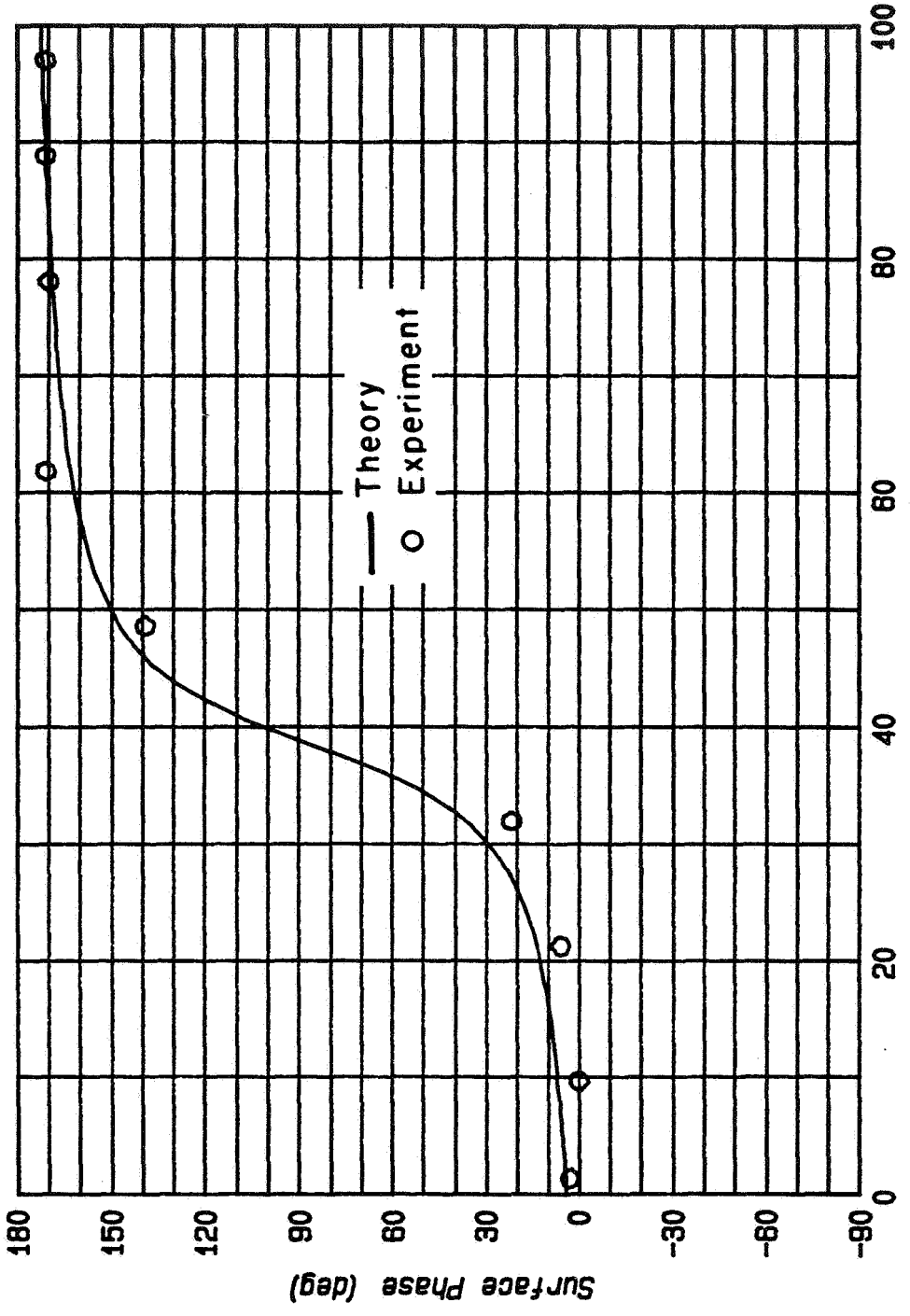

Figure B.3b Comparison of Theory and Experiment; k=1.989, α_o=30.8 μrad.

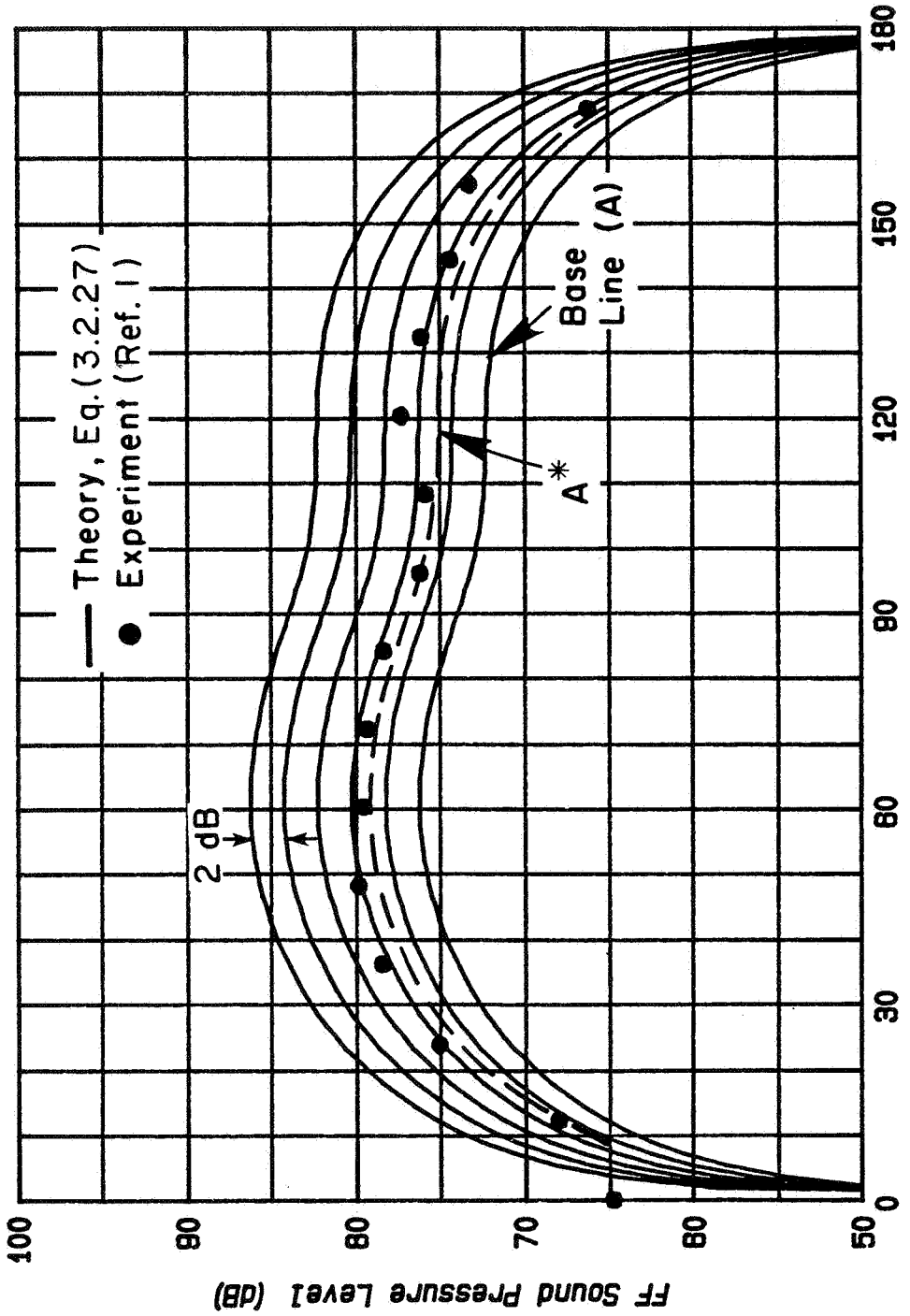

Figure B.3c Comparison of Theory and Experiment; k=1.989, α_o=30.8 μrad.

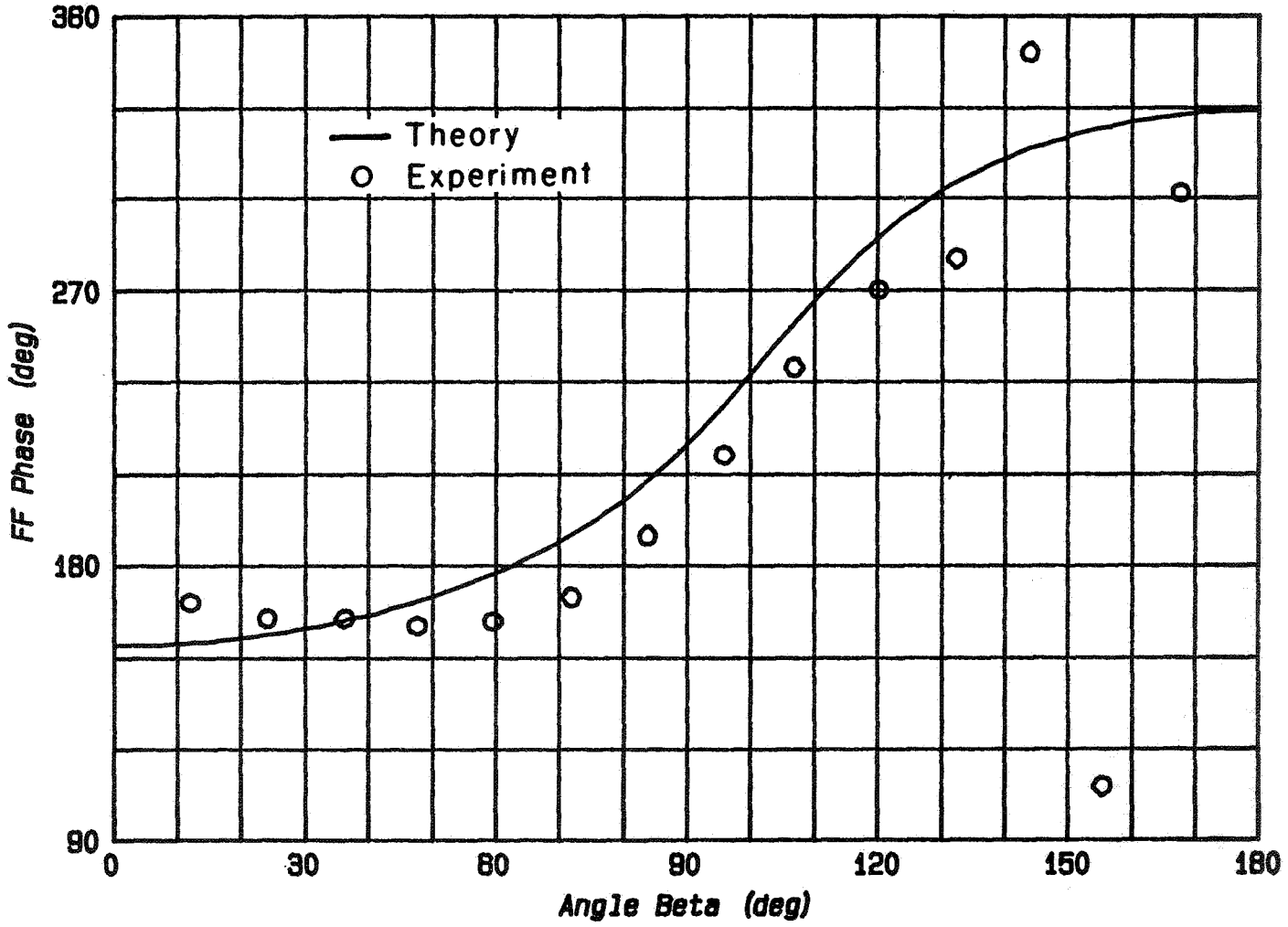

Figure B.3d Comparison of Theory and Experiment; k=1.989, α_0=30.8 μrad.

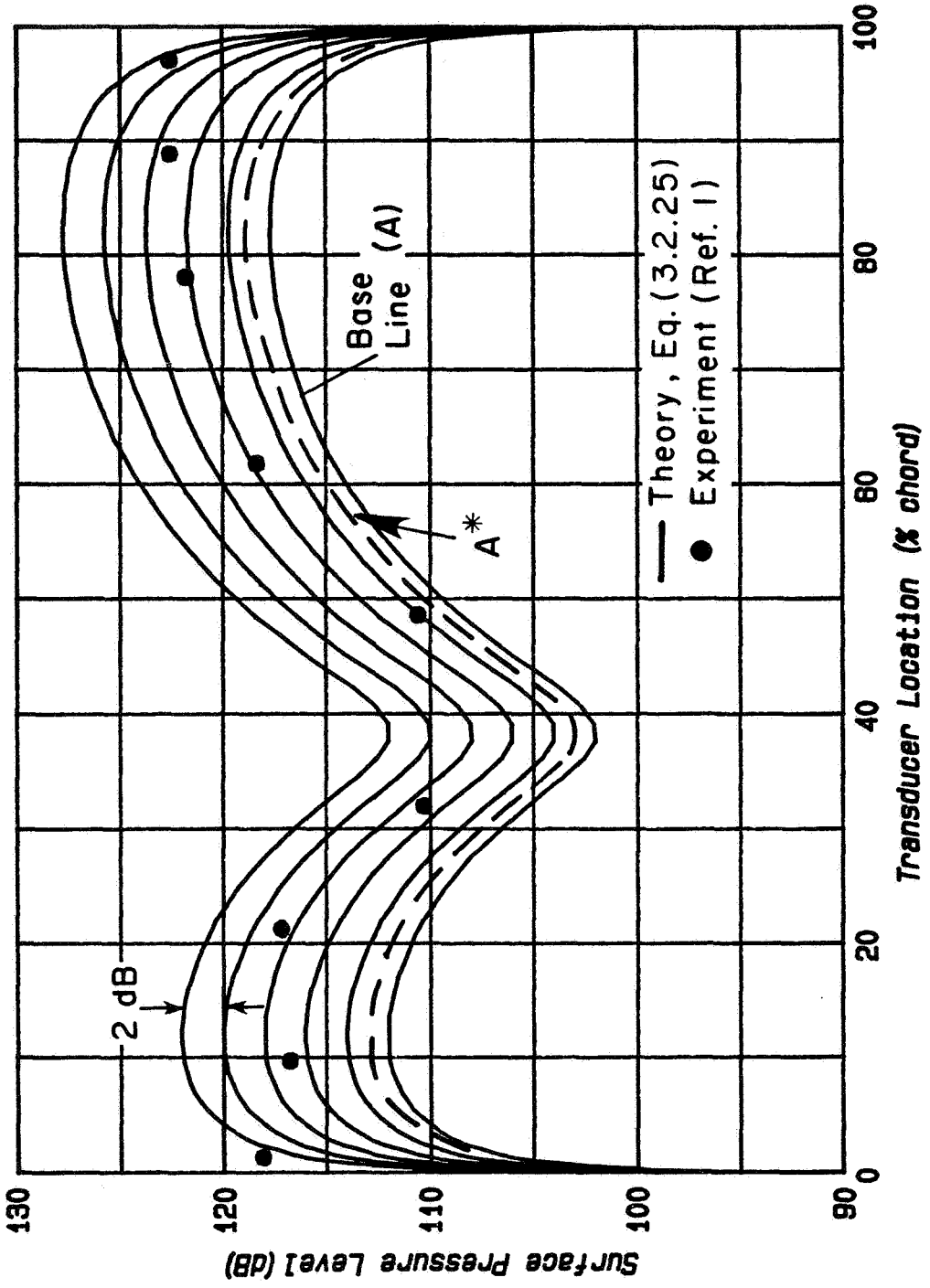

Figure B.4a Comparison of Theory and Experiment, k=1.989, α_o=97.6 μrad.

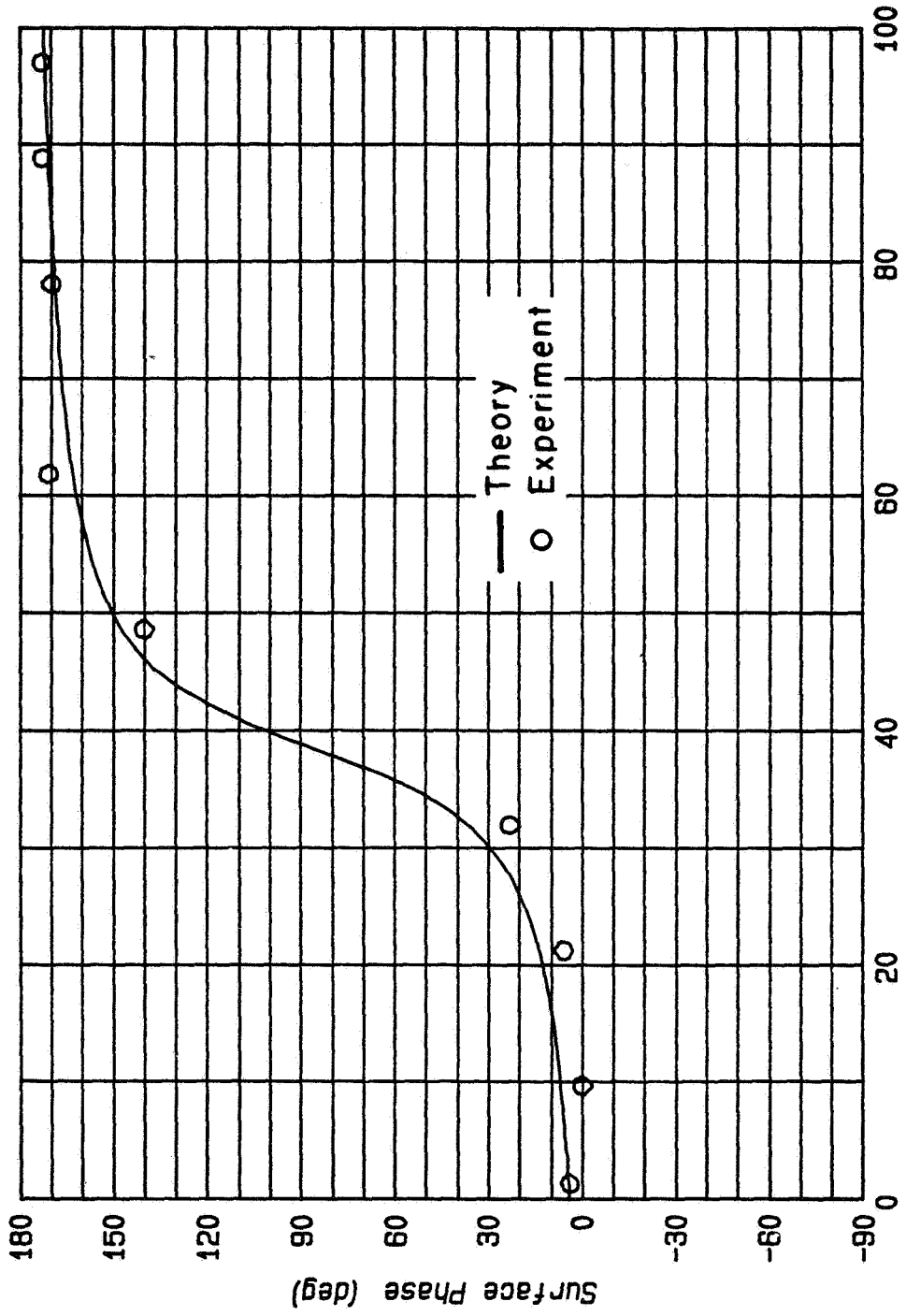

Figure B. 4b Comparison of Theory and Experiment, k=1.989, α_o=97.6 μrad.

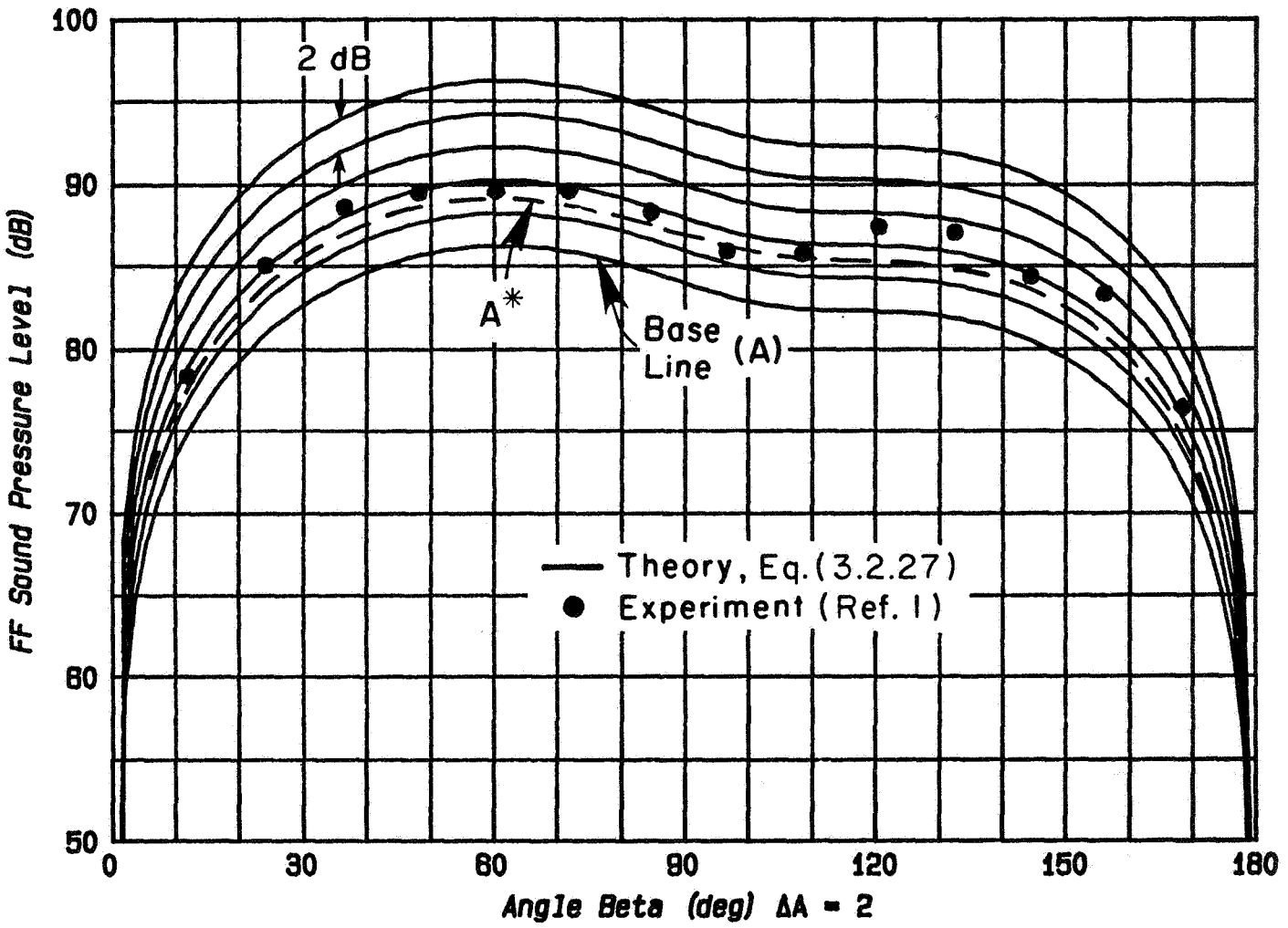

Figure B.4c Comparison of Theory and Experiment, k=1.989, α_0=97.6 μrad.

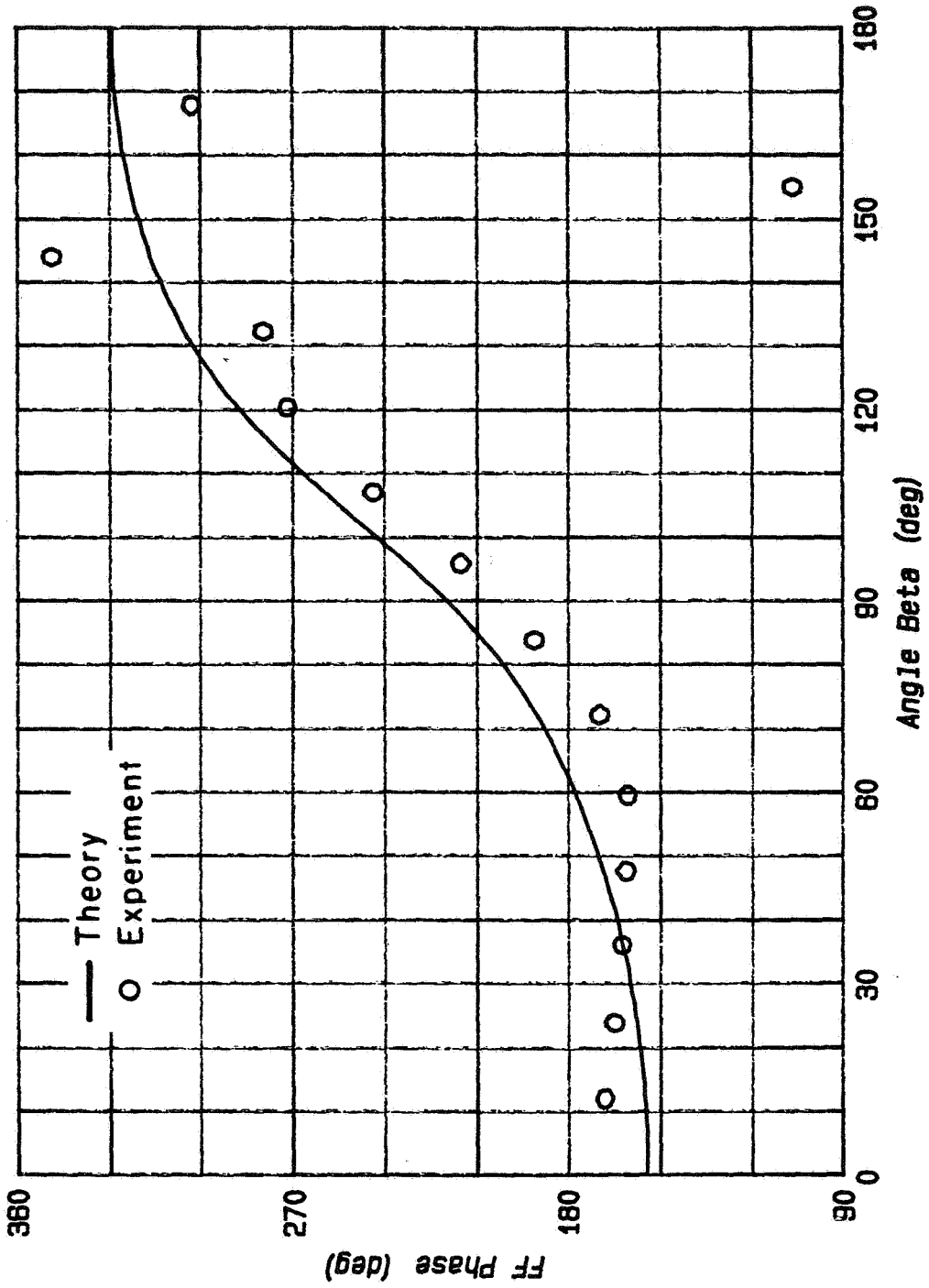

Figure B.4d Comparison of Theory and Experiment, k=1.989, α_o=97.6 μrad.

APPENDIX C
EFFECT OF ACCELERATION ON THE INVISCID FLAT PLATE THEORY

The theoretical calculations presented in this Appendix (Figs. C.1 through C.4) are based on Eq. (3.5.1) for the surface pressure and phase and on Eq. (3.2.27) for the far field. A complete discussion of these results is given in Section 3.5. The baseline curve on each graph is calculated with the actual geometric aspect ratio, A = 0.666. The successive amplitude curves are calculated for an acceleration increment $\Delta e = 0.1 (\approx 0.27$ Pa/g). The dashed curves denote the location of the peak surface pressures. The experimental amplitude data of Ref. 1 are denoted by solid symbols, and the phase data are denoted by open symbols. The Helmholtz number, k, and micro-radian amplitude, α_o, are noted in the title of each graph.

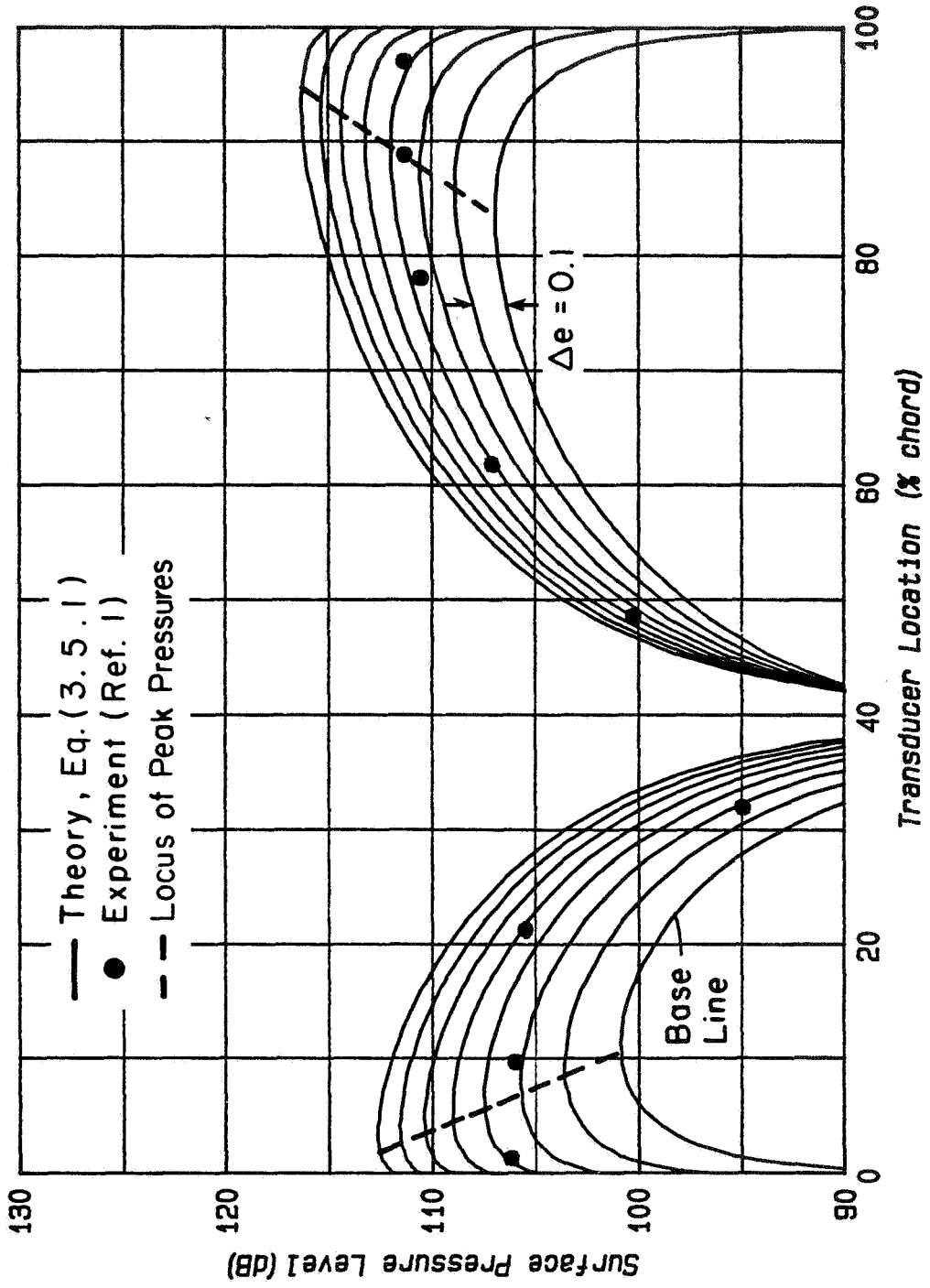

Figure C.1a Comparison of Inviscid Theory (with Acceleration Contamination) and Experiment; k=1.255, α_o=82.1 μrad.

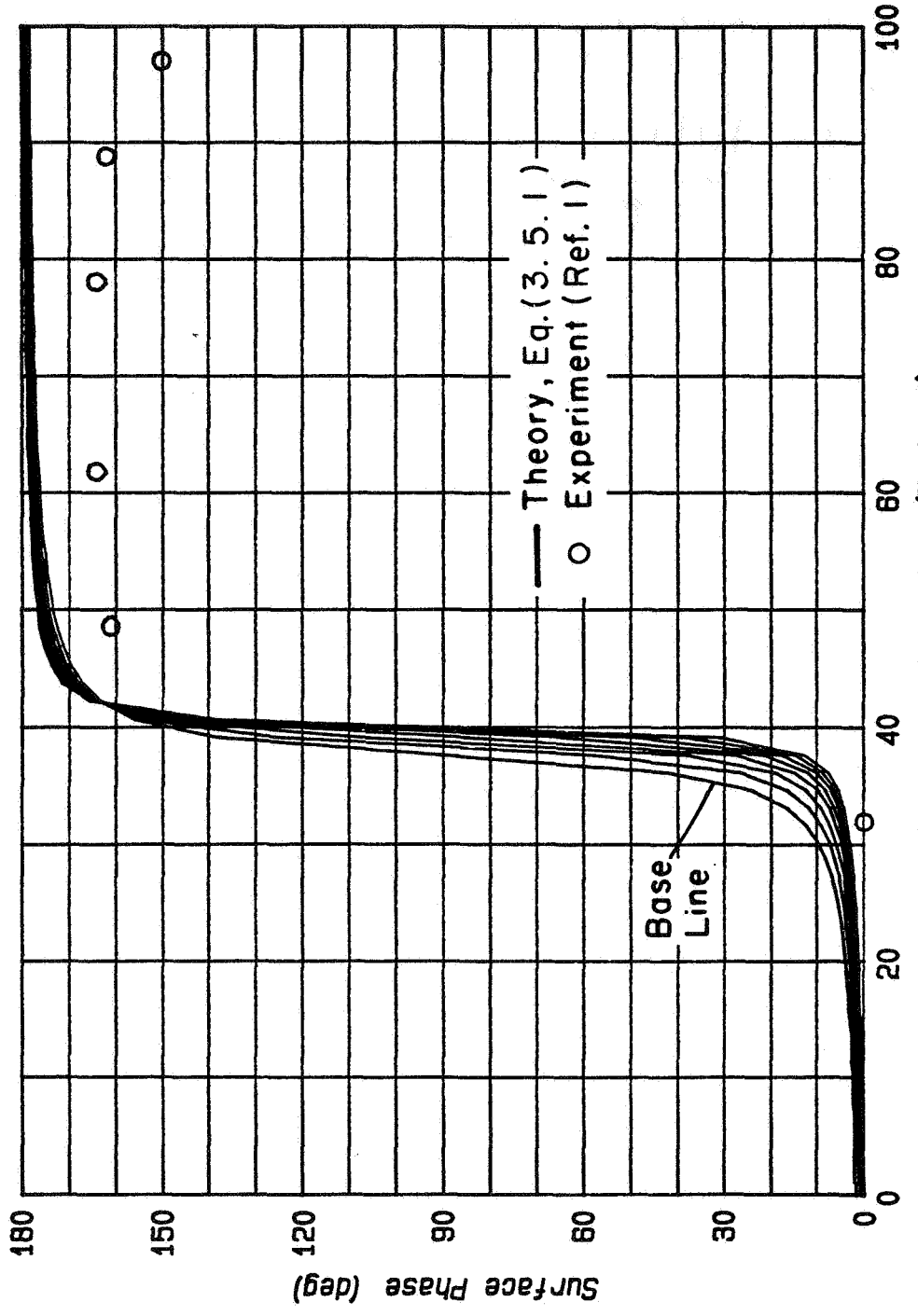

Figure C.1b Comparison of Inviscid Theory (with Acceleration Contamination) and Experiment; k=1.255, α_o=82.1 μrad.

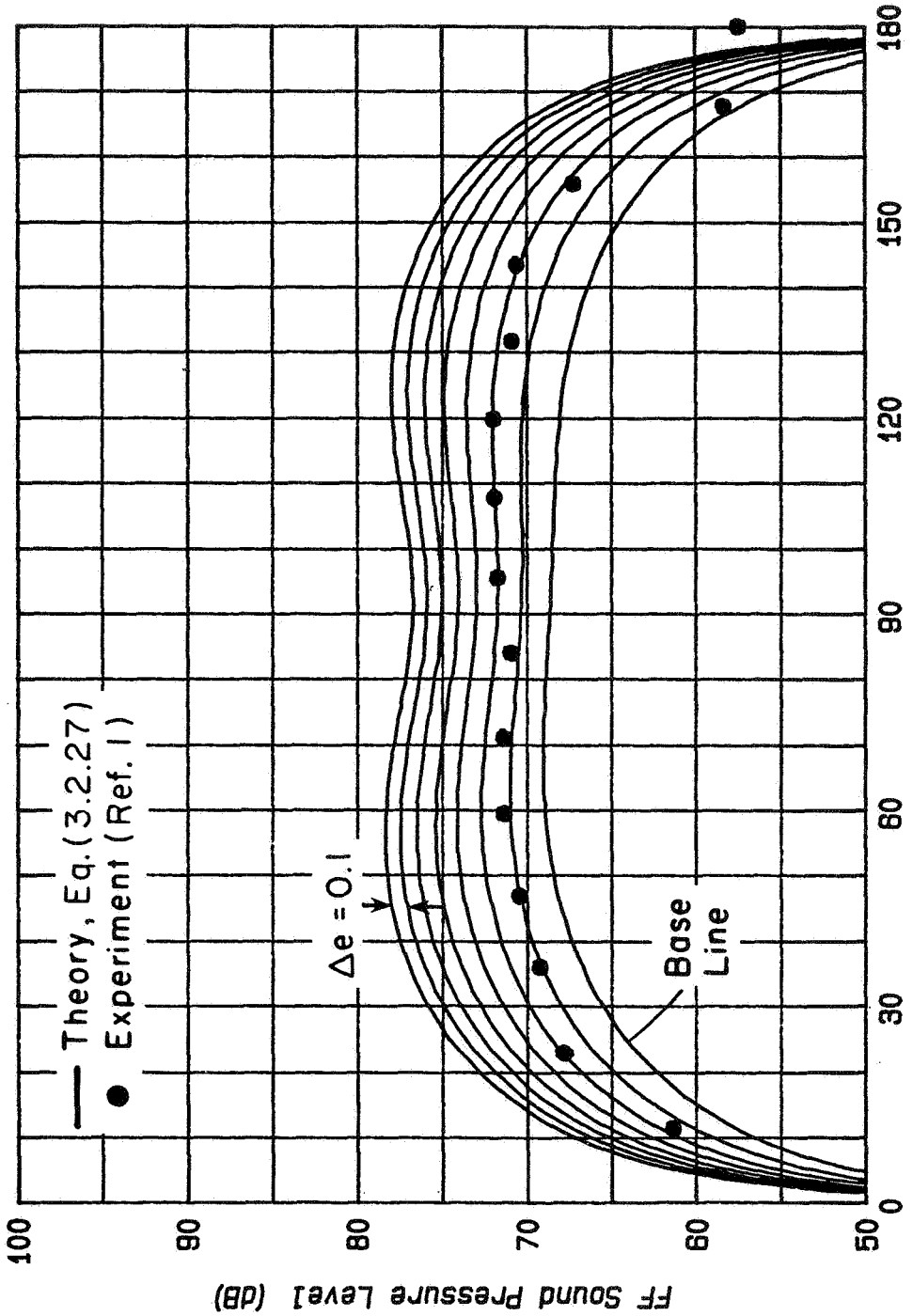

Figure C.1c Comparison of Inviscid Theory (with Acceleration Contamination) and Experiment; k=1.255, α_o=82.1 μrad.

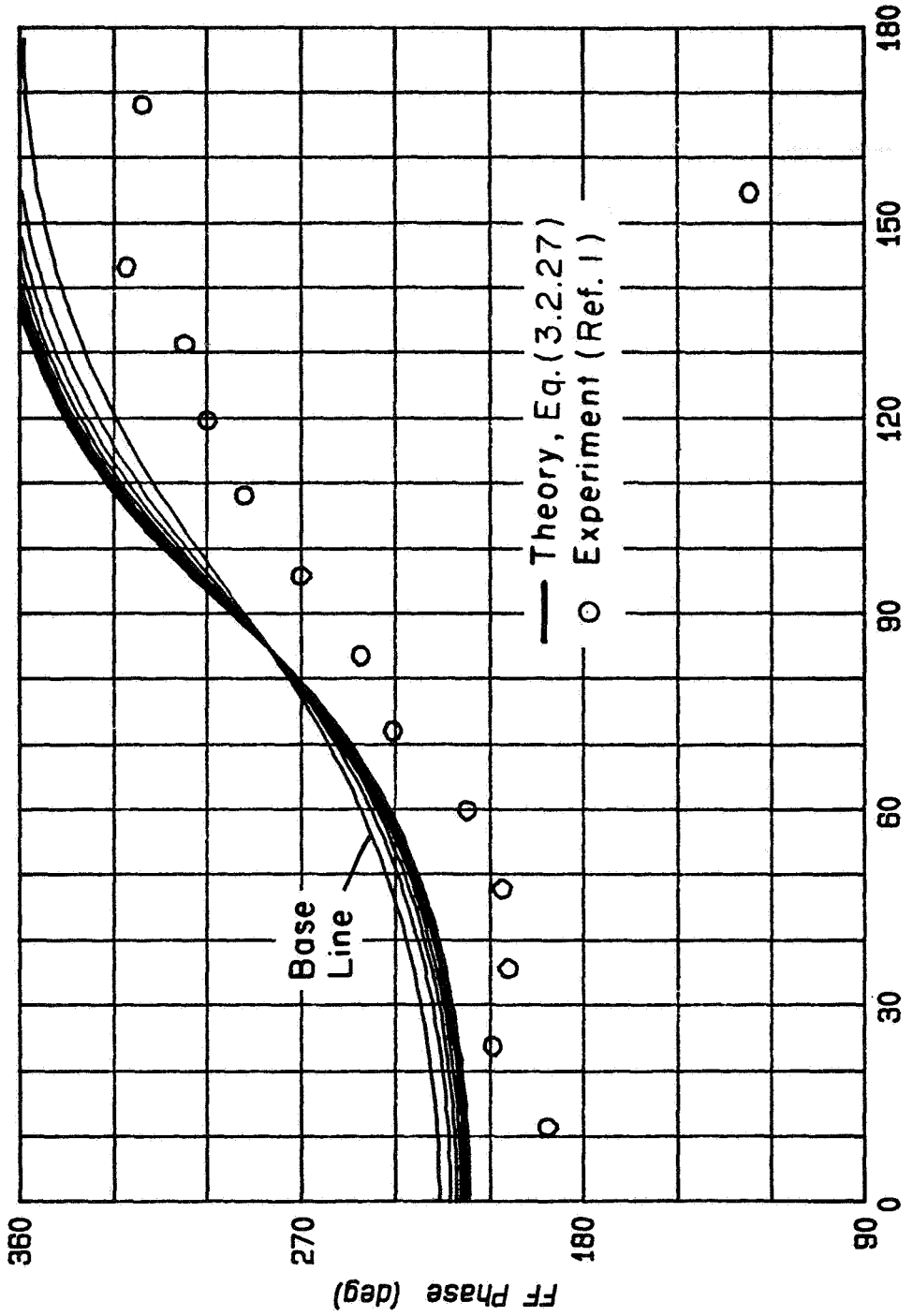

Figure C.1d Comparison of Inviscid Theory (with Acceleration Contamination) and Experiment; k=1.255, α_o=82.1 μrad.

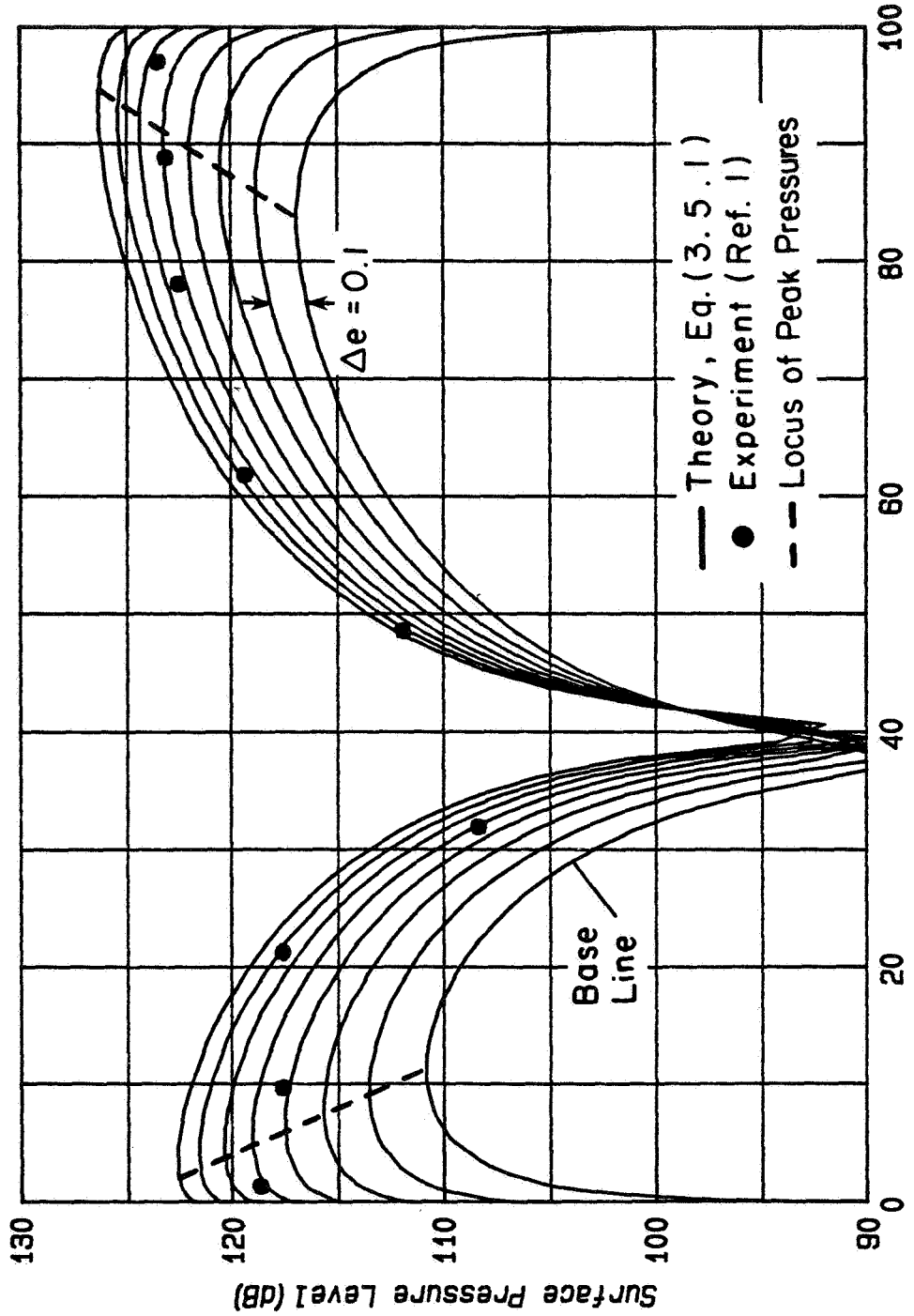

Figure C.2a Comparison of Inviscid Theory (with Acceleration Contamination) and Experiment; k=1.255, α_o=259.3 μrad.

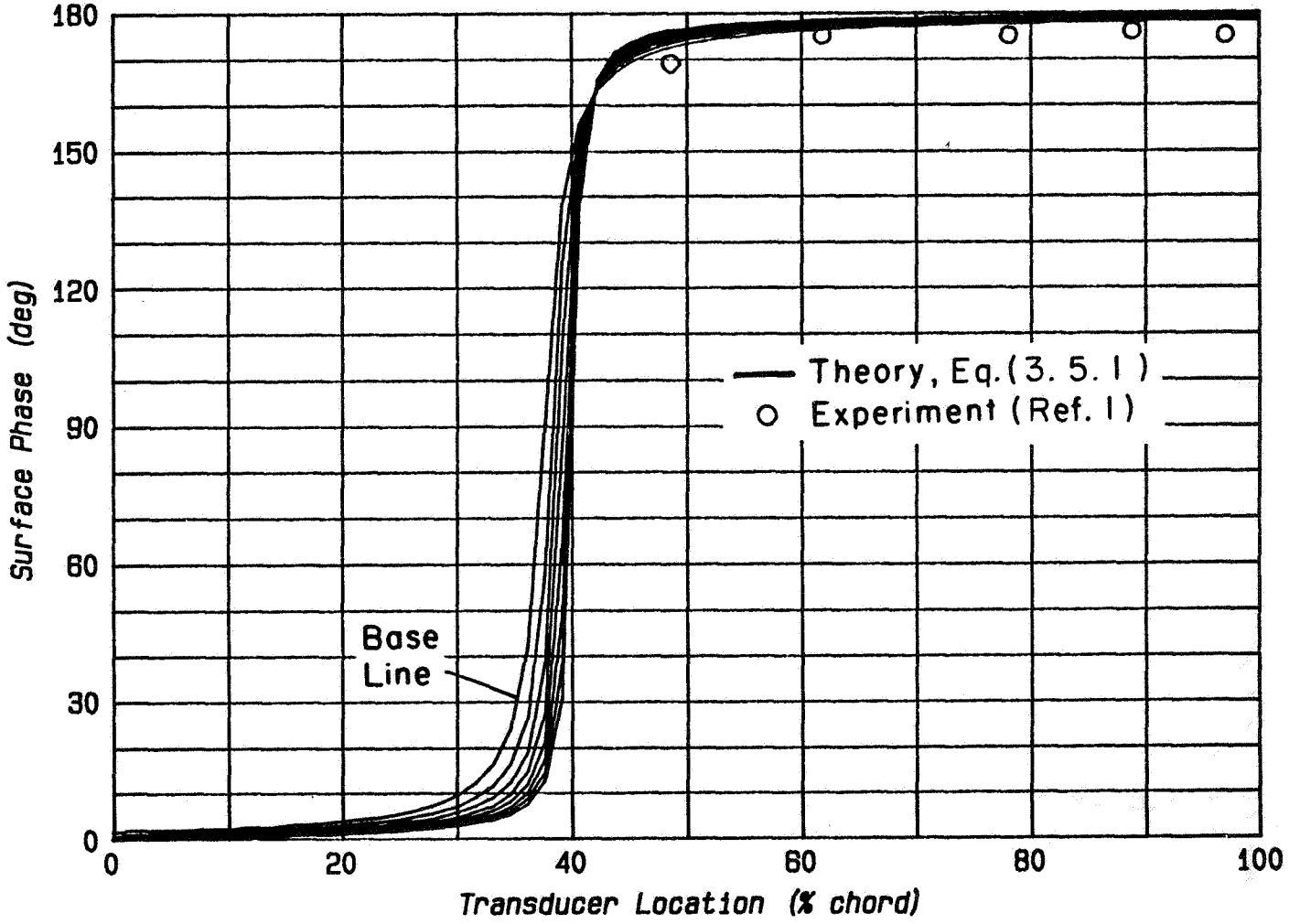

Figure C.2b Comparison of Inviscid Theory (with Acceleration Contamination) and Experiment; k=1.255, α_o=259.3 μrad.

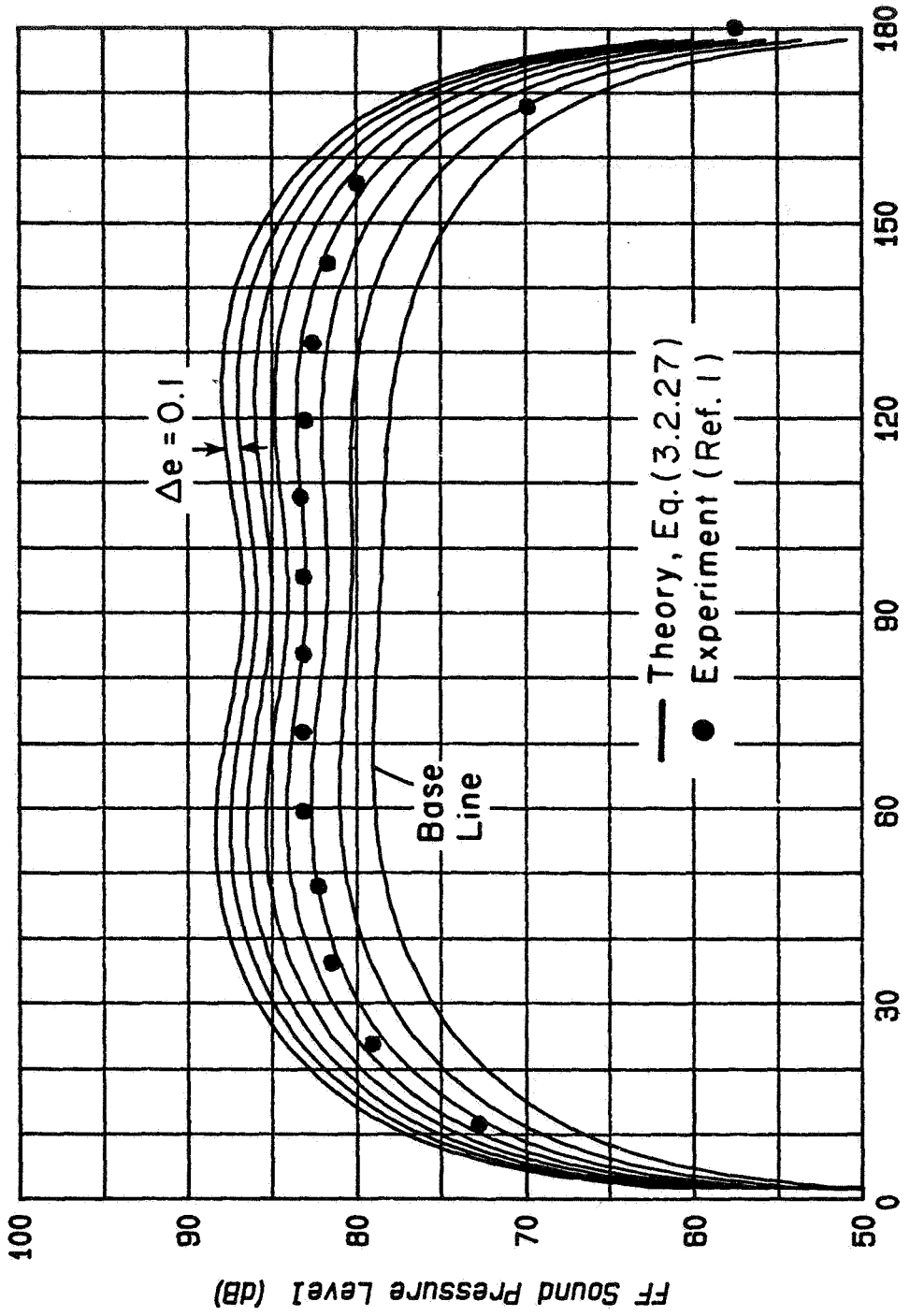

Figure C.2c Comparison of Inviscid Theory (with Acceleration Contamination) and Experiment; k=1.255, α_o=259.3 μrad.

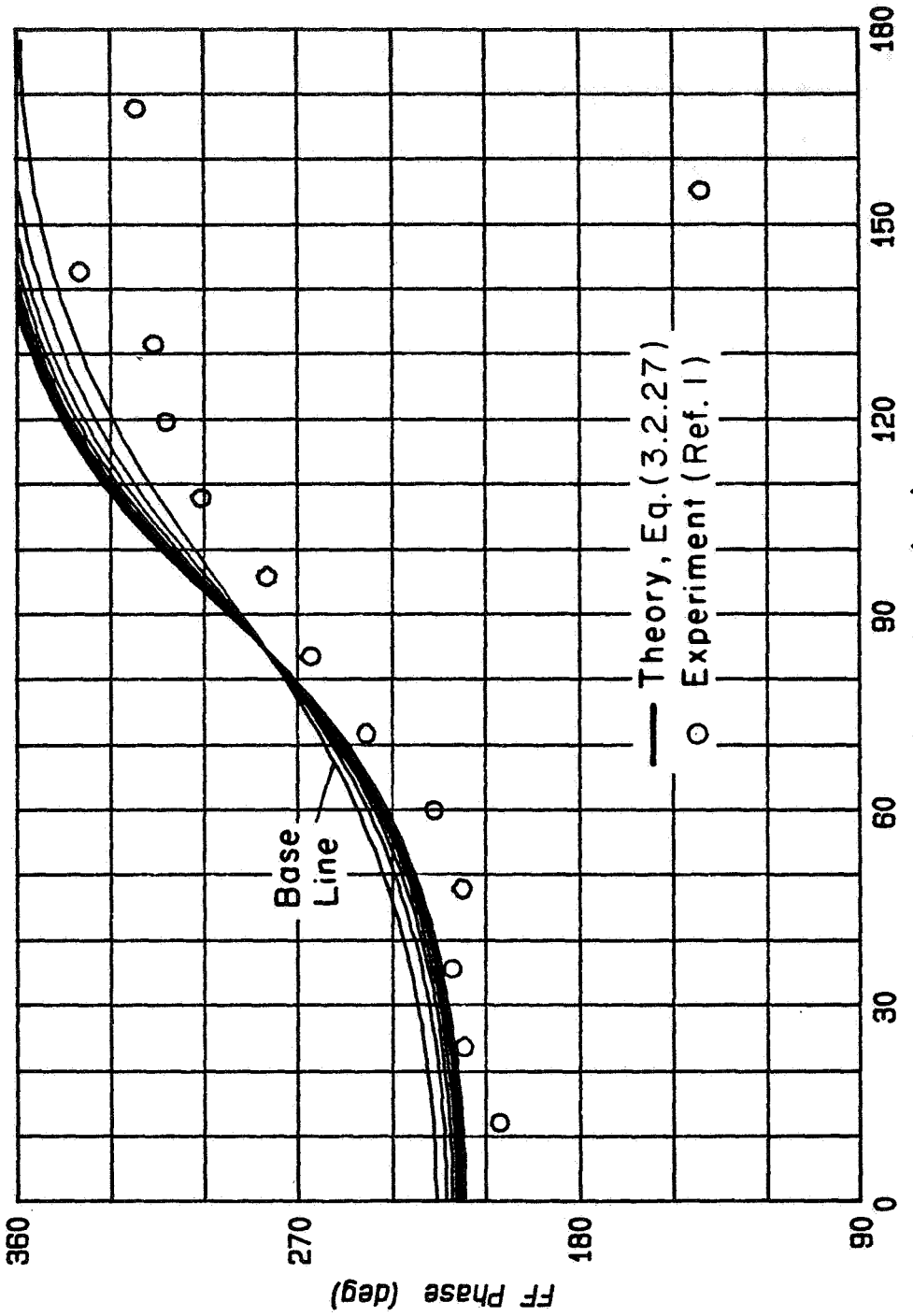

Figure C.2d Comparison of Inviscid Theory (with Acceleration Contamination) and Experiment; k=1.255, α_o=259.3 μrad.

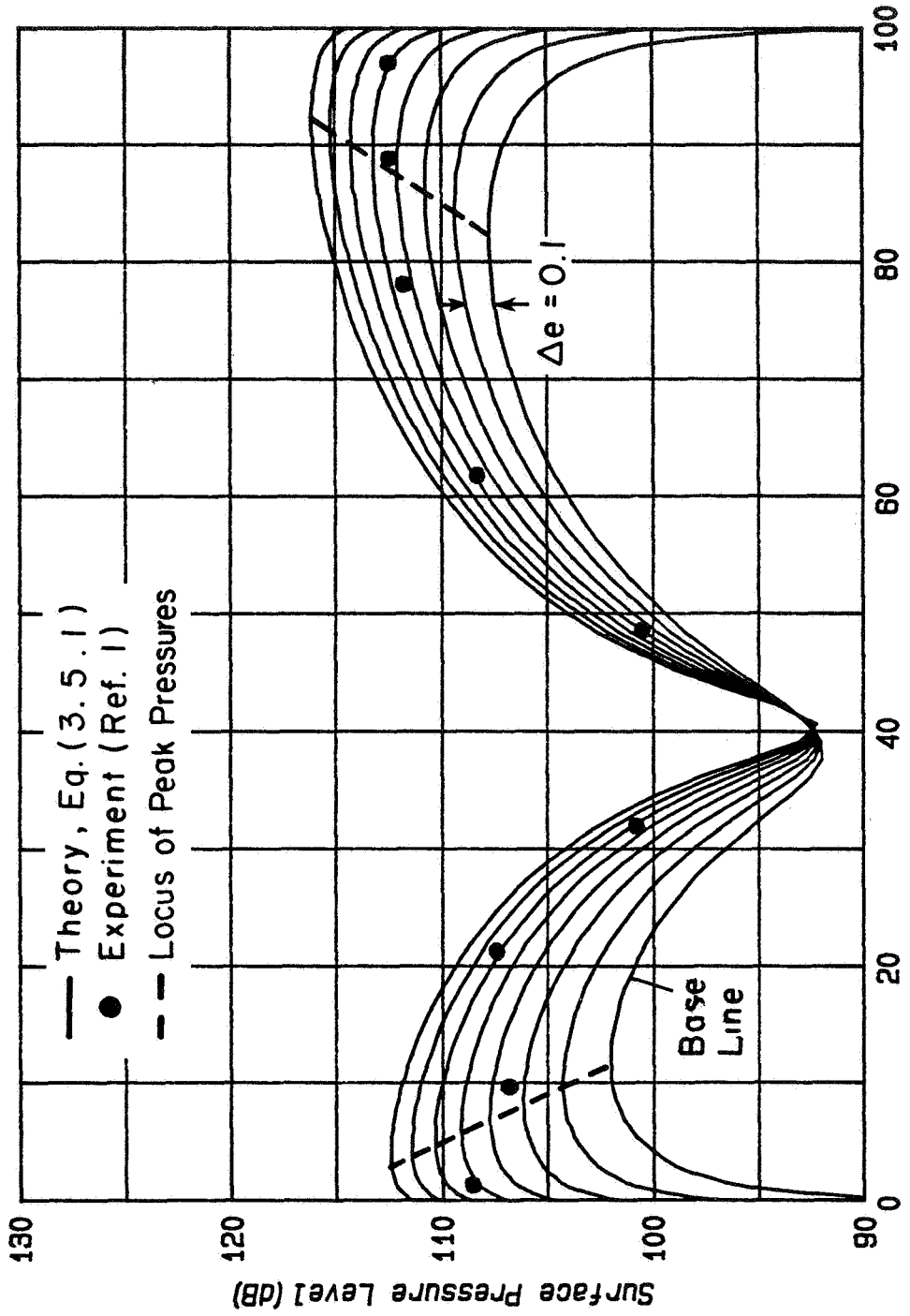

Figure C.3a Comparison of Inviscid Theory (with Acceleration Contamination) and Experiment; k=1.989, α_o=30.8 μrad.

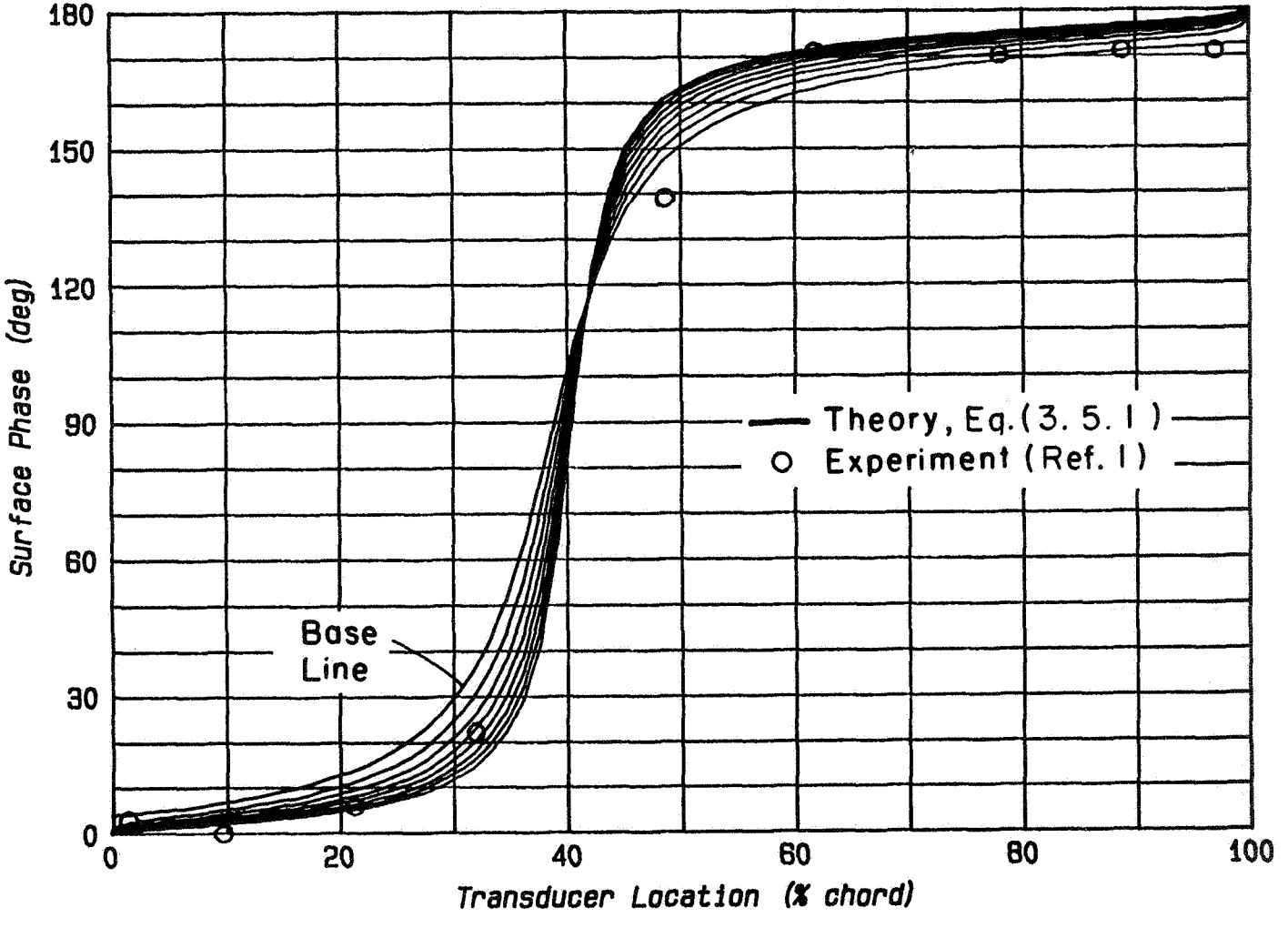

Figure C.3b Comparison of Inviscid Theory (with Acceleration Contamination) and Experiment; k=1.989, α_o=30.8 μrad.

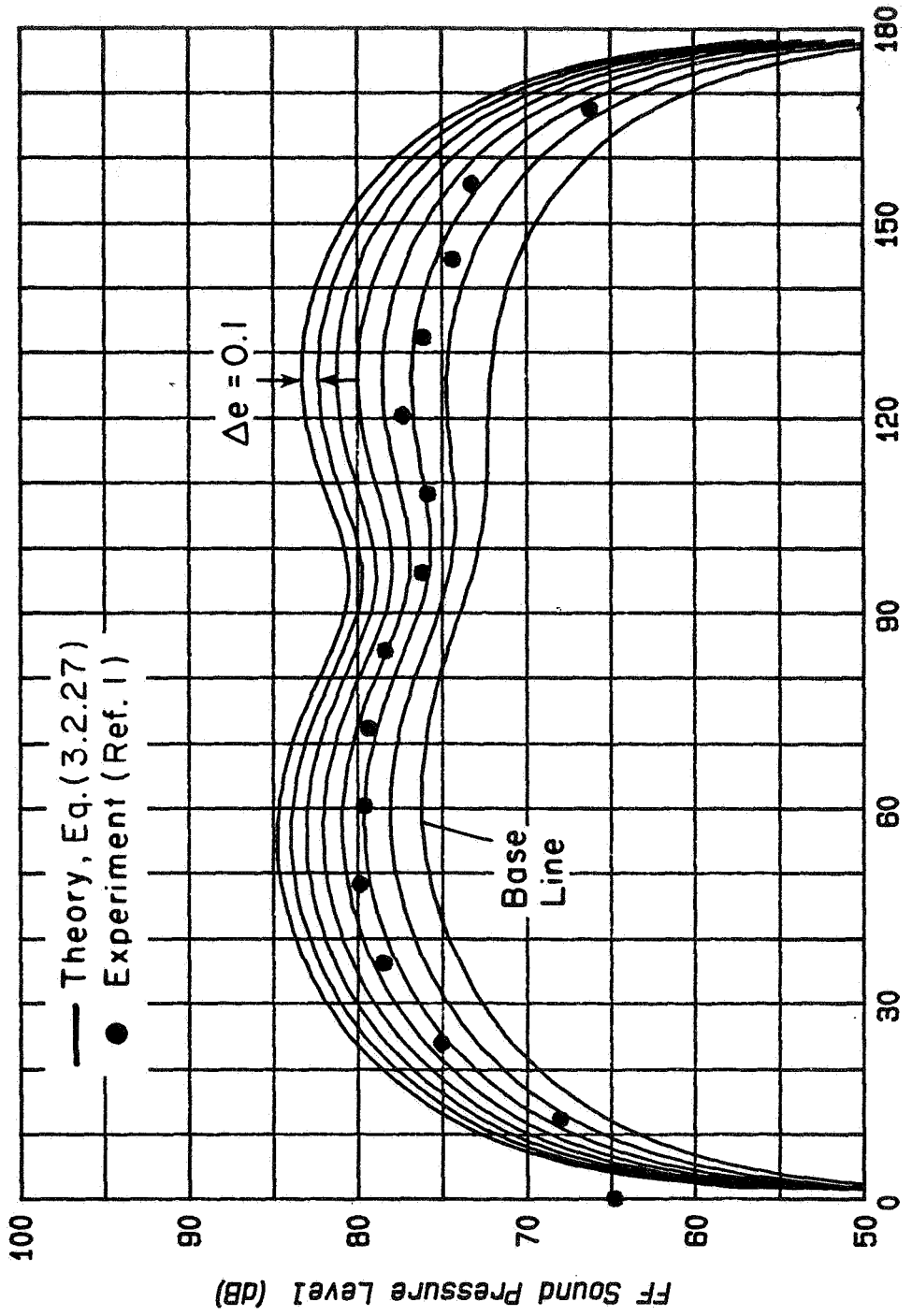

Figure C.3c Comparison of Inviscid Theory (with Acceleration Contaimination) and Experiment; k=1.989, α_o=30.8 μrad.

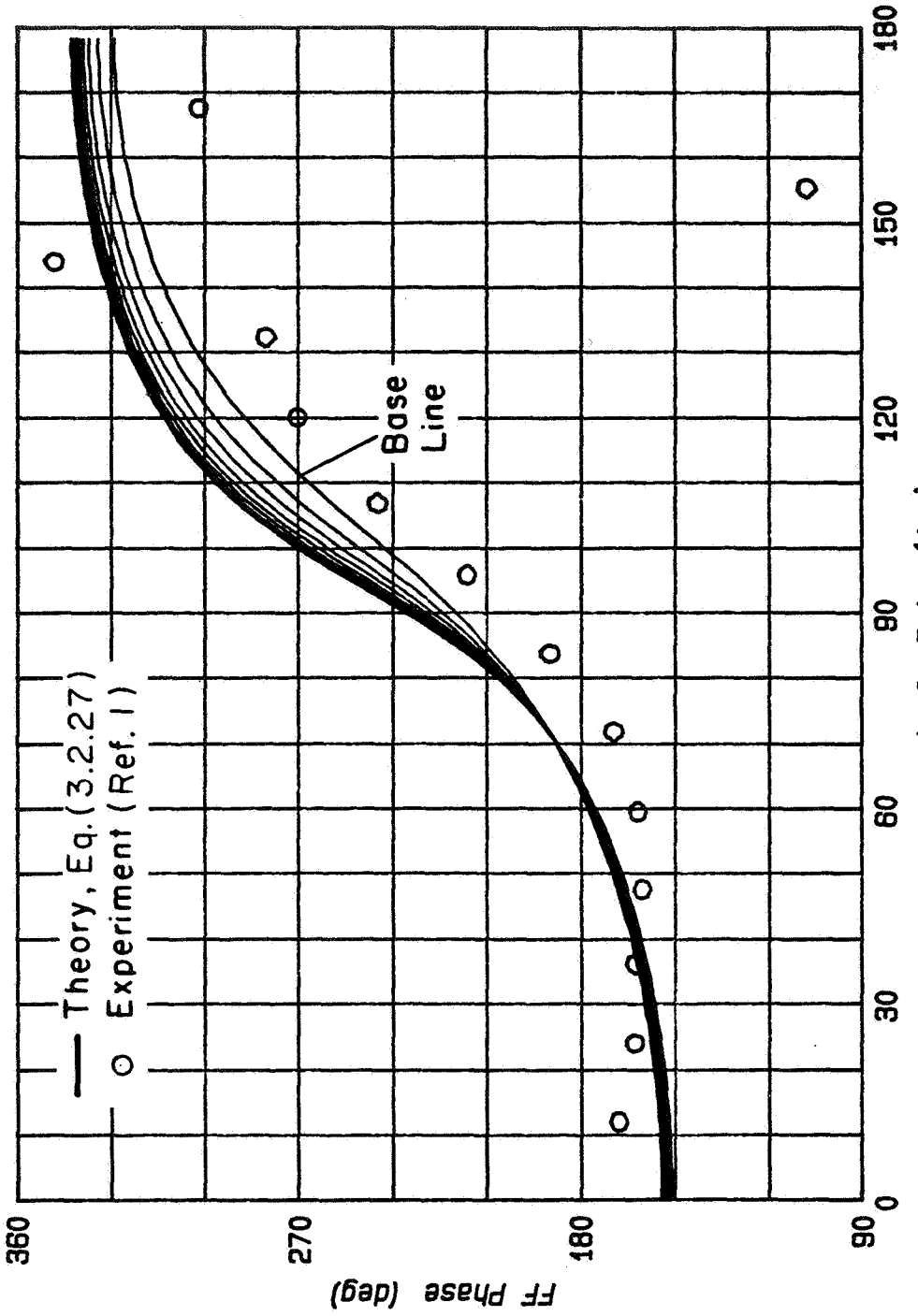

Figure C.3d Comparison of Inviscid Theory (with Acceleration Contamination) and Experiment; k=1.989, α_o=30.8 μrad.

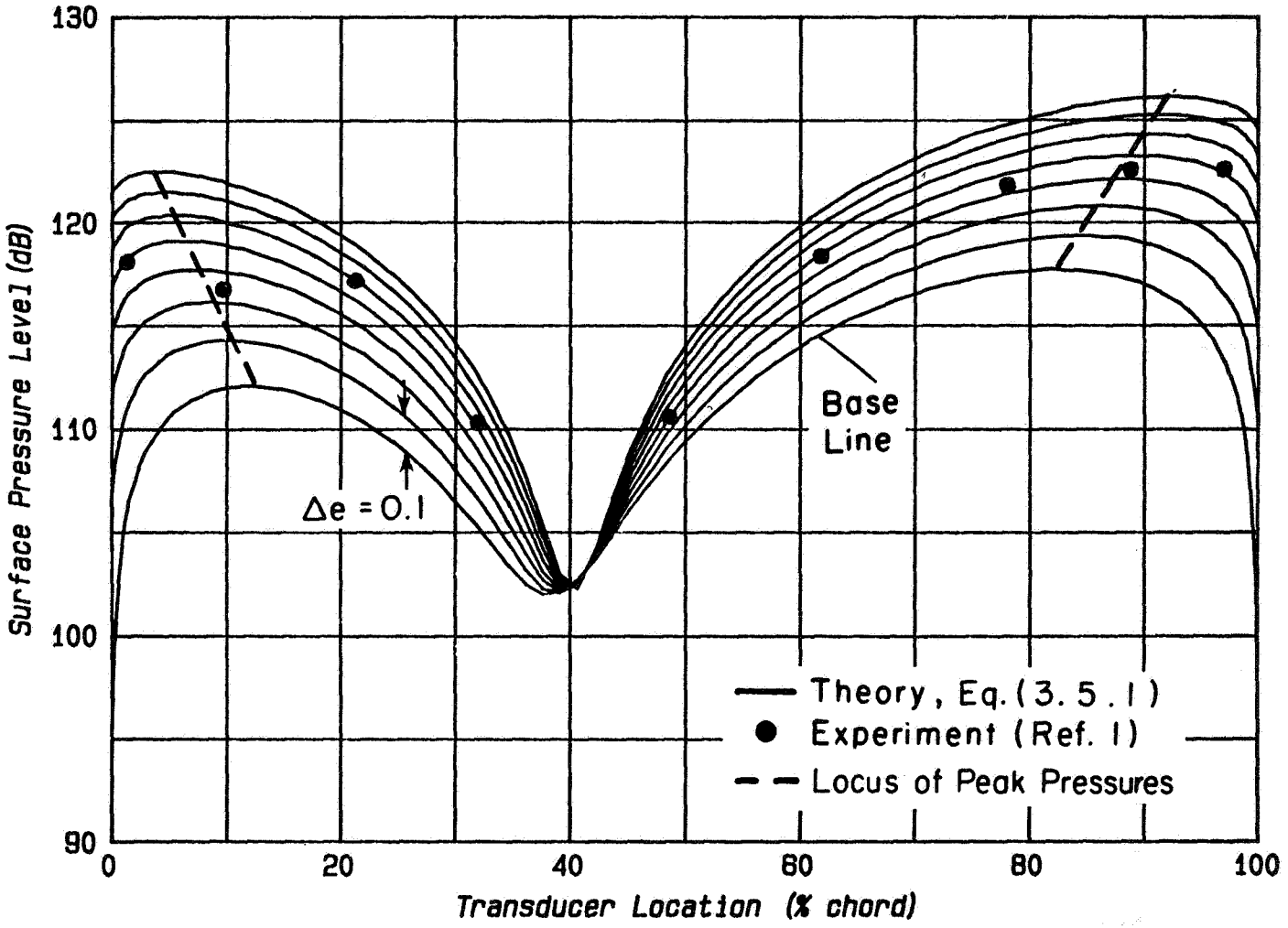

Figure C.4a Comparison of Inviscid Theory (with Acceleration Contamination) and Experiment; k=1.989, α_o=97.6 μrad.

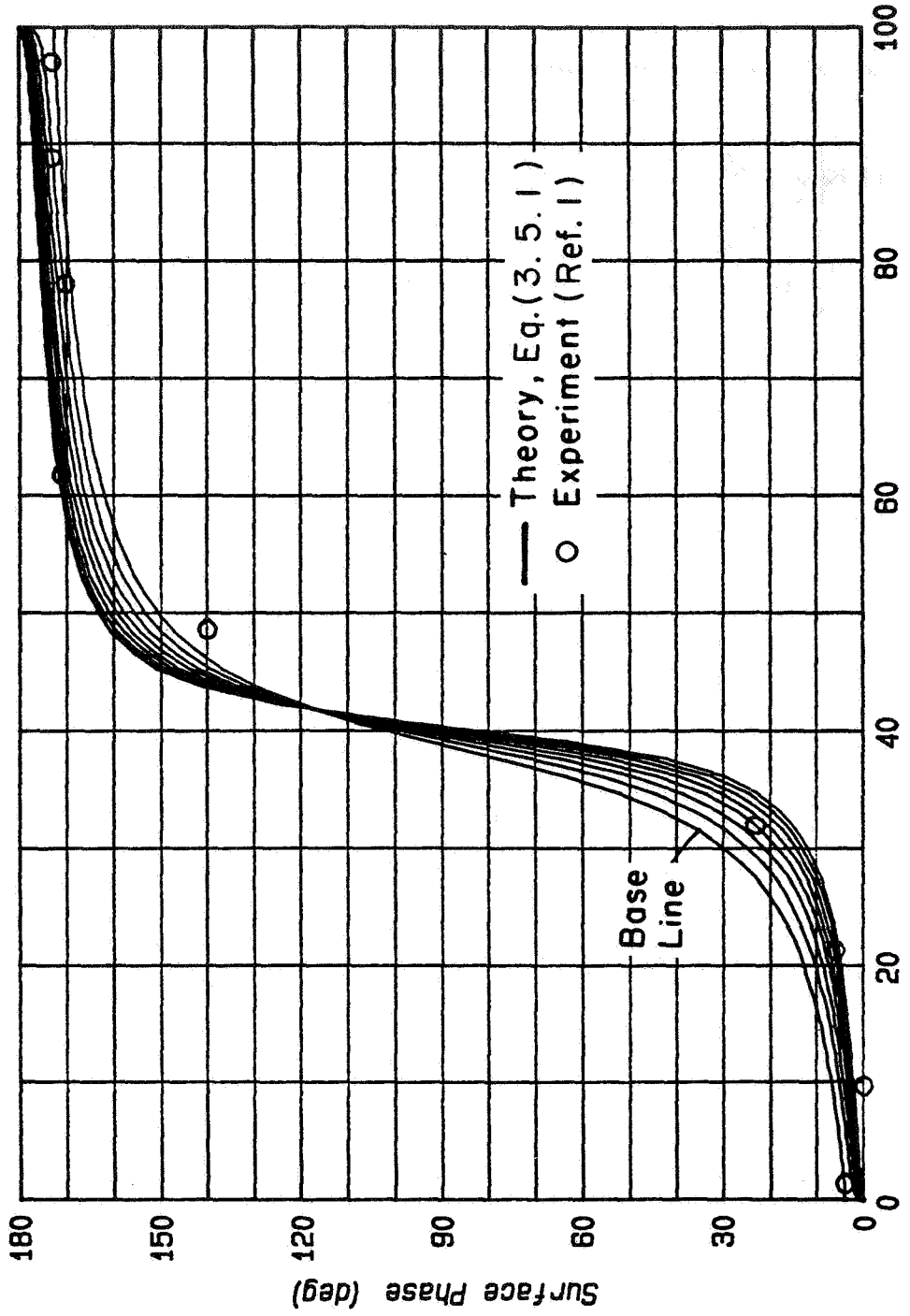

Figure C.4b Comparison of Inviscid Theory (with Acceleration Contamination) and Experiment; k=1.989, α_o=7.6 μrad.

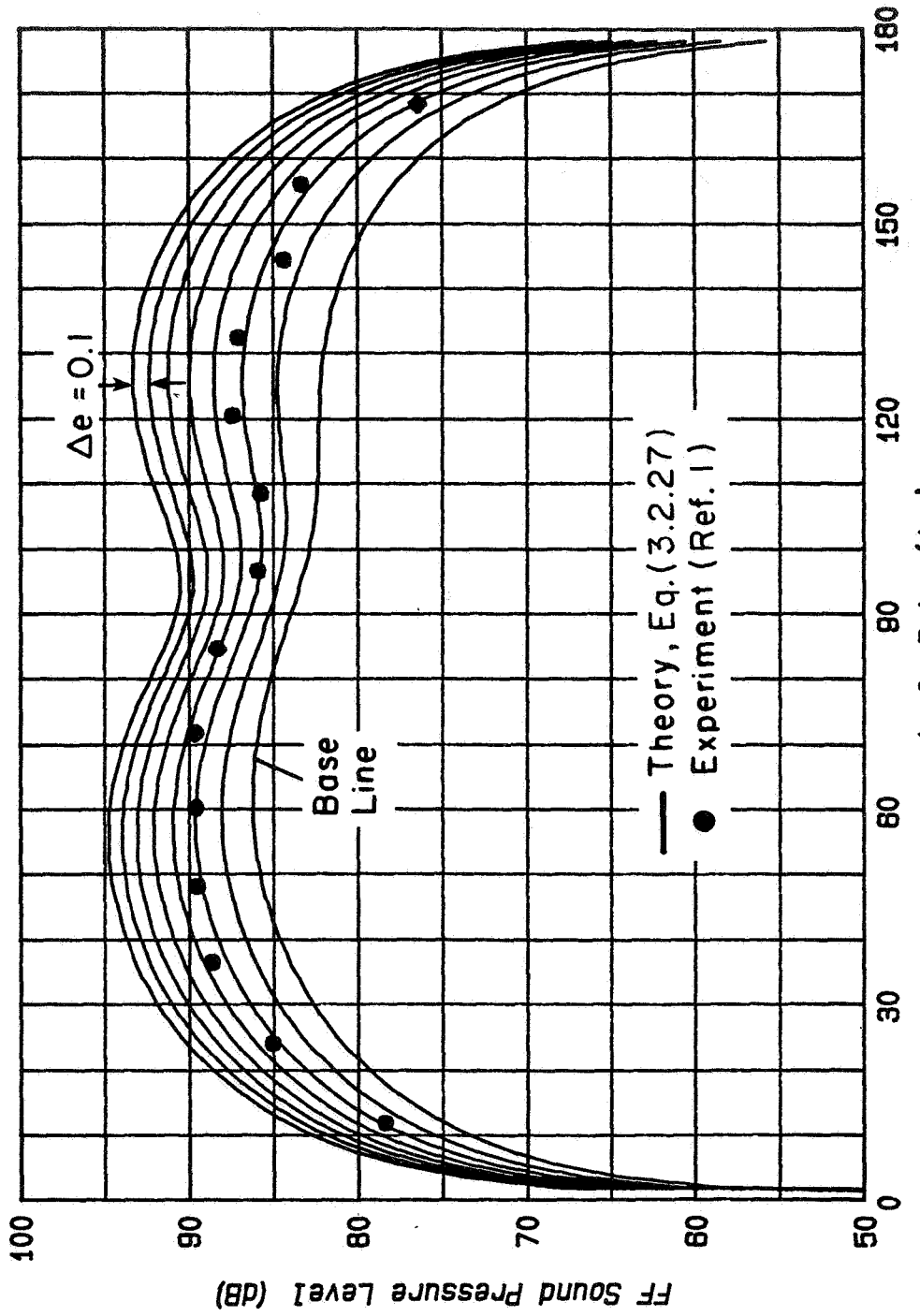

Figure C.4c Comparison of Inviscid Theory (with Acceleration Contamination) and Experiment; k=1.989, α_o=97.6 μrad.

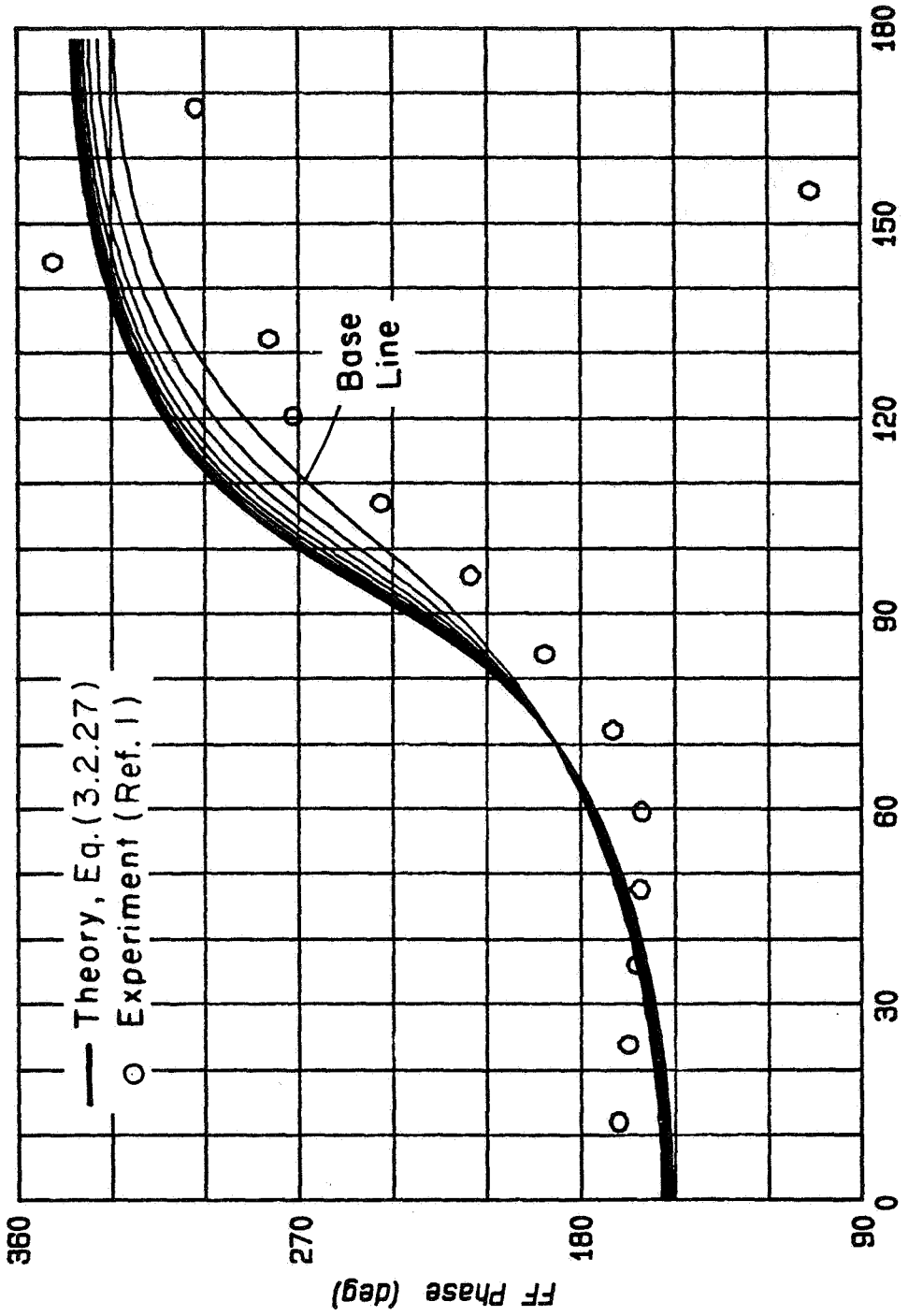

Figure C.4d Comparison of Inviscid Theory (with Acceleration Contamination) and Experiment; k=1.989, α_o=97.6 μrad.

APPENDIX D
EFFECT OF IN-PLANE VIBRATION ON THE INVISCID FLAT PLATE THEORY

The theoretical calculation presented in this Appendix (Figs. D.1 through D.4) are based on Eq. (3.6.1) for the surface pressure and phase and on Eq. (3.6.2) for the far field. A complete discussion of these results is given in Section 3.6. The baseline curve on each graph is calculated with the actual geometric aspect ratio, A = 0.666. The successive amplitude curves are calculated for an increment of in-plane vibration, Δe, with amplitude equal to 0.2 of the transverse displacement at the trailing edge due to torsional vibration. The dashed curve denotes the location of the peak surface pressure. The experimental amplitude data of Ref. 1 are denoted by the solid symbols, and the phase data are denoted by the open symbols. The Helmholtz number, k, and the micro-radian amplitude, α_0, are noted in the title of each graph.

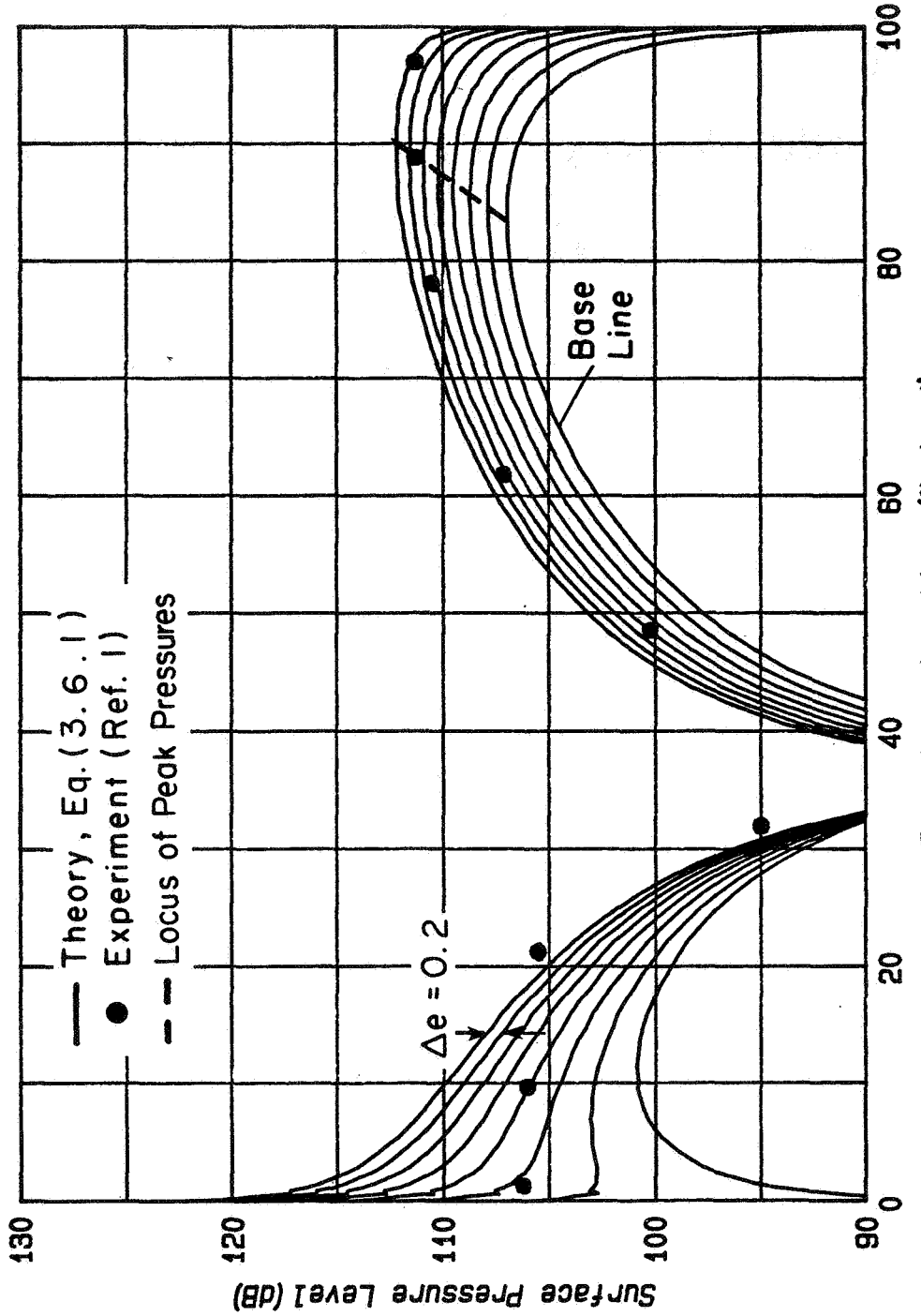

Figure D.1a Comparison of Inviscid Theory (with in-plane Vibration Contamination) with Experiment; k=1.255, α_o=82.1 μrad.

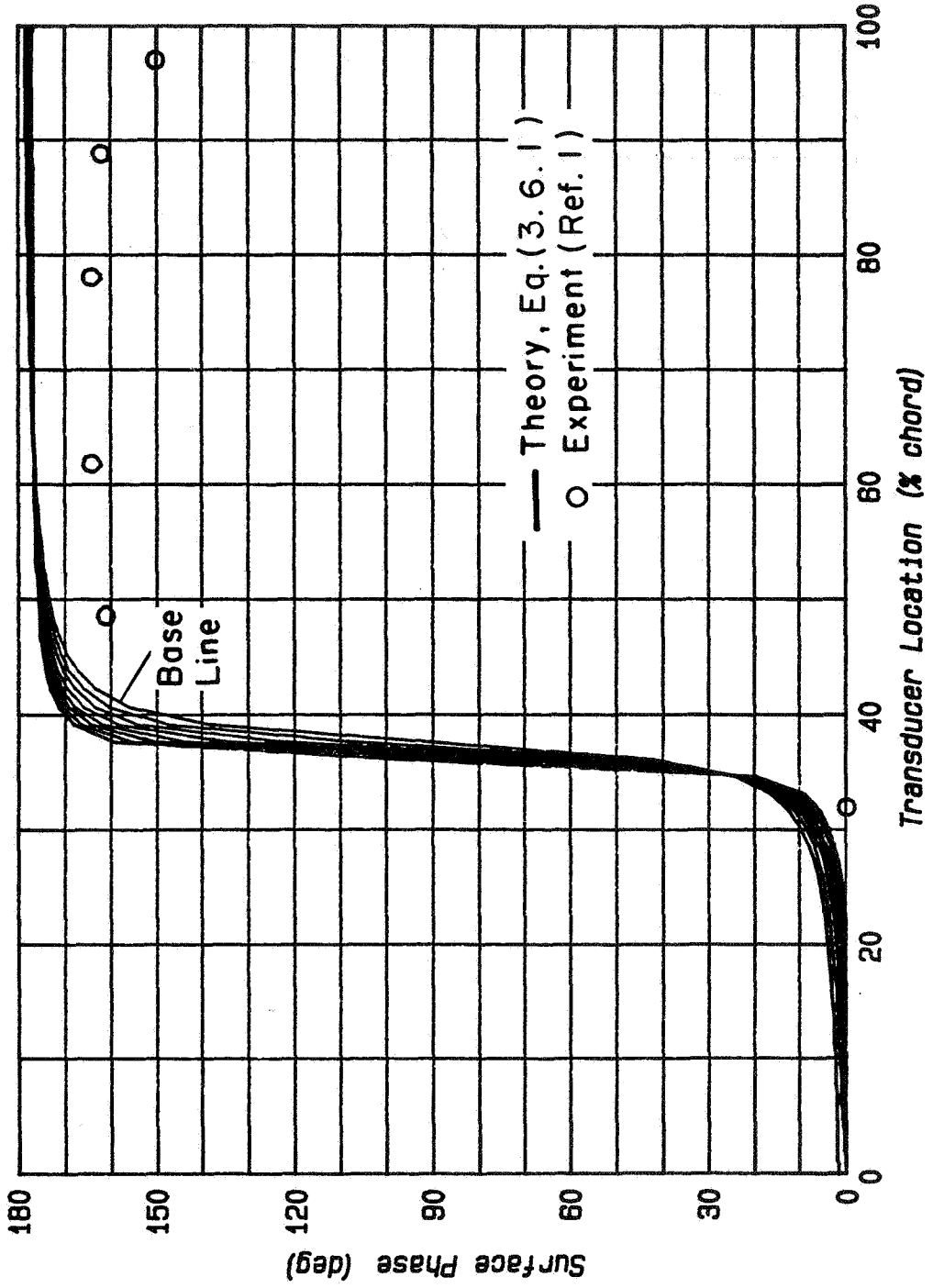

Figure D.1b Comparison of Inviscid Theory (with in-plane Vibration Contamination) with Experiment; k=1.255, α_o=82.1 μrad.

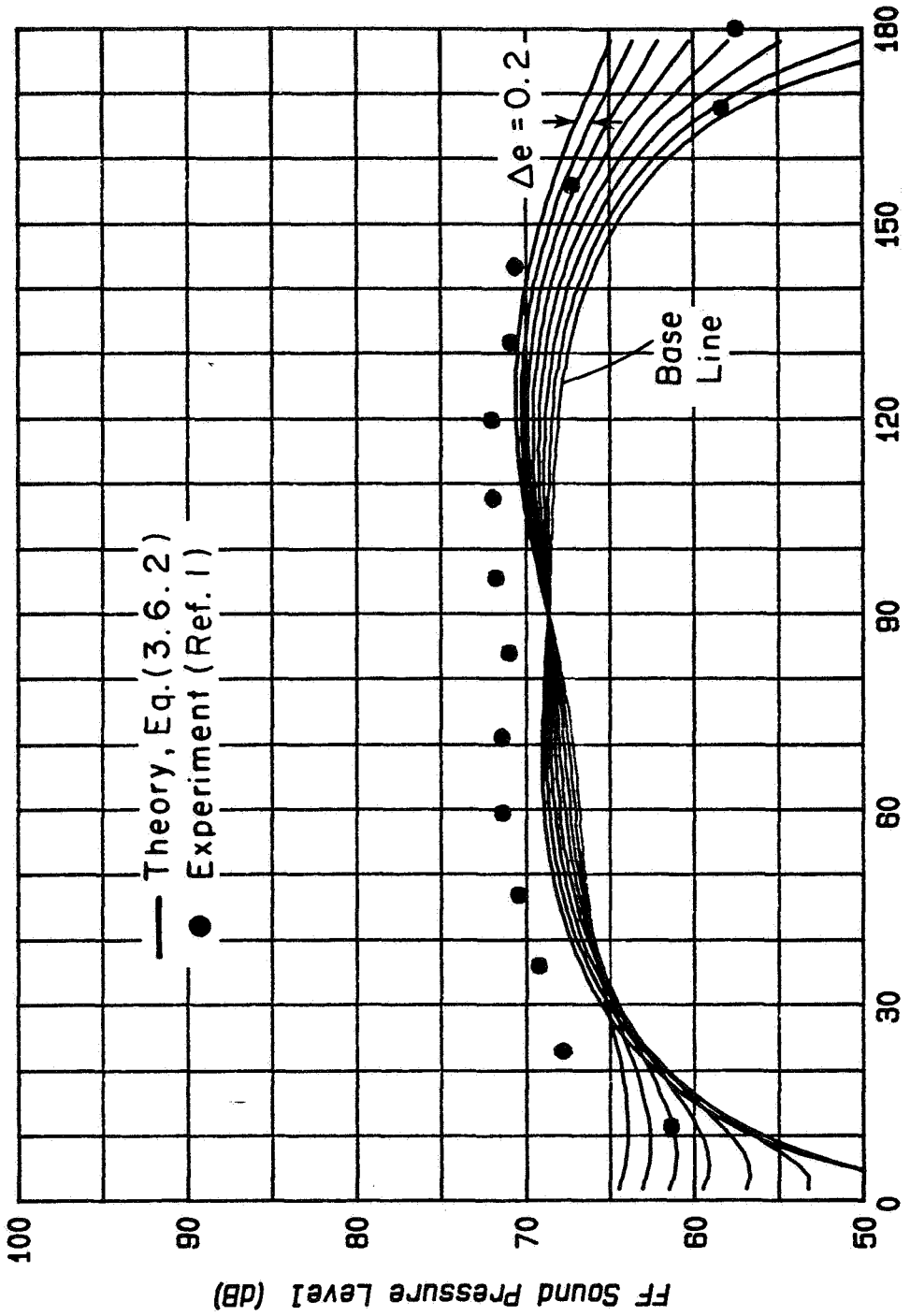

Figure D.1c Comparison of Inviscid Theory (with in-plane Vibration Comtamination) with Experiment; k=1.255, α_o=82.1 μrad.

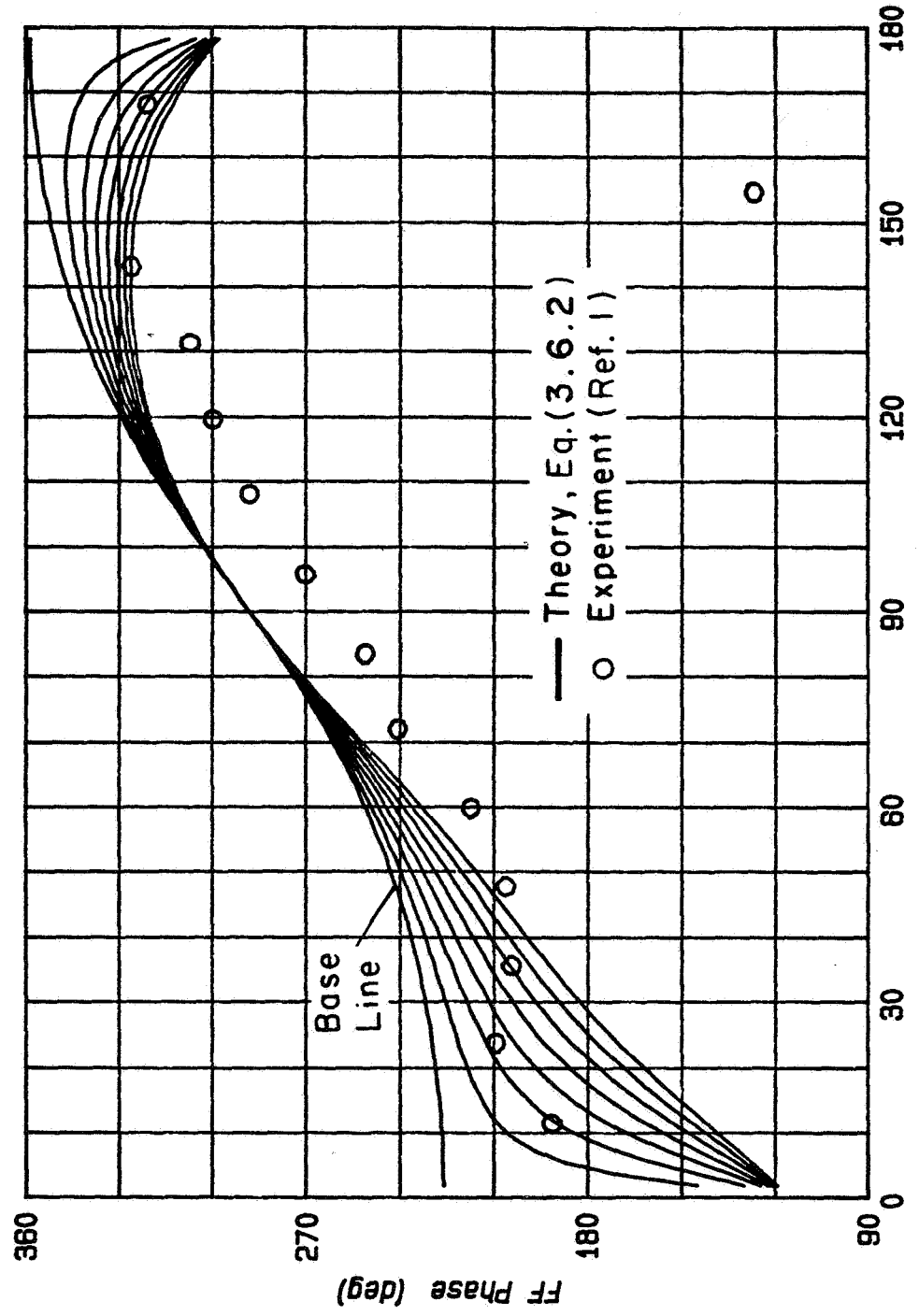

Figure D.1d Comparison of Inviscid Theory (with in-plane Vibration Contamination) with Experiment; k=1.255, α_o=82.1 μrad.

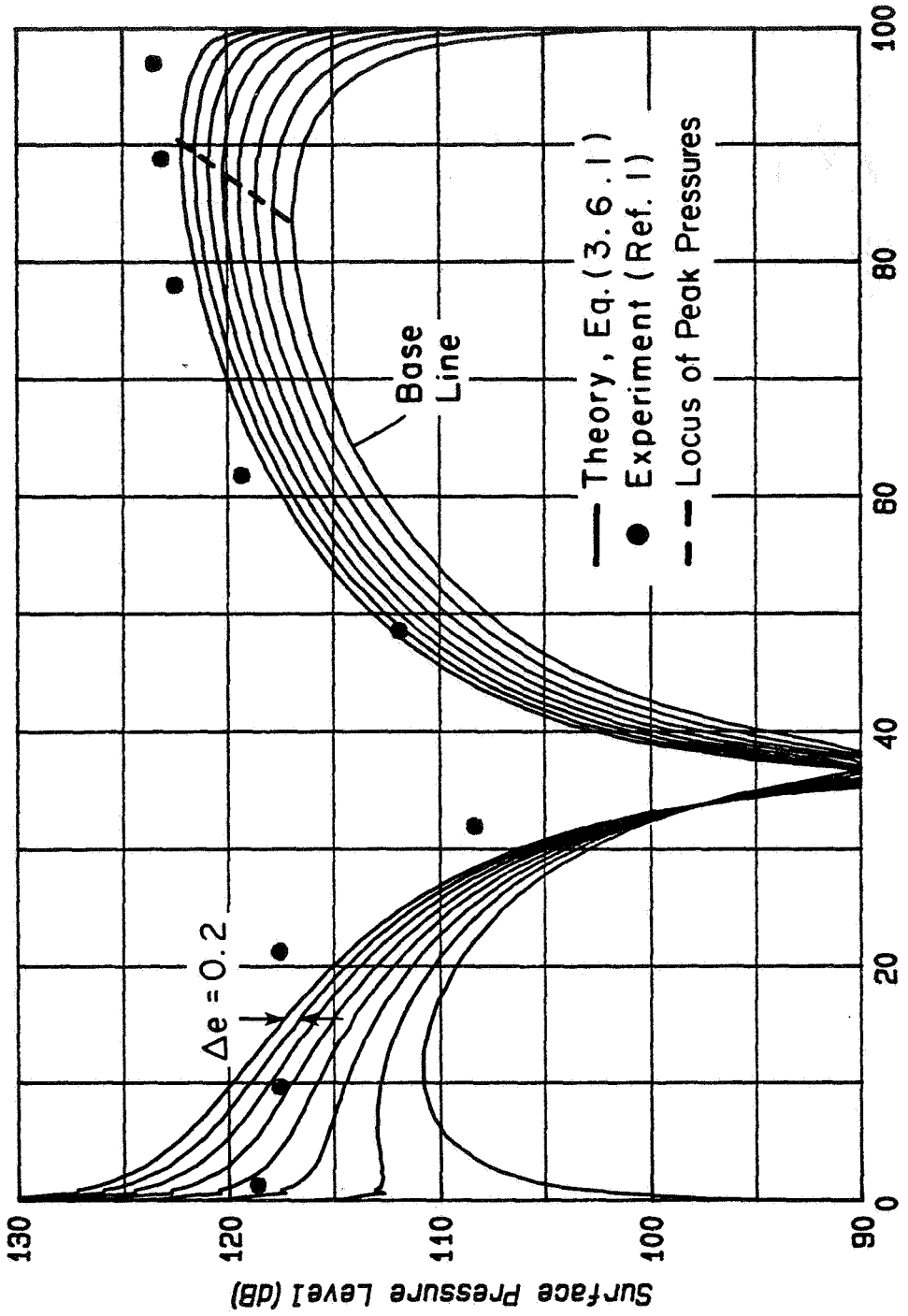

Figure D.2a Comparison of Inviscid Theory (with in-plane Vibration Contamination) with Experiment; k=1.255, α_o=259.3 μrad.

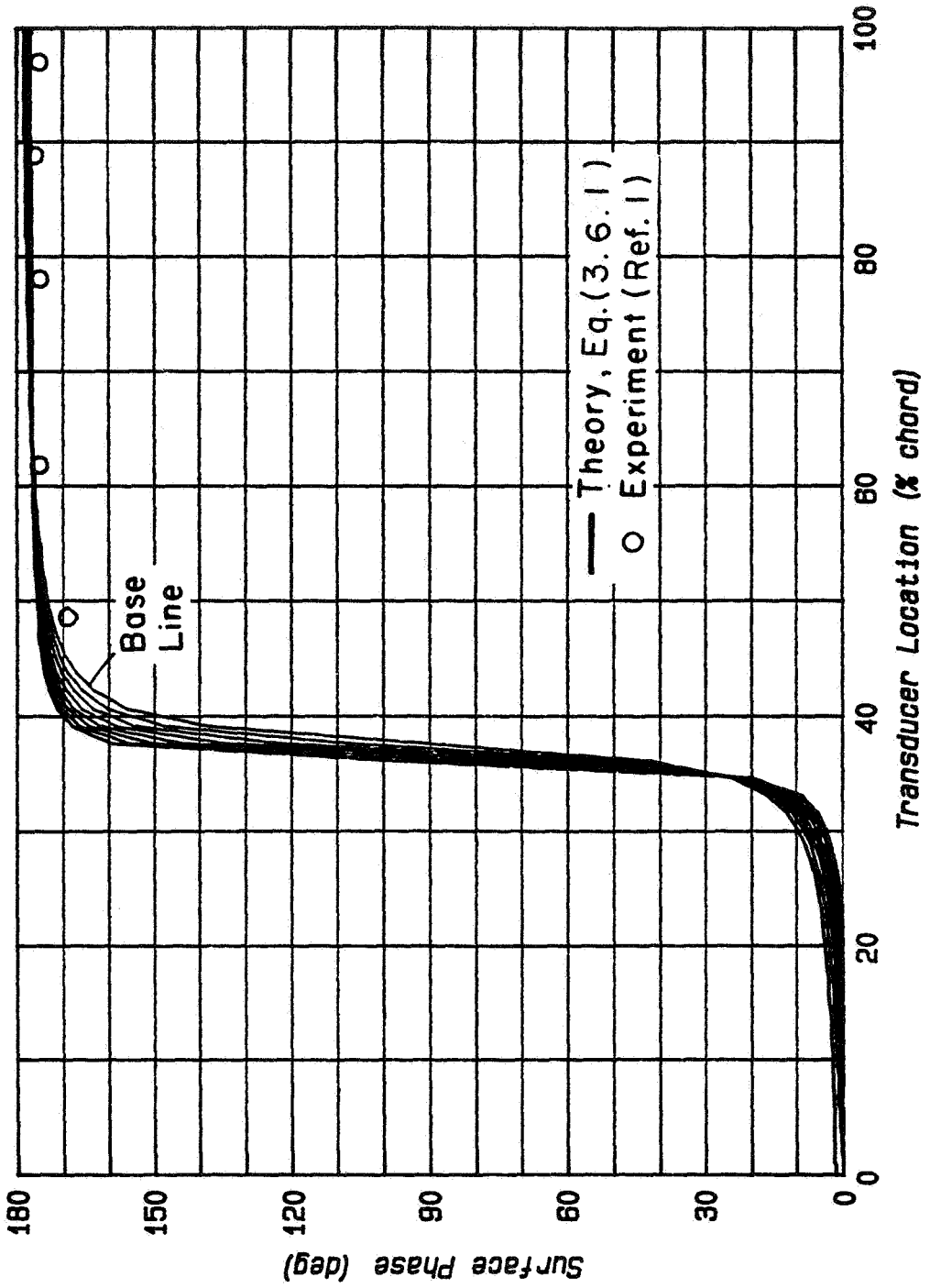

Figure D.2b Comparison of Inviscid Theory (with in-plane Vibration Contamination) with Experiment; k=1.255, α_o=259.3 μrad.

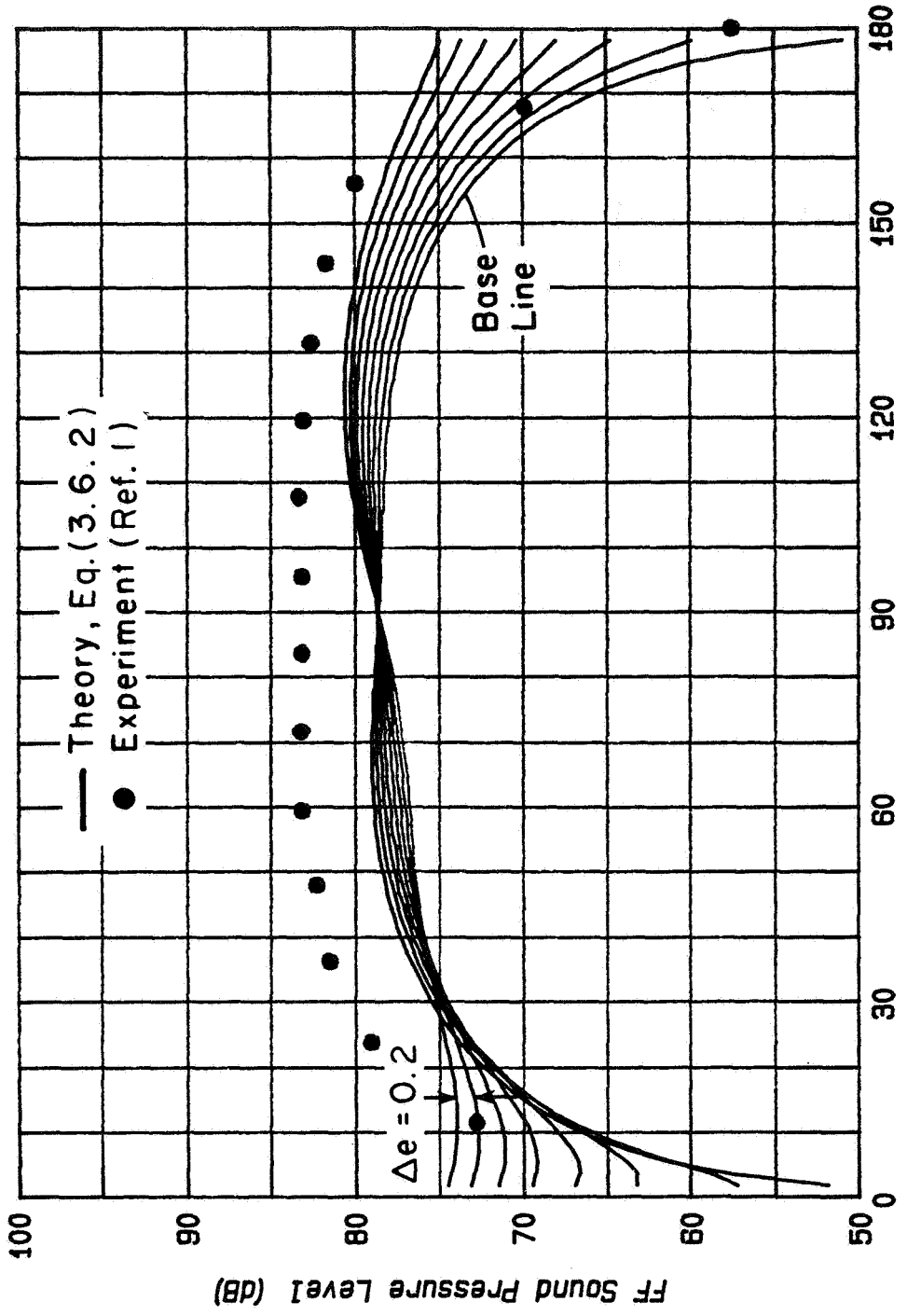

Figure D.2c Comparison of Inviscid Theory (with in-plane Vibration Contamination) with Experiment; k=1.255, α_o=259.3 μrad.

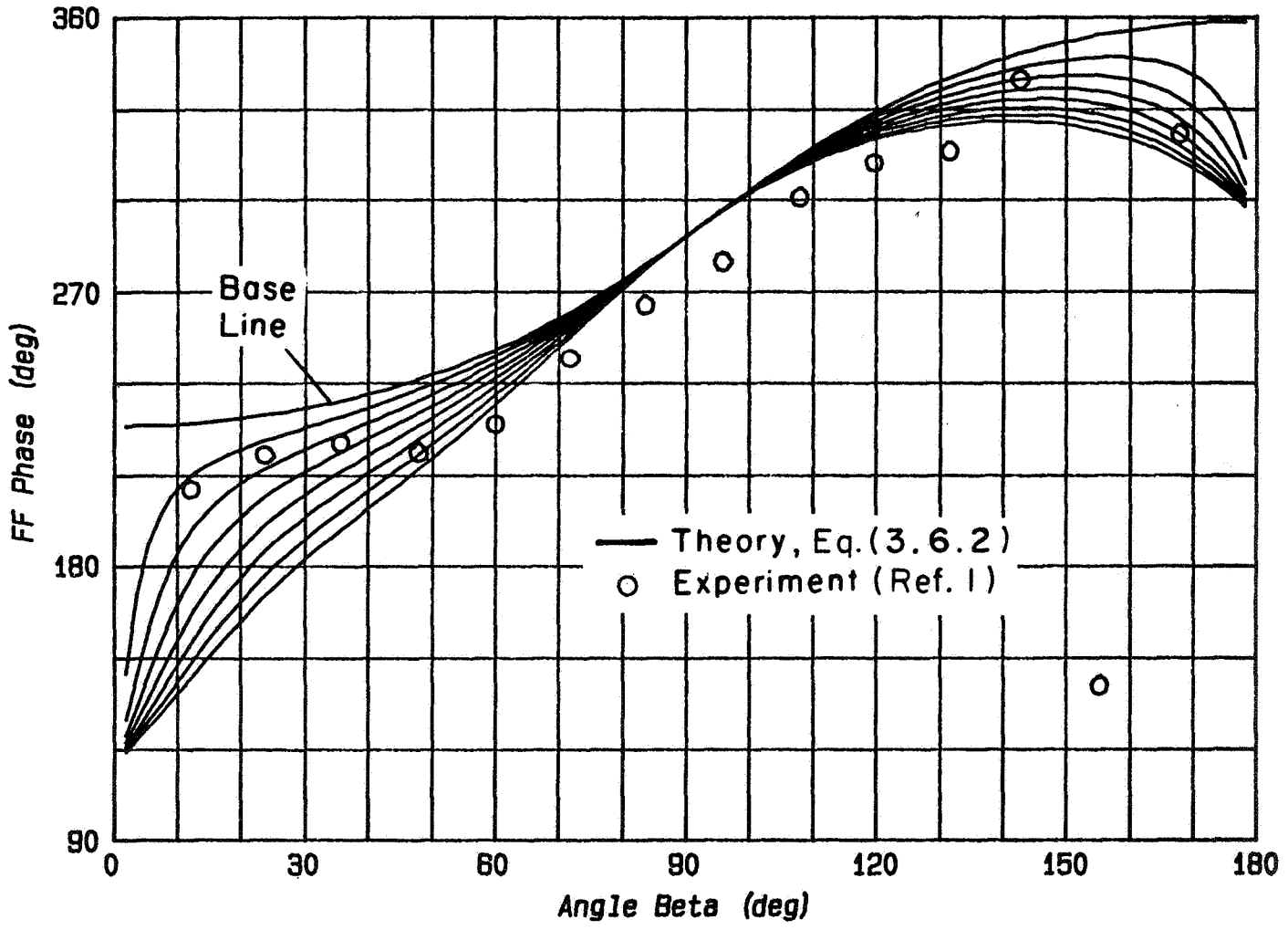

Figure D.2d Comparison of Inviscid Theory (with in-plane Vibration Contamination) with Experiment; k=1.255, α_o=259.3 μrad.

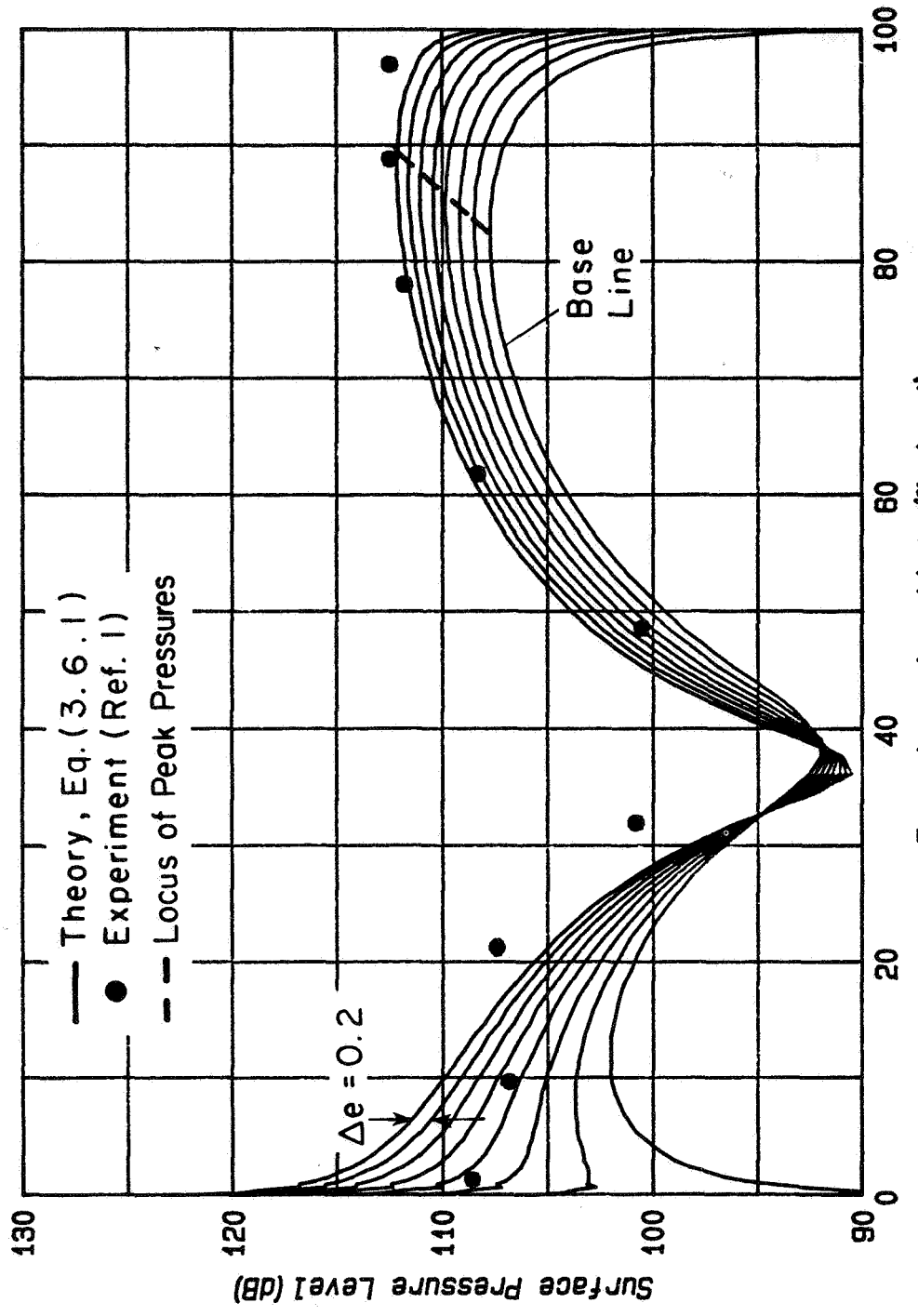

Figure D.3a Comparison of Inviscid Theory (with in-plane Vibration Contamination) with Experiment; k=1.989, α_o=30.8 μrad.

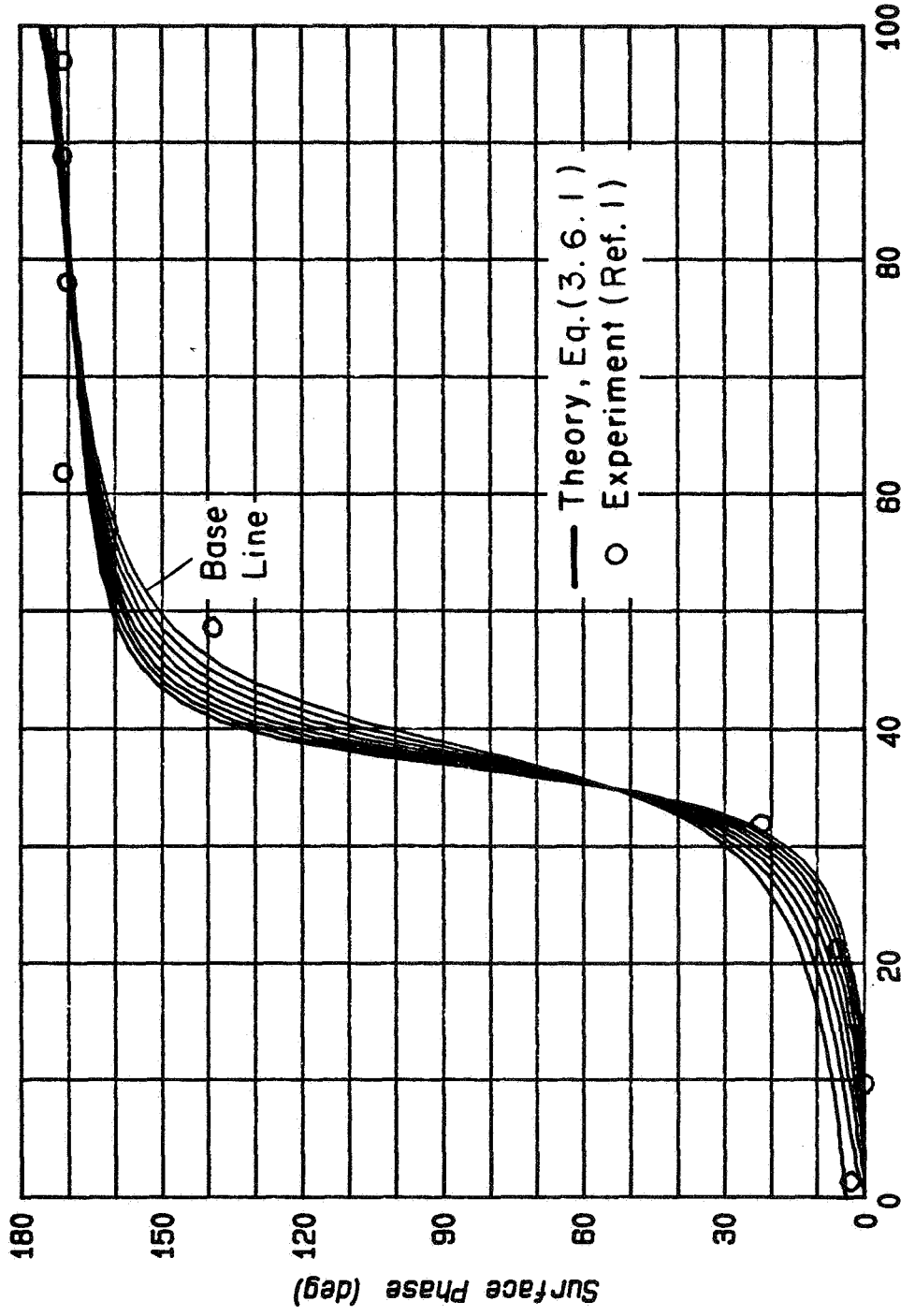

Figure D.3b Comparison of Inviscid Theory (with in-plane Vibration Contamination) with Experiment; k=1.989, α_o=30.8 μrad.

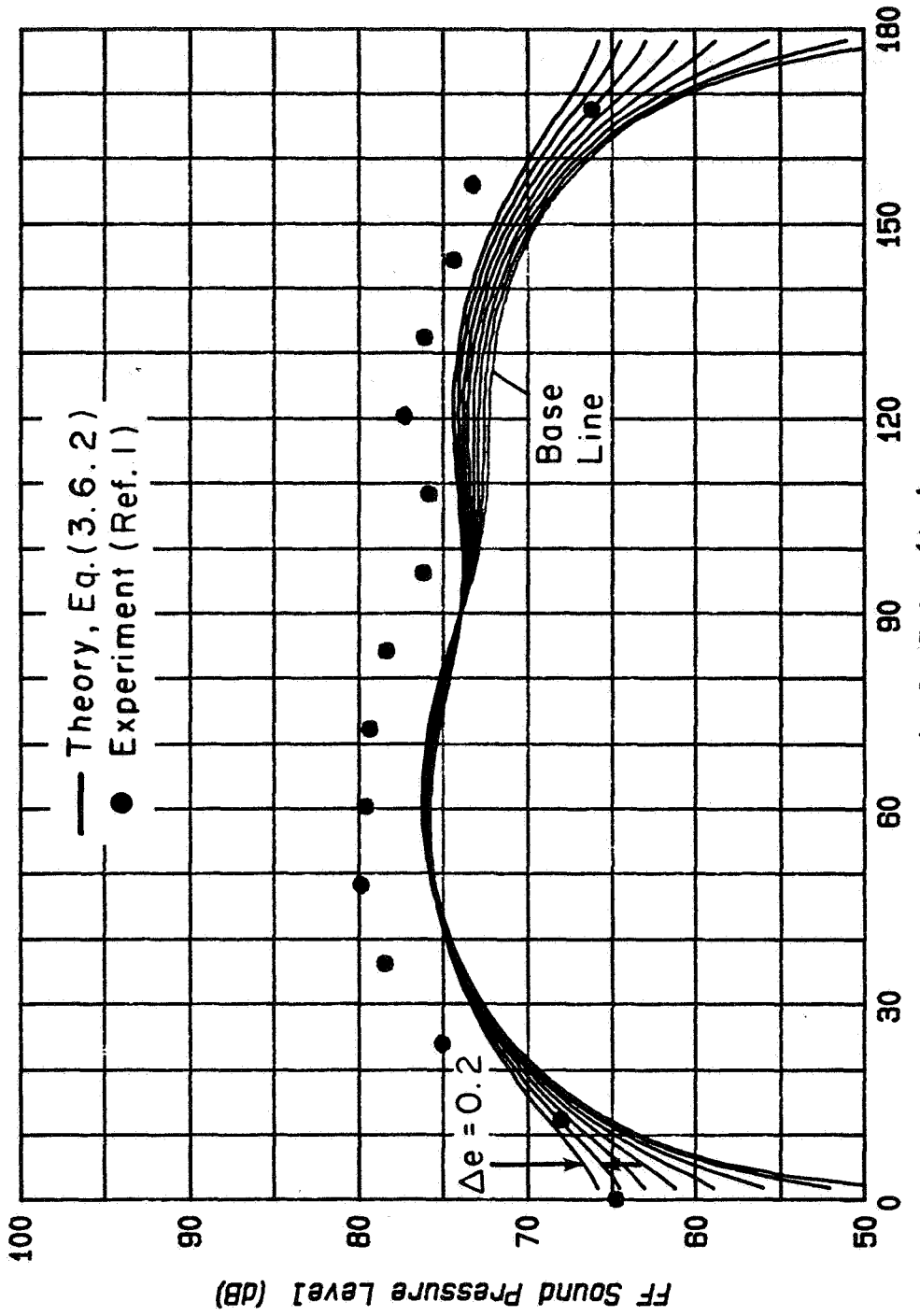

Figure D.3c Comparison of Inviscid Theory (with in-plane Vibration Contamination) with Experiment; k=1.989, α_o=30.8 μrad.

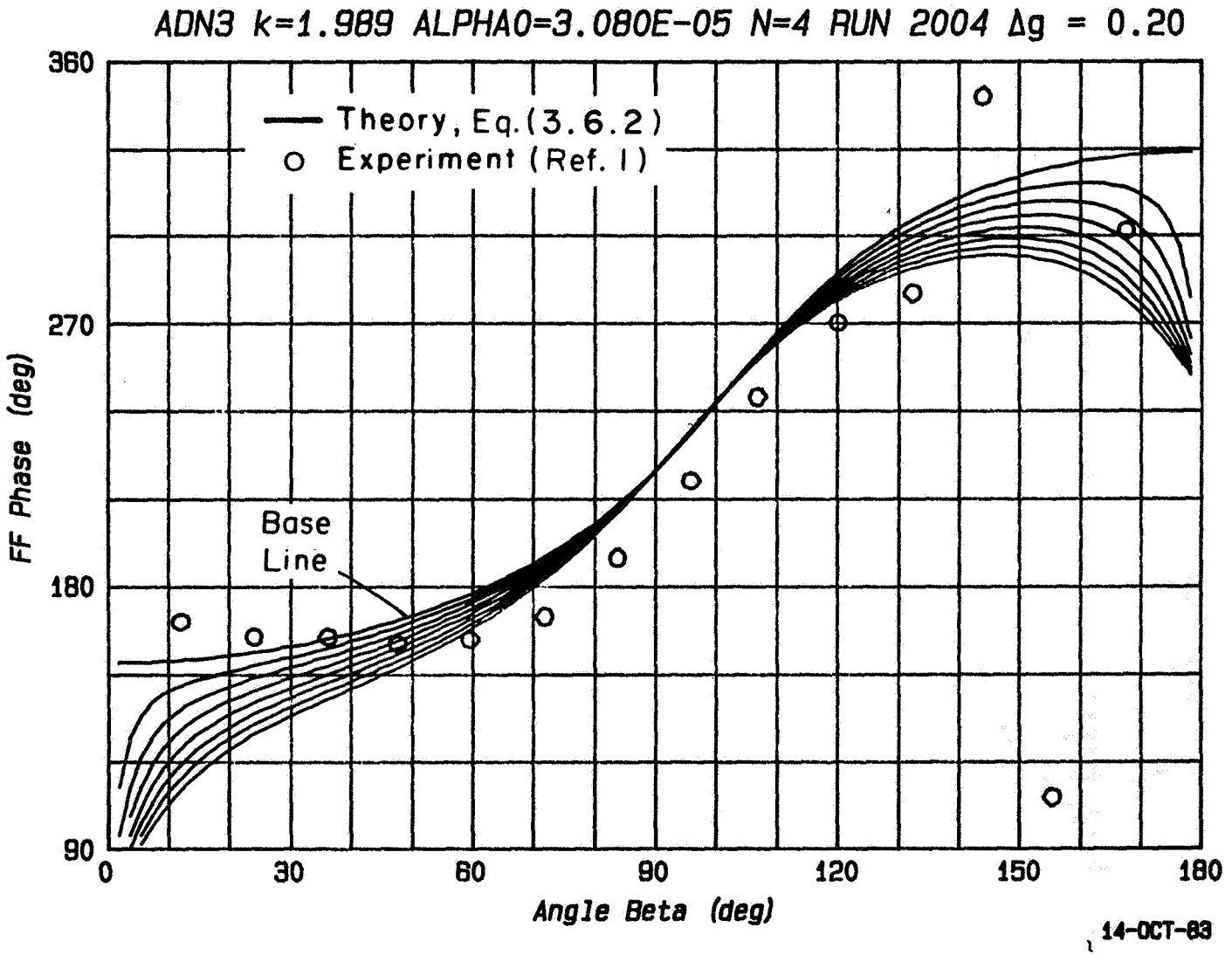

Figure D.3d Comparison of Inviscid Theory (with in-plane Vibration Contamination) with Experiment; k=1.989, α_o=30.8 μrad.

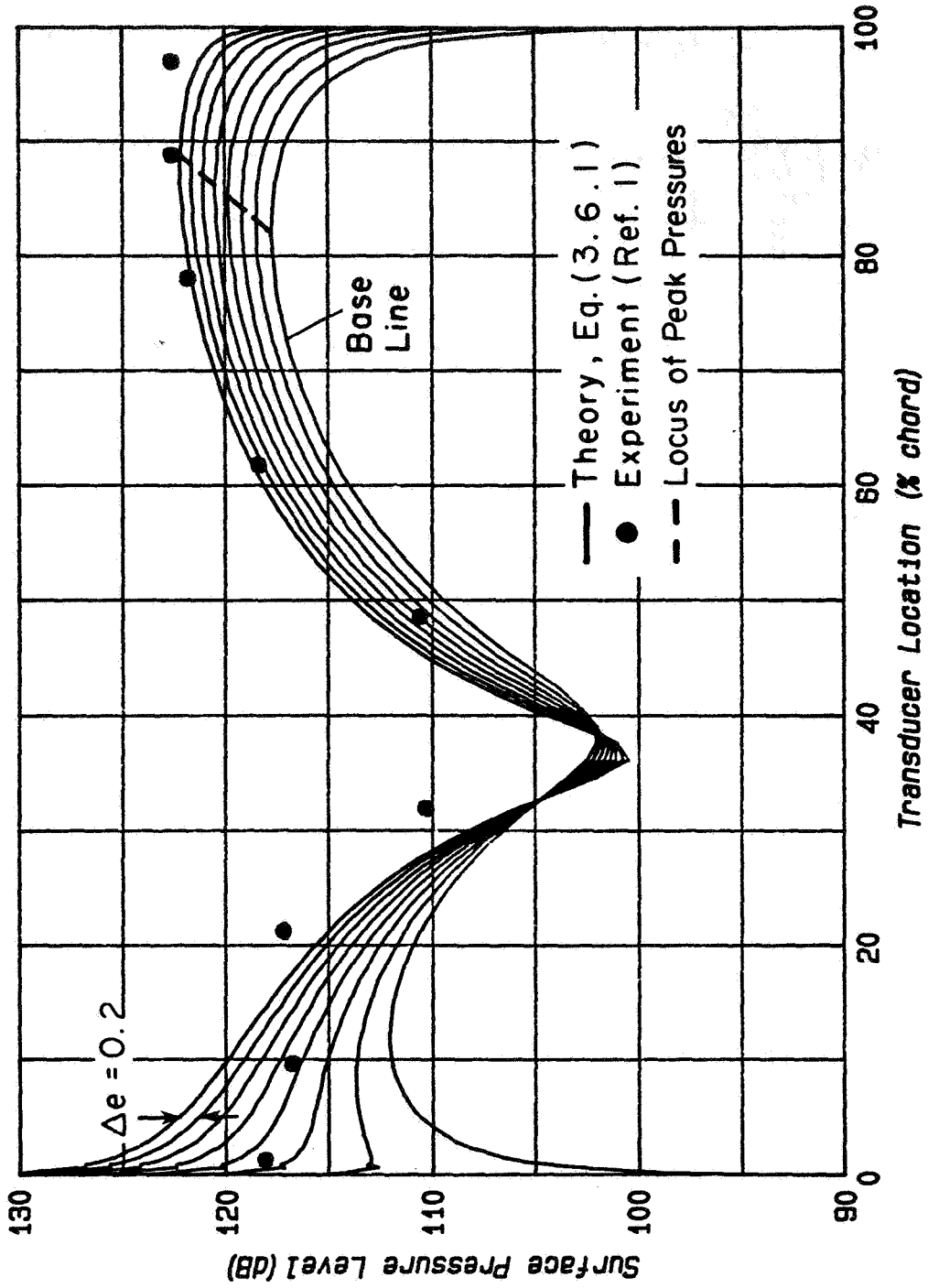

Figure B.4a Comparison of Inviscid Theory (with in-plane Vibration Contamination) with Experiment; k=1.989, α_o=97.6 μrad.

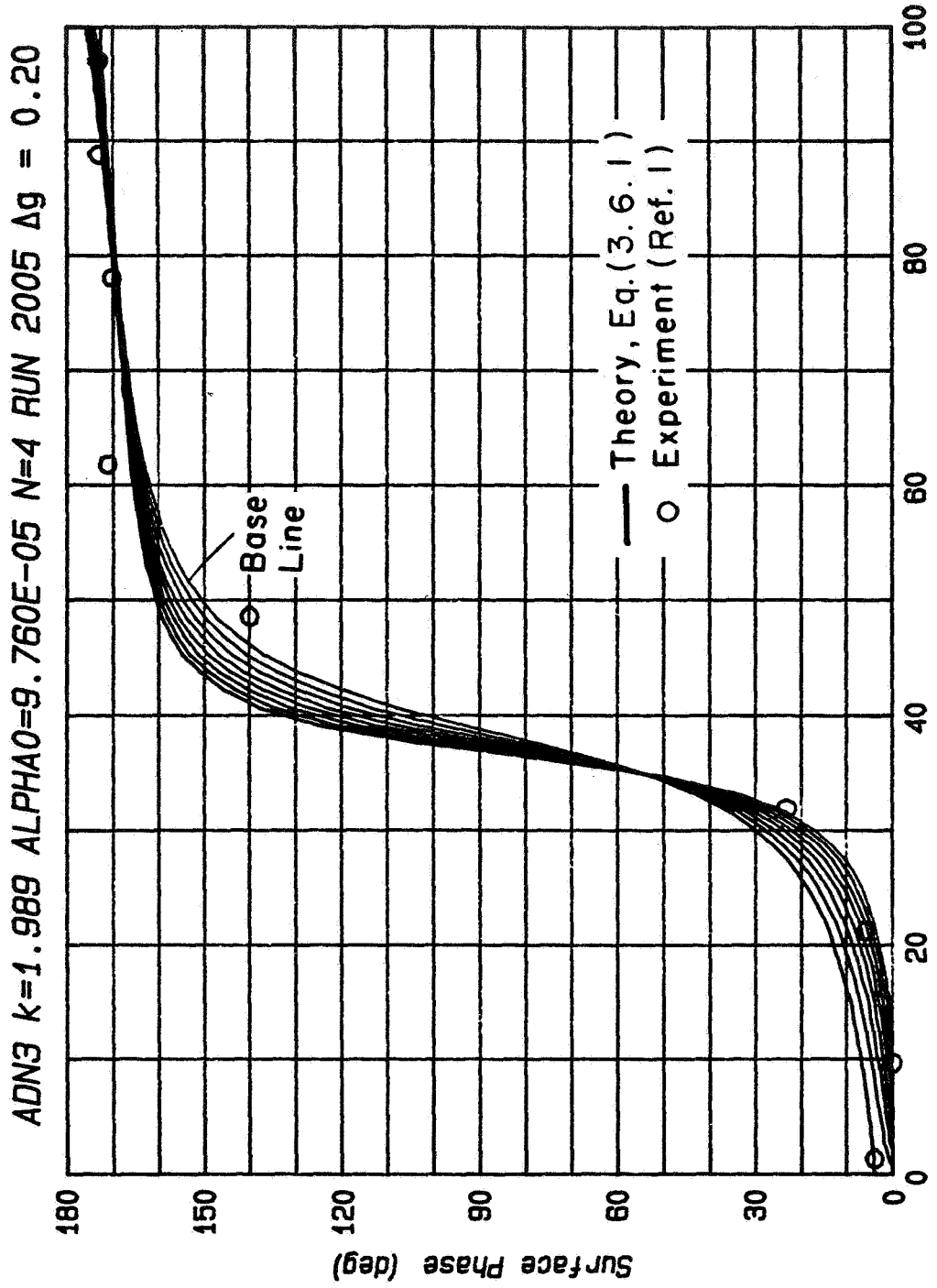

Figure D.4b Comparison of Inviscid Theory (with in-plane Vibration Contamination) with Experiment: k=1.989, α_o=97.6 μrad.

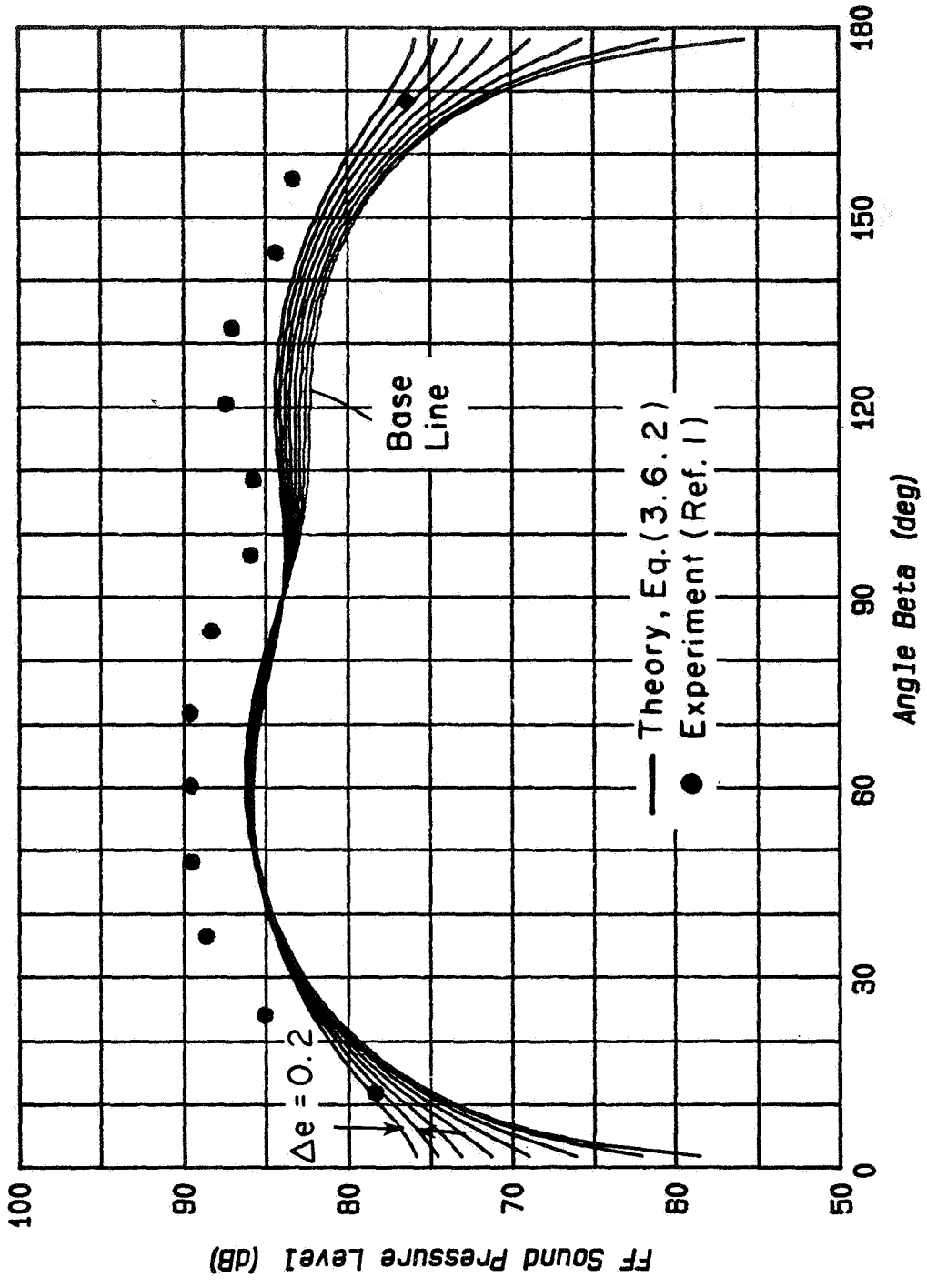

Figure D.4c Comparison of Inviscid Theory (with in-plane Vibration Contamination) with Experiment; $k=1.989$, $\alpha_o=97.6$ μrad.

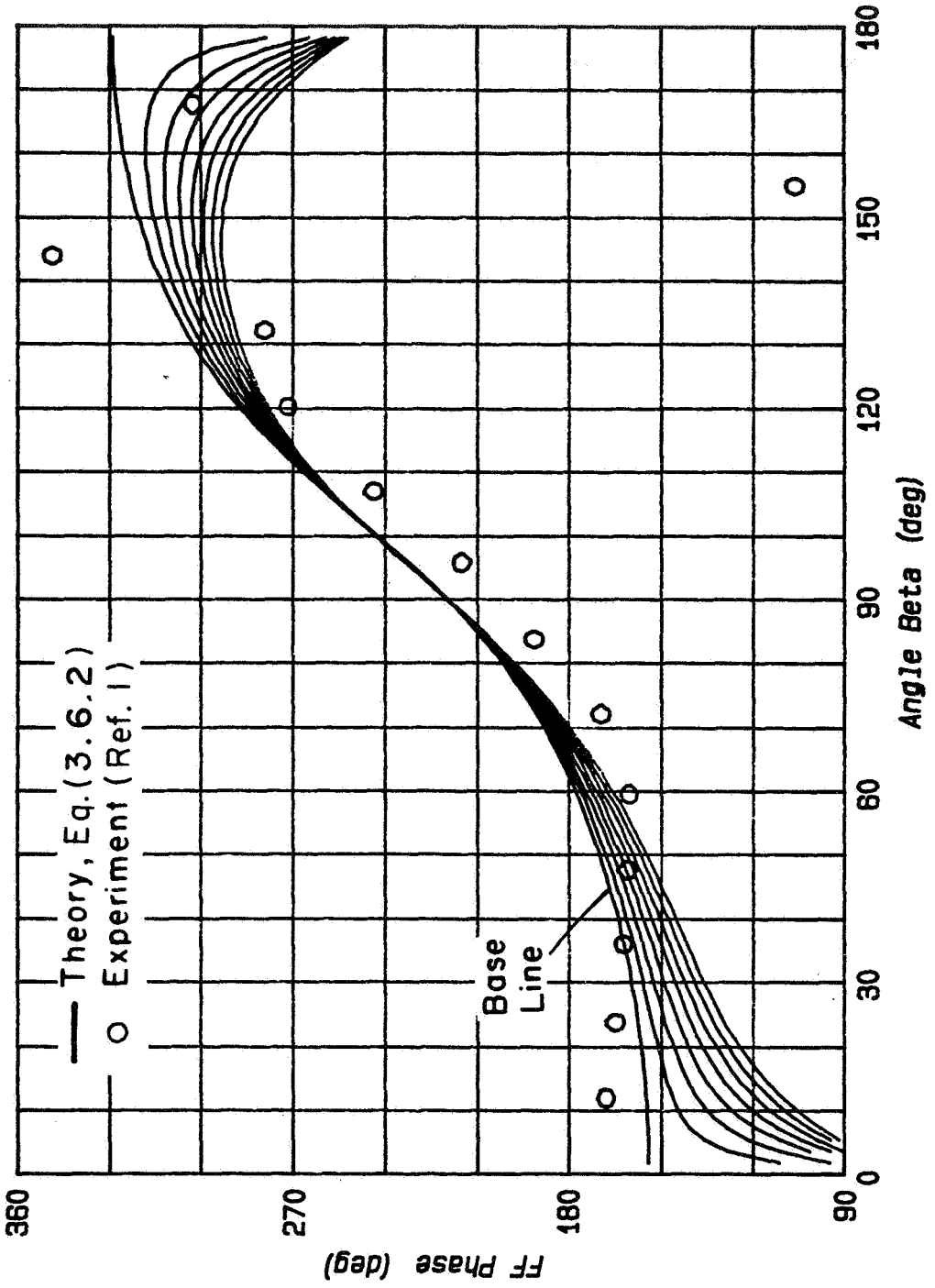

Figure D.4d Comparison of Inviscid Theory (with in-plane Vibration Contamination) with Experiment; k=1.989, σ_o=97.6 μrad.

APPENDIX E
THE DISSIPATION INTEGRAL

Consider the dissipation integral (4.4.22) of the main text; i.e.,

$$v = \frac{\sigma^2}{4(2\pi)^2} \oint\!\!\oint d\alpha d\beta \, \frac{(\alpha^2+\beta^2)|L^+|^2}{|\lambda_o|^2 \, \mathrm{Re}\, \lambda_o} \tag{E.1}$$

where

$$\lambda_o = \left[\alpha^2 + \beta^2 + i\sigma^2(1+\alpha s)\right]^{1/2} \tag{E.2}$$

and

$$L^+(\alpha,\beta) = \iint dxdy \, e^{-i(\alpha x+\beta y)} \, L(x,y) \tag{E.3}$$

with

$$L(x,y) = \frac{2\alpha_o}{\pi A^2} \sqrt{A^2-y^2} \, (1+x)^{\nu}(1-x)^{\epsilon} P(x) \tag{E.4}$$

We evaluate $\mathscr{P}_v$ for $\sigma >> 1$ with $\sigma s = O(1)$. Let

$$(\alpha,\beta) = \sigma(u,v) \tag{E.5}$$

Then

$$\mathscr{P}_v = \frac{\sigma^3}{4(2\pi)^2} \cdot \Phi \tag{E.6}$$

where

$$\Phi = \oint\!\!\oint dudv \, \frac{(u^2+v^2)|L^+(\sigma u,\sigma v)|^2}{|\Lambda|^2 \, \mathrm{Re}\, \Lambda} \tag{E.7}$$

and

$$\Lambda = \left[u^2 + u^2 + i(1+\delta u)\right]^{1/2} \tag{E.8}$$

$$\delta = \sigma s = O(1) \tag{E.9}$$

First we evaluate the transformed load,

$$L^+(\sigma u,\sigma v) = \frac{2\alpha_o}{\pi A^2}\int_{-A}^{A} e^{-i\sigma v y}\sqrt{A^2-y^2}\,dy \int_{-1}^{1} e^{-i\sigma u x}(1+x)^{\nu}(1-x)^{\varepsilon}P(x)dx$$

$$= 2\alpha_o \cdot \frac{J_1(\sigma vA)}{\sigma vA} \cdot L^+(\sigma u) \tag{E.10}$$

where

$$L^+(\sigma u) = \int_{-1}^{1} e^{-i\sigma u x}\,(1+x)^{\nu}(1-x)^{\varepsilon}P(x)dx \tag{E.11}$$

Thus

$$|L^+(\sigma u,\sigma v)|^2 = 4\alpha_o^2\left(\frac{J_1(\sigma vA)}{\sigma vA}\right)^2 |L^+(\sigma u)|^2 \tag{E.12}$$

Now consider the integral

$$I = \int_{-\infty}^{\infty} dv\left(\frac{J_1(\sigma vA)}{\sigma vA}\right)^2 F(v) \tag{E.13}$$

where F(v) is a bounded even function of v for $\sigma \to \infty$. Then for $\sigma >> 1$, we have

$$I \approx \frac{2F(0)}{\sigma A}\int_{o}^{\infty}\left(\frac{J_1(t)}{t}\right)^2 dt$$

$$= \frac{8}{3\pi}\,\frac{F(0)}{\sigma A} \tag{E.14}$$

so that (E.7) can be reduced to the following single integral:

$$\Phi = \frac{32\alpha_o^2}{3\pi\sigma A}\int_{-\infty}^{\infty} du\;\frac{u^2|L^+(\sigma u)|^2}{|\Lambda_o|^2\ \mathrm{Re}\ \Lambda_o} \tag{E.15}$$

with

$$\Lambda_o = \left[u^2 + i(1+\delta u)\right]^{1/2} \tag{E.16}$$

Now we return to (E.11) and evaluate $L^+(\sigma u)$. For $\sigma >> 1$ and $u = O(1)$, the principal contribution to the integral is from the end points. Thus

$$L^+(\sigma u) = P(-1)\cdot 2^{\varepsilon}\cdot e^{-i\sigma u}\cdot \int_o^{\infty} e^{-i\sigma u t}\cdot t^{\nu} dt$$

$$+ P(1)\cdot 2^{\nu}\cdot e^{-i\sigma u}\cdot \int_o^{\infty} e^{i\sigma v}\, t^{\varepsilon} dt$$

$$= P(-1)\cdot 2^{\varepsilon}\cdot \frac{\Gamma(1+\nu)}{(\sigma u)^{1+\nu}} e^{i(\sigma u - \pi/2(1+\nu))}$$

$$+ P(1)2^{\nu}\cdot \frac{\Gamma(1+\varepsilon)}{(\sigma u)^{1+\varepsilon}}\cdot e^{-i(\sigma u - \pi/2(1+\varepsilon))} \tag{E.17}$$

For the purpose of evaluating the integral in (E.15), we have

$$|L^+(\sigma u)|^2 = |P(-1)|^2\cdot \frac{4^{\varepsilon}(\Gamma(1+\nu))^2}{(\sigma|u|)^{2(1+\nu)}} + |P(1)|^2\cdot \frac{4^{\nu}(\Gamma(1+\varepsilon))^2}{(\sigma|u|)^{2(1+\varepsilon)}} \tag{E.18}$$

We further simplify the calculation by setting $\nu = \varepsilon$ so that

$$|L^+(\sigma u)|^2 = \left(|P(-1)|^2 + |P(1)|^2\right)\cdot \frac{4^{\varepsilon}(\Gamma(1+\varepsilon))^2}{(\sigma|u|)^{2(1+\varepsilon)}} \tag{E.19}$$

Finally, we note the following results:

$$|A|^2 \operatorname{Re} A = \frac{1}{\sqrt{2}} \left[u^4 + (1+\delta u)^2\right]^{1/2} \left\{u^2 + \left[u^4 + (1+\delta u)^2\right]^{1/2}\right\}^{1/2} \tag{E.20}$$

Substitute (E.15), (E.19), and (E.20) into (E.6) to get

$$\mathscr{P}_v = \frac{4^{\varepsilon}(\Gamma(1+\varepsilon))^2}{o^{2\varepsilon}} \left(\frac{2\sqrt{2}\ \alpha_o^2}{3\pi^3 A}\right) \cdot \mathscr{I}_{\varepsilon}(\delta s)\ |P(-1)|^2 + |P(1)|^2 \tag{E.21}$$

where for $0 < \varepsilon < 1/2$,

$$\mathscr{I}_{\varepsilon}(\delta) = \int_{-\infty}^{\infty} \frac{du}{|u|^{2\varepsilon}\left[u^4 + (1+\delta u)^2\right]^{1/2} \left\{u^2 + \left[u^4 + (1+\delta u)^2\right]^{1/2}\right\}^{1/2}} \tag{E.22}$$

REFERENCES

1. Brooks, Thomas F.: An Experimental Evaluation of the Application of the Kirchhoff Formulation for Sound Radiation from an Oscillating Airfoil. NASA TP-1048, 1977.

2. Yates, John E.: Viscous Theory of Surface Noise Interaction Phenomena. NASA CR-3331, 1980.

3. Yates, John E.: The Importance of Viscosity in Experimental Applications of Kirchoff-Type Integral Relations. Presented at the AIAA 6th Aeroacoustics Conference, Hartford, Conn., AIAA Paper No. 80-0971, 1980.

4. Ffowcs Williams, J. E.; and Hawkings, D. L.: Sound Generation by Turbulence and Surfaces in Arbitrary Motion. Philos. Trans. R. Soc. London, ser. A, vol. 264, no. 1151, 1969, pp. 321-342.

5. Yates, John E.: A Study of the Viscous Dissipation and Surface Loading on a Vibrating Surface. NASA CR-3499, 1981.

6. Yates, John E.: Viscous Thin Airfoil Theory. NASA CR-163069, 1980.

7. Abramowitz, M.; and Stegun, I. A., eds.: Handbook of Mathematical Functions (2nd Printing), National Bureau of Standards (Washington, D.C.), 1964.

8. Abbott, Ira H.; and von Doenhoff, Albert E.: Theory of Wing Sections, Dover Publications (New York), 1959.

National Aeronautics and
Space Administration

Washington, D.C.
20546

Official Business
Penalty for Private Use, $300

THIRD-CLASS BULK RATE

Postage and Fees Paid
National Aeronautics and
Space Administration
NASA-451

NASA

POSTMASTER: If Undeliverable (Section 158 Postal Manual) Do Not Return